

ENHANCED RESOLUTION IMAGING FROM REMOTELY SENSED
MICROWAVE DATA

Warren B. Davis

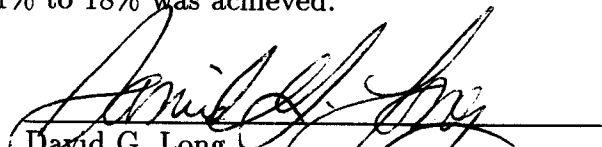
Department of Electrical and Computer Engineering

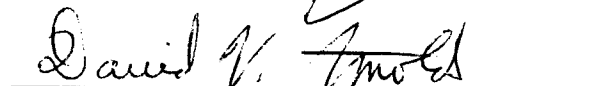
M. S. Degree, Nov. 1993

ABSTRACT

Analysis in the wavenumber domain was performed on three imaging methods to determine the effective resolution of the methods as applied to remotely sensed microwave data. Resolution was determined as the bandwidth for which the error in the image spectrum was below a threshold. This analysis showed that image resolution is limited by an effective measurement response, which is determined by the size, shape, and orientation of the measurement cells and cell responses associated with the data set. Data sets from three low-resolution remote sensing instruments were used to generate test images and actual images and their resolutions were compared. The comparison showed that if the measurement cells used to collect data were long and narrow, and the cells were oriented in many different directions, then the resolution of the image was dominated by the short dimension of the measurement cells. If the measurement cells were circular, then the resolution was determined by the diameter of the measurement cells. A method to further enhance the resolution of an image using a compensation filter was also developed. The measurement response of the underlying data was determined and used to design a filter with the inverse response. A low pass filter was then used to avoid excessive amplification of high-frequency noise in the image. With this method, resolution enhancement of 11% to 18% was achieved.

COMMITTEE APPROVAL:


David G. Long
Committee Chairman


David V. Arnold
Committee Member


Richard H. Selfridge
Graduate Coordinator

ENHANCED RESOLUTION IMAGING FROM REMOTELY SENSED MICROWAVE DATA

A Thesis

Submitted to the

Department of Electrical and Computer Engineering

Brigham Young University

In Partial Fulfillment

of the Requirements for the Degree

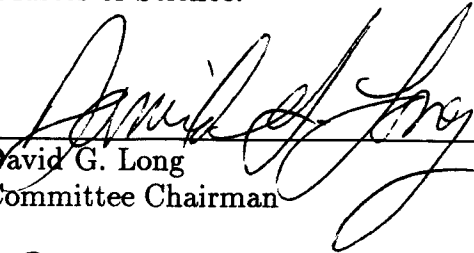
Master of Science

by

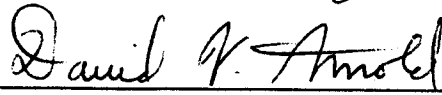
Warren B. Davis

Nov. 1993

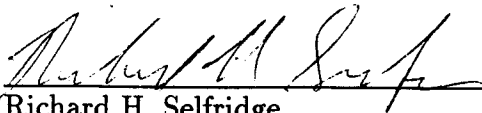
This thesis by Warren B. Davis is accepted in its present form by the Department of Electrical and Computer Engineering of Brigham Young University as satisfying the thesis requirement for the degree of Master of Science.



David G. Long
Committee Chairman



David V. Arnold
Committee Member



Richard H. Selfridge
Graduate Coordinator

Nov 23, 1993
Date

ACKNOWLEDGMENTS

I am grateful to my research advisor, Dr. David Long, for the invaluable advice he gave me in the development of the ideas for this thesis. I admire his creativity in solving problems and developing new ideas. I also thank him and Dr. David Arnold for their helpful evaluations of my writing.

I acknowledge the Physical Oceanography DAAC at Jet Propulsion Laboratory/California Institute of Technology for distributing the data used in this research.

Lastly, I thank my wife, Tina, and my daughter, Marissa, for their love and support. They mean the world to me.

CONTENTS

Acknowledgments	iii
1 Introduction	1
2 Resolution	4
2.1 Introduction	4
2.2 Resolution of Remotely Sensed Data	7
2.3 The Effects of Noise	11
2.4 Variable Cell Response	11
2.5 Resolution Enhancement	12
3 Imaging	16
3.1 Imaging Methods	16
3.2 Example 1: Surface Response with Linearly Increasing Wavenumber	19
3.3 Example 2: Resolving Closely Spaced Surface Features	24
3.4 Resolution Enhancement through Filter Compensation	24
3.5 Summary	32
4 Image Reconstruction from Microwave Data	33
4.1 Basics of Microwave Measurements	33
4.1.1 Radiometry	33
4.1.2 Scatterometry	35
4.2 Instrument Descriptions	36
4.2.1 SMMR	36
4.2.2 SASS and ERS-1 Scatterometers	37
4.3 Application of SIRF to SMMR	40
4.3.1 Considerations for Imaging	40
4.3.2 The Modified SIRF Algorithm	43
4.3.3 Improved SMMR Cell Response Estimate	45
4.3.4 Computational Considerations	47
5 Results	49
5.1 Simulation Results	49
5.1.1 SMMR	50
5.1.2 SASS	60
5.1.3 ERS-1 Scatterometer	68
5.1.4 Simulation Summary	73
5.2 Real Data	78
5.2.1 SMMR	78

5.2.2	SASS	78
5.2.3	ERS-1 Scatterometer	83
6	Conclusions	86
6.1	Discussion	86
6.2	Contributions	87
6.3	Future Research	88

LIST OF FIGURES

2.1	Instantaneous footprint and corresponding response pattern.	5
2.2	Integrated footprint	6
2.3	Instantaneous and integrated weighting functions.	6
2.4	Cell response and associated measurement cell.	7
2.5	Cell response, surface response, measurements, and corresponding Fourier transforms.	10
2.6	$Z(k)$ and the associated error, $\epsilon(k)$, with resolution determined by $E = 1/2$	11
2.7	Noisy measurement spectrum, $V(k)$, and the associated error, $\epsilon(k)$, with resolution determined by $E = 1/2$	12
2.8	FTs of combined cells responses and associated error.	13
2.9	Image, $p(n)$, generated by sampling a measurement set, $z(x)$, that is infinitely dense in x	14
2.10	Noise level, $N(k)$, of measurements after compensation filtering and the associated error, $\epsilon(k)$, with resolution determined by $E = 1/2$	15
3.1	Determination of resolution elements that contribute to a measure- ment.	16
3.2	Determining pixel estimates from the measurement locations.	17
3.3	Determining pixel estimates from all measurements touching the pixel.	18
3.4	Surface response and cell response used for simulations.	20
3.5	Surface response estimates and associated error for noise-free mea- surements.	22
3.6	Surface response estimates and associated error for noisy measure- ments.	23
3.7	Surface response estimates and associated error for mixed measure- ment cells.	25
3.8	Error curves for noise-free, noisy, and mixed cell images.	26
3.9	Noise-free simulation of resolving closely spaced features.	27
3.10	Determining the effective low pass filter and inverse filter.	29
3.11	Enhancing image resolution through compensation filtering.	30
3.12	Increasing feature resolvability through compensation filtering.	31
4.1	SMMR swath relative to the direction of travel of the spacecraft.	37
4.2	SMMR footprints	38
4.3	SASS and ERS-1 antenna illumination patterns	39
4.4	SASS integrated measurement cell.	39
4.5	ERS-1 cell response.	40
4.6	Effect of clouds on transmission from the earth surface into space.	42
4.7	Integrated cell response using the 3 dB cutoff and 15 dB roll-off.	46
5.1	Typical cell layout (3 dB contour) for SMMR 6.6 GHz measurements for a single scan and for several scans.	51

5.2	Test image and SIRF image for simulated 6.6 GHz noise-free SMMR data	52
5.3	Cross section and estimated error of SIRF image from 6.6 GHz SMMR data	53
5.4	Filter response of compensating filters.	54
5.5	SIRF images after compensation filtering by Filter 1 and Filter 2.	55
5.6	Cross section and estimated error of compensation filtered images.	56
5.7	SIRF image from simulated noisy 6.6 GHz SMMR measurements.	57
5.8	Cross section of SIRF image from simulated noisy 6.6 GHz SMMR data	58
5.9	Compensation filtered SIRF image from simulated noisy 6.6 GHz SMMR measurements.	58
5.10	Cross section and estimated error of SIRF image from simulated noisy 6.6 GHz SMMR data after compensation filtering.	59
5.11	Typical cell layout (3 dB contour) for SMMR 10.69 GHz measurements for a single scan and for several scans.	60
5.12	Test image and SIRF image for 10.69 GHz SMMR data	61
5.13	Cross section and estimated error of SIRF image from 10.69 GHz SMMR data	62
5.14	Typical cell layout (3 dB contour) for SASS measurements for a single beam and for several beams.	63
5.15	Orientation of SASS cells used in simulation.	63
5.16	Effective cell response and FT for cells aligned in one direction.	64
5.17	Effective resolution of the SASS image	65
5.18	Test image and SIRF image for SASS data	65
5.19	Resolution of the SIRF image from simulated SASS data	66
5.20	Cross section and estimated error of SIRF image from SASS data	67
5.21	Typical cell layout (3 dB contour) for ERS-1 measurements for a single cell and the cells from a single measurement cycle and for several measurement cycles.	68
5.22	Test image and SIRF image for ERS-1 data	69
5.23	Cross section and estimated error of SIRF image from ERS-1 data	70
5.24	ERS-1 SIRF image after compensation filtering from Filter 1 and Filter 2.	71
5.25	Cross section and estimated error of SIRF image after compensation filtering.	72
5.26	SIRF image from simulated noisy ERS-1 measurements.	73
5.27	Cross section and estimated error of SIRF image from simulated noisy ERS-1 measurements.	74
5.28	SIRF image after compensation filtering from Filter 2.	75
5.29	Cross section and estimated error of SIRF image from noisy measurements after compensation filtering.	76

5.30	SMMR images from 6.6 GHz vertically polarized measurements. . .	79
5.31	SMMR images from 6.6 GHz horizontally polarized measurements. .	80
5.32	SMMR images from 10.69 GHz vertically polarized measurements. .	81
5.33	SMMR images from 10.69 GHz horizontally polarized measurements.	82
5.34	Compensation filtered images of 6.6 GHz horizontal polarization data from July 15 - 18, Filter 1 and Filter 2.	83
5.35	SASS <i>A</i> images of Greenland.	84
5.36	ERS-1 and SASS <i>A</i> images of the Amazon region.	85
5.37	ERS-1 <i>A</i> image after compensation filtering from Filter 1 and Filter 2.	85

CHAPTER 1

INTRODUCTION

Microwave remote sensing from spaceborne instruments has become a very important method for obtaining data for geophysical studies of the Earth. For example, the study of polar regions is facilitated by spaceborne microwave remote sensing. A complete study of the global climate must include information about the vast ice sheets that cover Greenland and Antarctica. These regions cover about 10% of the Earth's surface area and yet are critical to the regulation of the global climate. They are also believed to be sensitive indicators of changes in climatic trends [1]. The need for continuous monitoring of the polar regions points to the use of spaceborne microwave sensors for two reasons: First, the polar regions are shrouded in darkness and cloud cover for much of the year, which prohibits the use of optical sensors. Second, the polar regions are very remote and inaccessible, which prohibits the gathering of spatially and temporally dense *in situ* measurements. The monitoring of polar ice sheets is one example of many studies that are aided by the repetitive, long term, all-weather coverage from spaceborne microwave remote sensing. Other examples include the determination of soil moisture [2], vegetation mapping [3], and surface temperature monitoring [4].

In many cases, the usefulness of data from spaceborne instruments is limited by low spatial resolution (see for example [2]). Although the spatial resolution of an instrument can be improved by increasing the size of the antenna, this solution is not always practical. Research is underway in the Microwave Earth Remote Sensing Research Group at Brigham Young University to develop post-processing techniques to enhance the resolution of data sets.

Long, Hardin, and Whiting recently developed an enhanced resolution imaging method for Seasat scatterometer (SASS) data [3]. This method, called Scatterometer Iterative Reconstruction with Filter (SIRF), combines the measurements from several satellite passes and uses the spatial overlap of measurement cells to extract information at a higher resolution than that of the individual measurements. This *ad hoc* technique worked very well for SASS data, but when it

was applied to data sets from other instruments, the improvement in resolution was not as dramatic.

As part of the research for this thesis, the SIRF technique was applied to ERS-1 scatterometer data. The technique was also modified and applied to the Seasat Scanning Multichannel Microwave Radiometer (SMMR) data set. In both cases, the resolution of the resulting images was surprisingly low, compared with the resolution enhancement observed in the SASS images. This led to a desire to better understand the limitations of the SIRF technique and to improve the resolution of SIRF images.

In order to observe the performance of the SIRF technique and compare the resolution of SIRF images with the resolution of images generated using other methods, a technique for analyzing images in the wavenumber domain was developed. One-dimensional test images generated using SIRF and two other imaging methods were compared in the wavenumber domain using a definition of resolution based on the error in the image spectrum. This analysis showed that the resolution of an imaging technique is limited by the measurement response, which is determined by the size, shape, and orientation of the measurement cells associated with the underlying data set. This is a significant result because the dependence of the SIRF algorithm on the shape of the measurement cells was not previously understood.

To compare the resolution of the three instruments, SMMR, SASS, and ERS-1, actual data from these instruments were used to create test images and analysis in the wavenumber domain was performed on the test images. For each instrument, a set of actual measurements was used to compute what the measurements would have been if the observed scene was the test image. The SIRF technique was then applied to these synthetic measurements to reconstruct the image. A comparison of the images showed that the resolution of the image created from the SASS data, which were made from long and narrow measurement cells that were oriented in several different directions, was dominated by the short dimension of the measurement cells. This enabled SIRF to generate high resolution images. The SMMR and ERS-1 data were made from measurement cells that were essentially circular. The resolution of the resulting images was dominated by the diameter of the measurement cells; hence, the images did not exhibit as dramatic

improvement in resolution as SASS.

A method for further enhancing the resolution of images through compensation filtering was also developed. The effective measurement response was determined and used to design a filter with the approximate inverse response. By applying this inverse filter and a low pass filter to avoid excessive amplification of high-frequency noise, the measurement response was effectively cancelled out within some bandwidth.

The contributions of this research are: (1) an understanding of the impact of measurement cell shape and orientation on resolution, (2) an understanding of the limitations on resolution enhancement, (3) a method for further resolution enhancement using compensation filtering, (4) a wavenumber analysis technique for comparing the effective resolution of different imaging methods and different instruments, (5) an alternative spectral-based definition of resolution for remote sensing applications, and (6) a modified version of SIRF that is applicable to radiometer data.

This thesis begins in Chapter 2 with the development of the spectral-based definition of resolution and considers some factors that influence resolution. In Chapter 3, different imaging methods are compared under various conditions and the method for enhancing the resolution through compensation filtering is presented. In Chapter 4, some background information about microwave measurements from radiometers and scatterometers is given, after which, each of the instruments considered in this research is described. Chapter 4 also contains a description of the modified SIRF technique as it is applied to SMMR data. Chapter 5 contains the results of a comparison of test images from each of the instruments and presents images from actual data. The conclusions are given in Chapter 6.

CHAPTER 2

RESOLUTION

2.1 Introduction

In this thesis, we look at the problem of creating images from data obtained from several types microwave remote sensing instruments. In particular, we consider three low-resolution spaceborne instruments that were not designed for imaging purposes: the SMMR radiometer and the SASS and ERS-1 scatterometers. These instruments measure electromagnetic energy that is emitted by or backscattered from a distant surface. Each individual measurement has the common characteristic of being a bulk measurement made over a region of the surface.

Consider how a measurement is made. Electromagnetic energy is collected by means of an antenna. A measurement is proportional to the total energy collected. Due to the directional nature of the antenna, the measurement depends mostly on energy transmitted or reflected from a region of the surface that lies within some beamwidth of the antenna. This region is called the *footprint* (see Fig. 2.1). While the footprint identifies the region that is emphasized by the measurement, energy coming from outside of the footprint may also contribute to the measurement via antenna sidelobes. Some instruments, such as the scatterometers discussed in this thesis, use filters or other processors to subdivide the antenna footprint into smaller measurement regions. In these cases, energy from outside of the measurement region may contribute to the measurement via antenna and processing sidelobes. Suppose the observed surface is the x - y plane. The instantaneous weighting function, $f(x, y)$, that governs the amount that each point on the surface contributes to the measurement is simply the normalized antenna/processor radiation pattern projected onto the surface.

The measurement is not made instantaneously, however, but is a temporal average made over some sample period. During the integration time, the antenna usually moves relative to the surface and the instantaneous weighting function moves along the surface. For each measurement, the instantaneous weighting

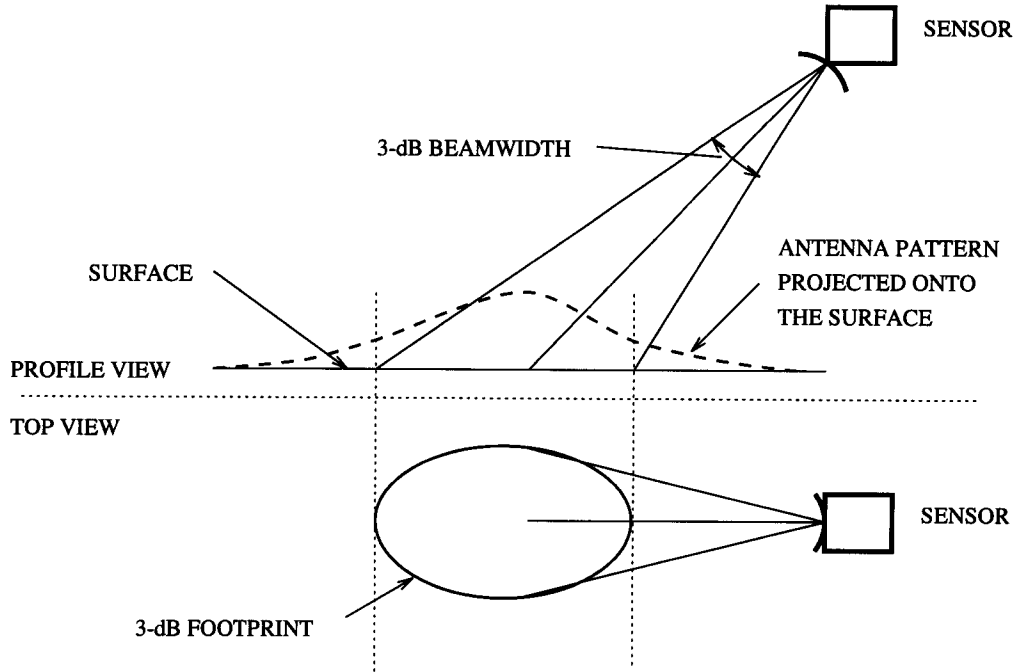


Figure 2.1: Instantaneous footprint and corresponding response pattern.

function becomes smeared into an integrated weighting function, $h(x, y)$ (see Fig. 2.2). Fig. 2.3 shows an example of an instantaneous weighting function and the result of smearing in the x direction.

Given a set of measurements, the r^{th} measurement, z_r , centered at (x_r, y_r) , has an associated weighting function, $h_r(x, y)$. If $s(x, y)$ is the surface response that determines the distribution of energy directed toward the antenna, then each measurement takes the form

$$z_r = \frac{1}{Q_r} \int_{-\infty}^{+\infty} \int_{-\infty}^{+\infty} s(x, y) h_r(x, y) dx dy, \quad (2.1)$$

where

$$Q_r = \int_{-\infty}^{+\infty} \int_{-\infty}^{+\infty} h_r(x, y) dx dy.$$

While the above integrals have limits at infinity, $h_r(x, y)$ is assumed to be zero outside some region surrounding (x_r, y_r) . For example, if the weighting function of Fig. 2.3 is assumed to be negligible below some threshold (typically 3 dB), then the weighting function can be approximated by its main lobe. The region where

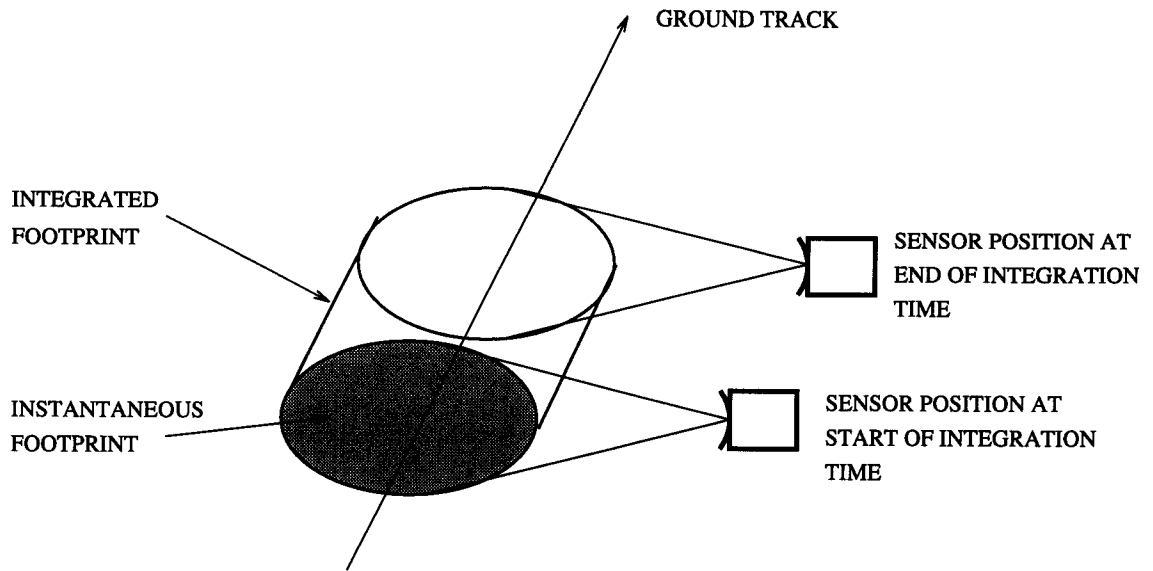


Figure 2.2: Integrated footprint

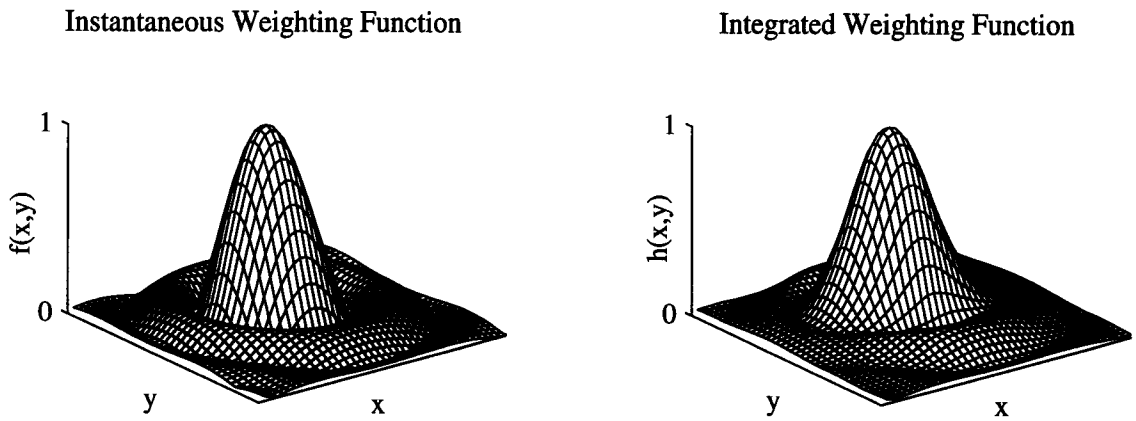


Figure 2.3: Instantaneous and integrated weighting functions.

this approximation is nonzero is called the *measurement cell* and the approximate weighting function is called the *cell response* (see Fig. 2.4).

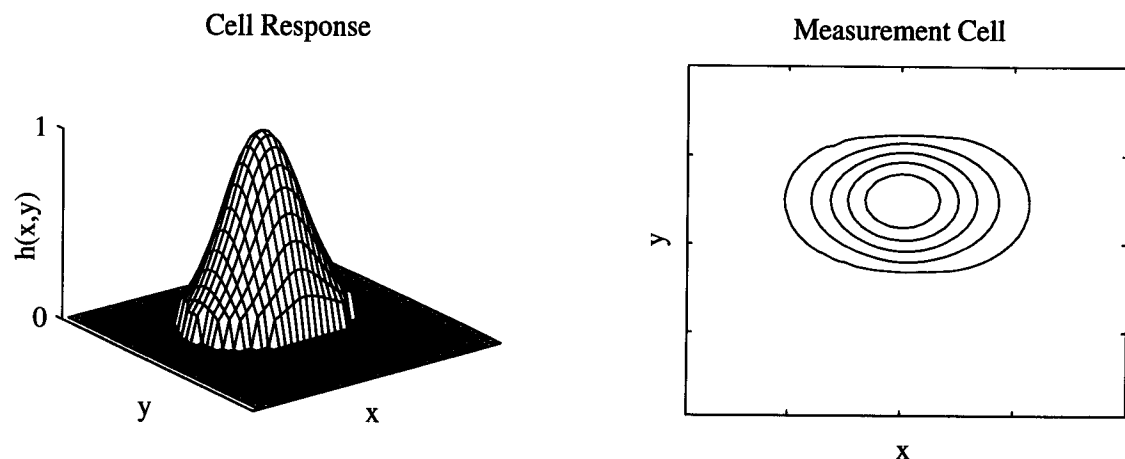


Figure 2.4: Cell response and associated measurement cell.

A data set from which an image can be generated consists of measurements that are distributed over a spatial grid. In order to use the resolution enhancement techniques that will be presented later, the spacing between measurements must be such that there is some overlap between neighboring measurement cells. This spacing does not need to be uniform. The discussion on enhanced resolution imaging that will be presented in this chapter applies to any remote sensing instrument that obtains its measurements in the manner just described.

2.2 Resolution of Remotely Sensed Data

An ideal remote sensing instrument obtains a noise free measurement of the desired surface parameter at each point on the surface. In practice, each individual measurement must be made over a measurement cell with a finite area. Consider a remote sensing instrument that obtains noise-free measurements using a cell response that is identical for all measurement cells. We will examine the resolution of the measurements from such an instrument.

The cell response for the r^{th} measurement is the identical cell response, $h(x, y)$, shifted to the location of the measurement (x_r, y_r) so that $h_r(x, y) =$

$h(x - x_r, y - y_r)$. The expression for the measurements given in Eq. 2.1 can be rewritten as

$$z_r = \frac{1}{Q} \int_{-\infty}^{+\infty} \int_{-\infty}^{+\infty} s(x, y) h(x - x_r, y - y_r) dx dy, \quad (2.2)$$

Equation 2.2 is effectively a normalized two-dimensional convolution integral.

If we assume the measurements are infinitely dense in (x, y) , then the measurements form a continuous function, $z(x, y)$. In this case, the measurements are proportional to the convolution of the surface characteristic with the reversed cell response, i.e.,

$$z(x, y) \propto s(x, y) * h(-x, -y). \quad (2.3)$$

Note that this is the cross-correlation operation, but we will assume that $h(x, y)$ is an even function so that convolution and cross-correlation are identical.

Let us examine the effect of this convolution on the resolution of the measurements by transforming to the spatial-frequency (*wavenumber*) domain. For ease of illustration, we will consider a one-dimensional case. Transformation to the wavenumber domain is accomplished via the Fourier transform (FT) [5], denoted by $\mathcal{F}\{s(x)\} = S(k)$. The inverse Fourier transform (IFT) is denoted by $\mathcal{F}^{-1}\{S(k)\} = s(x)$. Thus, $s(x)$ and $S(k)$ are a FT pair, indicated by $s(x) \leftrightarrow S(k)$. The wavenumber variable, k , is defined as $k = 2\pi/d$, where d is the distance corresponding to the period of a spatial sinusoid. The FT integrals are

$$S(k) = \int_{-\infty}^{+\infty} s(x) e^{-jkx} dx \quad (2.4)$$

$$s(x) = \frac{1}{2\pi} \int_{-\infty}^{+\infty} S(k) e^{jkx} dk. \quad (2.5)$$

A very important property of the FT is that the convolution operation in the spatial domain corresponds to multiplication in the wavenumber domain. Given

$$z(x) = s(x) * h(x), \quad (2.6)$$

then

$$Z(k) = S(k)H(k). \quad (2.7)$$

Assume, for the moment, that the simple indicator function $h(x)$ shown in Fig. 2.5a is the cell response used in making measurements of an impulse, $s(x)$,

in Fig. 2.5c. From the above property and since $h(x) = h(-x)$, the wavenumber spectrum of the measurements, $Z(k)$, will be the product of the wavenumber spectra of the cell response, $H(k)$, and of the surface, $S(k)$, as shown in Fig. 2.5f.

If we consider the measurement spectrum to be a representation of the surface response spectrum, then the difference between the two spectra can be considered error in the measurement spectrum. We now *define* resolution in terms of the fractional error in $Z(k)$. Starting at $k = 0$ and progressing toward $k = \infty$, the resolution of $Z(k)$ is the value of k at which the error, $\epsilon(k)$, first exceeds some threshold value, E , i.e.,

$$\text{resolution} \triangleq \Omega, \text{ such that } \epsilon(k) < E, \text{ for all } k < \Omega, \quad (2.8)$$

where

$$\epsilon(k) = \frac{|S(k) - Z(k)|}{|S(k)|}. \quad (2.9)$$

This definition is an alternative to the traditional definition of resolution: the size of the smallest feature that can be detected in the image. According to the traditional definition, resolution is defined by the extent of the measurement spectrum. The definition of Eq. 2.8 implies that resolution is defined by the accuracy as well as the extent of the measurement spectrum. When this definition is applied to an image, the term “resolution” then refers to the both the quality of the images and the size of the features in the image.

Figure 2.6 illustrates this definition using $S(k)$ and $Z(k)$ from the previous example and $E = 1/2$. Note in this example that the error starts at zero for $k = 0$ and increases as k increases. While this may not always be the case, it is reasonable to assume that when dealing with data from microwave remote sensing instruments, the error of the measurement spectrum will be smallest in the low wavenumber range and gets larger as k increases. Throughout this thesis, we assume that $\epsilon(0) < E$, and that Ω is determined by the point where the error *first* exceeds the threshold. We do not consider the effect of having an error that drops below the threshold for values of k greater than Ω .

For noise-free measurements, resolution is determined solely by the cell response of the sensor. In the following section we consider how resolution is affected by noise in the measurements.

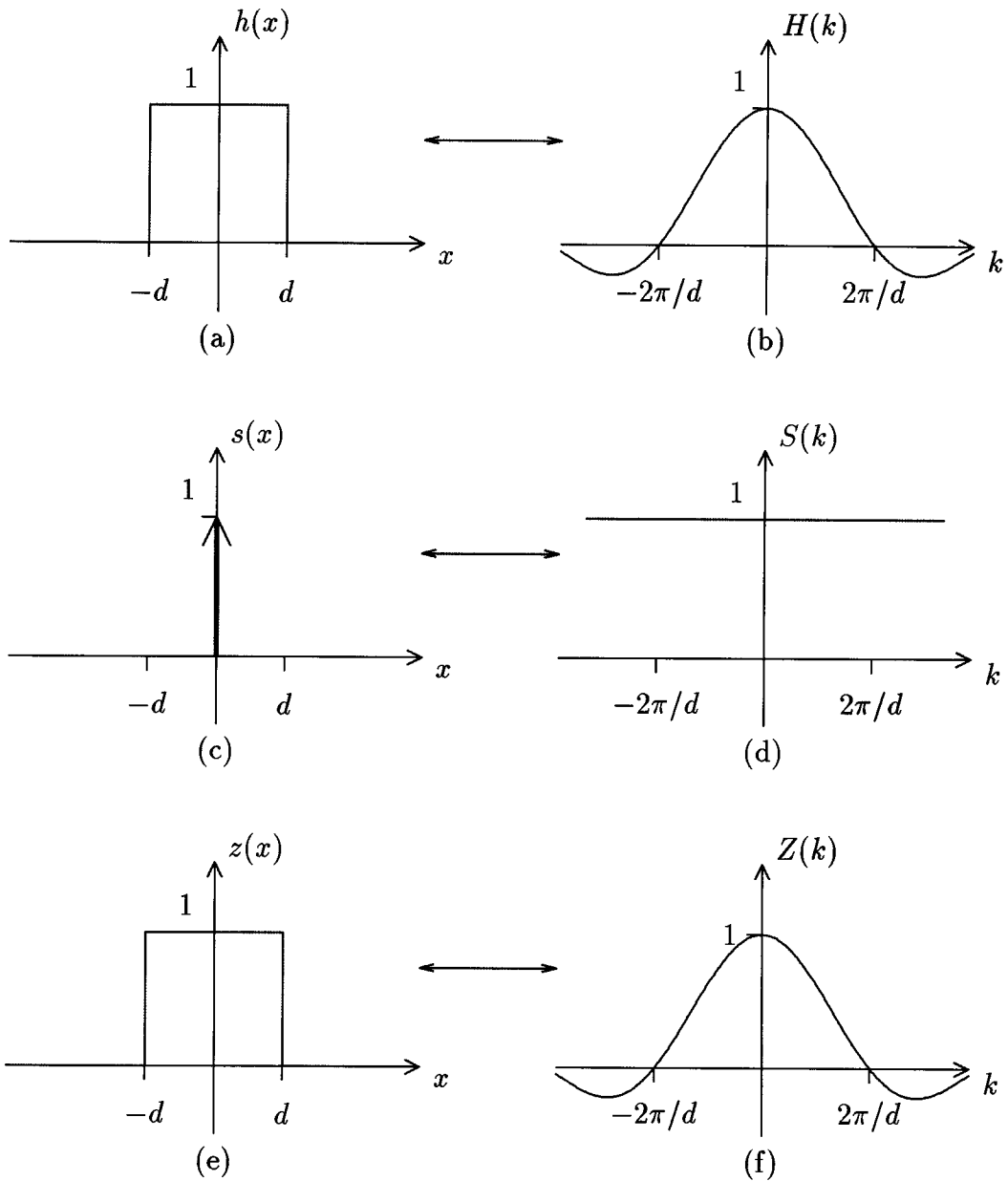


Figure 2.5: (a) cell response, $h(x)$, (b) FT of cell response, $H(k)$, (c) surface response, $s(x)$, (d) FT of surface response, $S(k)$, (e) measurements, $z(x)$ and (f) FT of the measurements, $Z(k)$, all normalized so that the maximum value is 1.

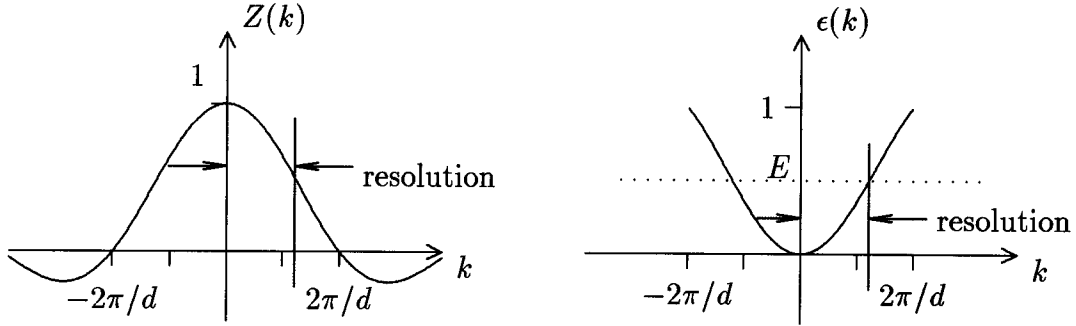


Figure 2.6: $Z(k)$ and the associated error, $\epsilon(k)$, with resolution determined by $E = 1/2$.

2.3 The Effects of Noise

In the previous section, we considered a remote sensing instrument that obtained noise-free measurements using an identical cell response for all measurement cells. Suppose now that noise is introduced into the measurements from the electronics of the remote sensing instrument. Let $v(x)$ denote the noisy measurements,

$$v(x) = z(x) + \eta(x), \quad (2.10)$$

where η is a zero-mean Gaussian random variable with variance σ^2 . Since the FT is a linear process, the wavenumber spectrum of the measurements is given by

$$V(k) = Z(k) + N(k), \quad (2.11)$$

where $N(k) = \mathcal{F}(\eta(x))$ is the noise spectrum. In effect, the noise adds a level of uncertainty to the measurement spectrum. In Fig. 2.7 the noise level, or amount of uncertainty, is depicted as a dashed line. The effective resolution is determined by adding a constant representing the noise level to the measurement spectrum before the error is calculated. The resulting increase in error results in a lower effective resolution.

2.4 Variable Cell Response

In the preceding discussion, it was assumed that all of the measurements were made with an identical cell response. In practice, this is not the case. Changes in position and orientation of the antenna relative to the surface cause differences

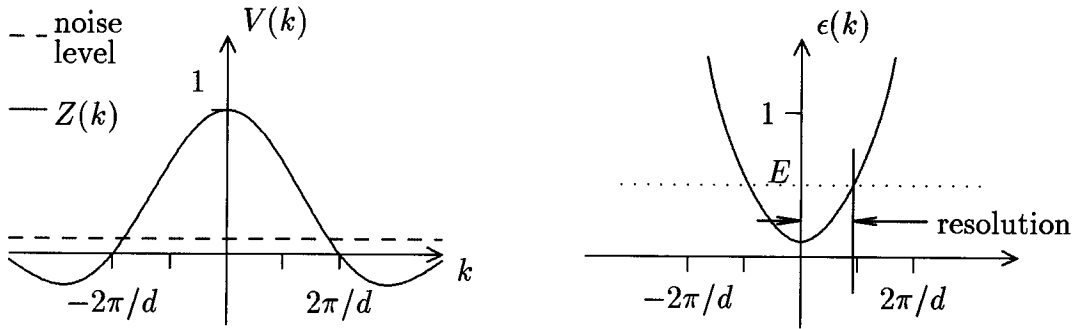


Figure 2.7: Noisy measurement spectrum, $V(k)$, and the associated error, $\epsilon(k)$, with resolution determined by $E = 1/2$.

in the cell response for different measurements. Sometimes these differences are subtle, and the cell response can be assumed to be identical for all measurements. In other instances, the cell response varies greatly for separate measurements. For example, an instrument may use a measurement cell that is long in one dimension and narrow in the other dimension. Any change in orientation of the measurement cell will result in a very different cell response (see Fig. 5.14, page 63). The measurements will then have an effective resolution that is determined by an effective measurement response rather than by the cell response.

In the one-dimensional case, consider a set of measurements for which each measurement is made with either a wide cell response or a narrow cell response. The complete data set can be divided into two subsets based on cell response. Suppose the measurements from each subset are distributed uniformly across the measured surface. Due to the linearity of the FT, the wavenumber spectrum of the complete set is a linear combination of the wavenumber spectra of the two subsets. This idea is illustrated in Fig. 2.8.

In practice, determining the measurement response of the measurements is not as straightforward as summing two sequences. The purpose of this example is to show that the measurement response of a measurement set may be different than the spectrum of any of the individual cell responses.

2.5 Resolution Enhancement

So far we have looked at the resolution of the measurements. We turn our attention now to the images generated from measurements. Suppose an image

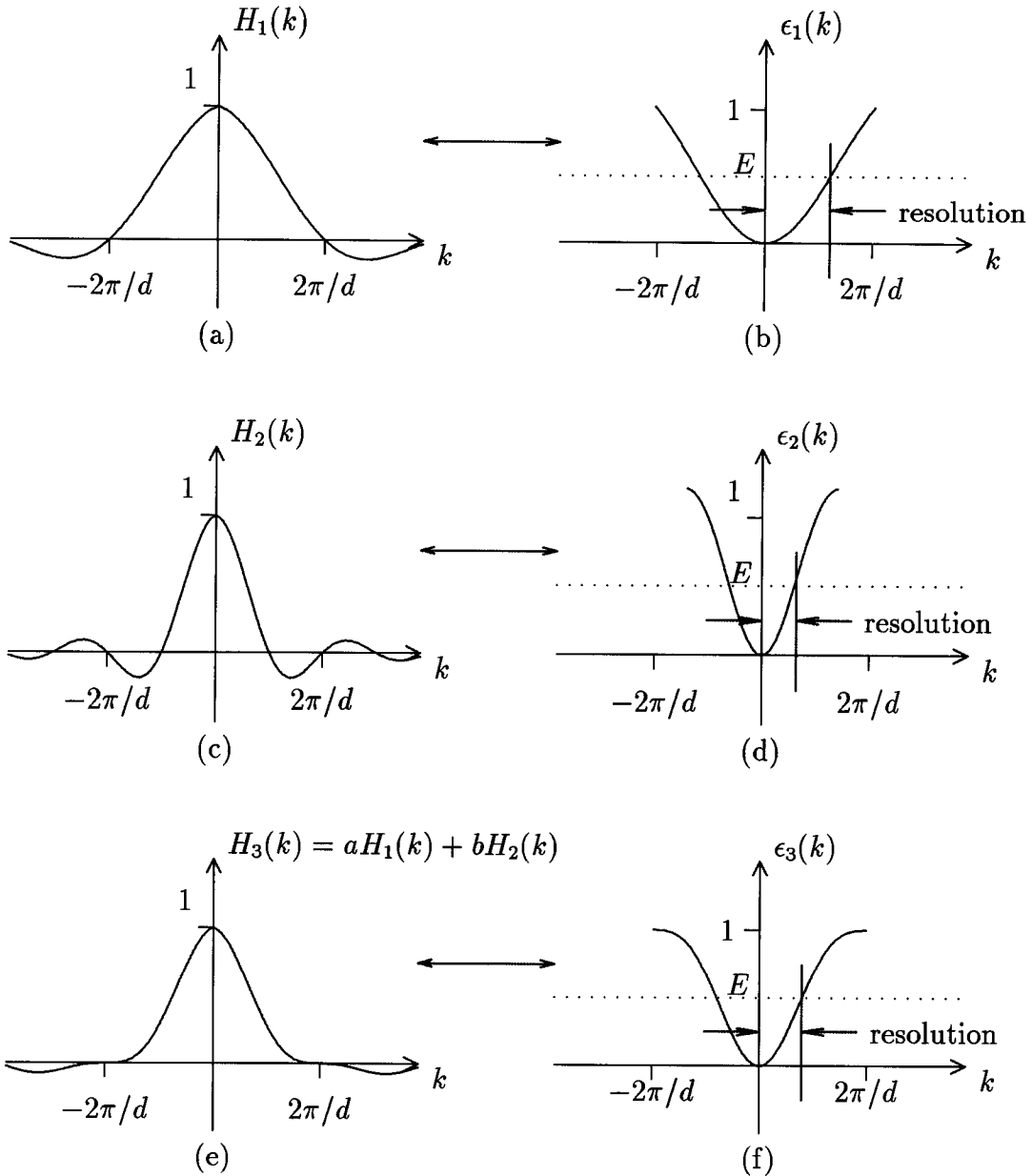


Figure 2.8: (a) FT of first cell response, $H_1(k)$, (b) error of first cell response, $\epsilon_1(k)$, (c) FT of second cell response, $H_2(k)$, (d) error of second cell response, $\epsilon_2(k)$, (e) FT of combined cell responses, $H_3(k)$, and (f) associated error, $\epsilon_3(k)$.

is generated from a set of measurements by superimposing the measurements onto a grid of pixels and assigning each pixel the value of the measurement that is located at its center. Consider the one-dimensional case. If we have a set of measurements, $z(x)$, that are infinitely dense in x , then the pixel values, $p(n)$, are given by

$$p(n) = z(nD), \quad (2.12)$$

where n is the pixel number and D is the spacing between pixels. Such an image is simply a sampled version of the measurement set (see Fig. 2.9). From sampling theory, the wavenumber spectrum of the image is identical to the measurement spectrum with the exception that the low pass spectrum is replicated at intervals of $2\pi/D$. If $P(k)$ is the FT of the image, then

$$P(k) = \frac{1}{D} \sum_{j=-\infty}^{+\infty} Z(k - 2\pi j/D). \quad (2.13)$$

Since the low pass spectrum of the image is essentially identical to the spectrum of the measurements, the resolution of the image is the same as the resolution of the measurements, provided T is sufficiently small to avoid aliasing within the resolution bandwidth.

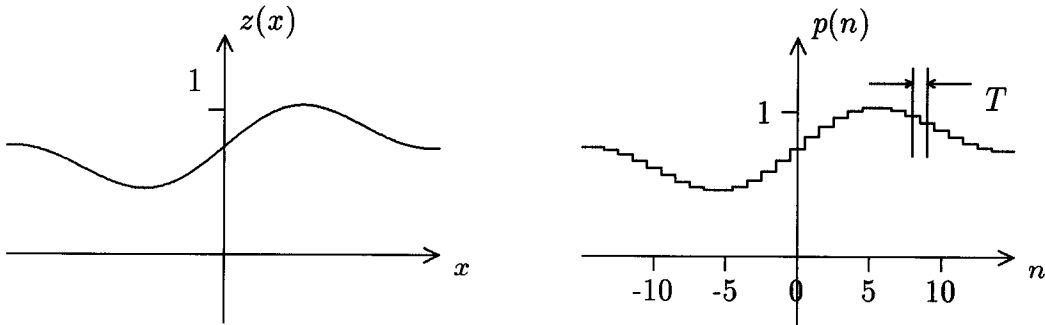


Figure 2.9: Image, $p(n)$, generated by sampling a measurement set, $z(x)$, that is infinitely dense in x .

Given that the cell response used in making the measurements is known, the true spectrum can be recovered from the image spectrum by multiplying by the inverse of the cell response spectrum. For the noise-free case, the true spectrum is exactly recovered from the image spectrum at all points where the cell response spectrum is not zero. This is equivalent to deconvolution of the image with the cell response.

For an image made from noisy measurements, this straight-forward deconvolution approach has the undesirable effect of amplifying the noise along with the signal. While the resolution may be enhanced, the image may still be degraded by excessive noise outside of the resolution bandwidth (see Fig. 2.10). A combination of deconvolution and low pass filtering increases the resolution while lessening the impact of the high-frequency noise.

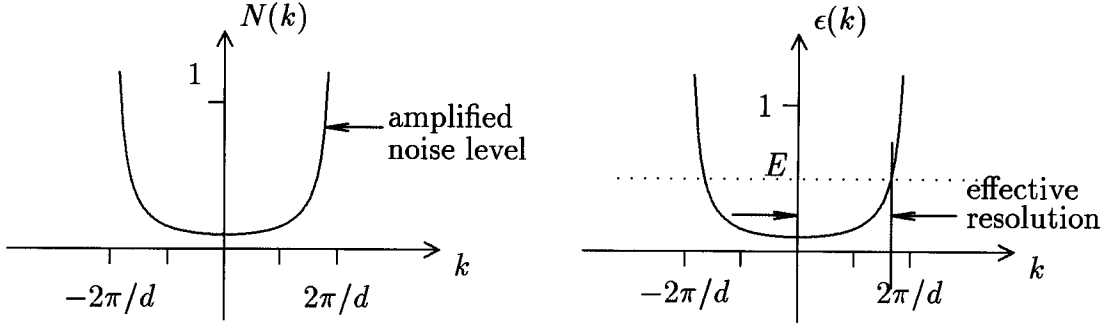


Figure 2.10: Noise level, $N(k)$, of measurements after compensation filtering and the associated error, $\epsilon(k)$, with resolution determined by $E = 1/2$.

A more desirable method would correct the spectrum of the image without amplifying the noise in the spectrum. Intuitively this must involve some form of averaging of the measurements to raise the SNR. Measurements that are close together should contain about the same signal component, while the noise components of the measurements are completely uncorrelated. We have assumed that the noise is introduced by the electronics of the system and is uncorrelated. When an average is taken, the noise component averages to zero while the average of the signal component is the same as the signal component. However, a simple spatial averaging of the image will reduce the resolution.

CHAPTER 3

IMAGING

3.1 Imaging Methods

This section deals with the problem of transferring the information from the measurements to the image pixels. Suppose that the observed surface is broken up into a grid of resolution elements and it is desired to create an image with the pixels corresponding to the resolution elements of the grid. The value of each resolution element is the average of the surface response within its boundaries. Each measurement is the weighted average of the values of all the resolution elements covered by its measurement cell (see Fig. 3.1). The image generation problem is to assign a value to each pixel that is an accurate estimate of the corresponding resolution element based on the measurements.

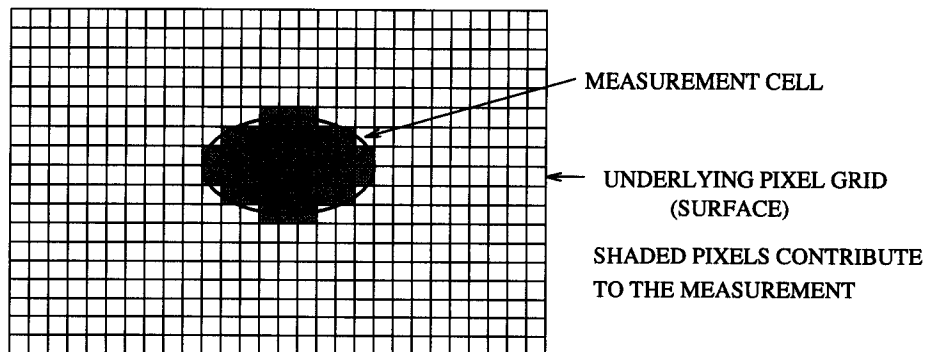


Figure 3.1: Determination of resolution elements that contribute to a measurement.

Much work has gone into developing methods to solve this imaging problem. A detailed summary of some traditional methods are found in [6]. In this chapter, three methods will be considered. Then the effective resolution of these methods will be compared using some simulation examples. Finally, a method for enhancing the resolution through compensation filtering will be presented.

The first imaging method is to superimpose the measurement cells onto the image and assign the value of each measurement to the pixel closest to its center. The values of any unassigned pixels are estimated by interpolating between the measurements (see Fig. 3.2). This method is similar to the sampling method described in Chapter 2, but in this case the measurements are less spatially dense than the pixels. We will call an image generated in this way an *interpolated* image. Depending on the spacing of the measurements, the resolution of the image would be expected to be about the same as the resolution of the measurements. This method involves no averaging of measurements. As a result, the images are very sensitive to noise.

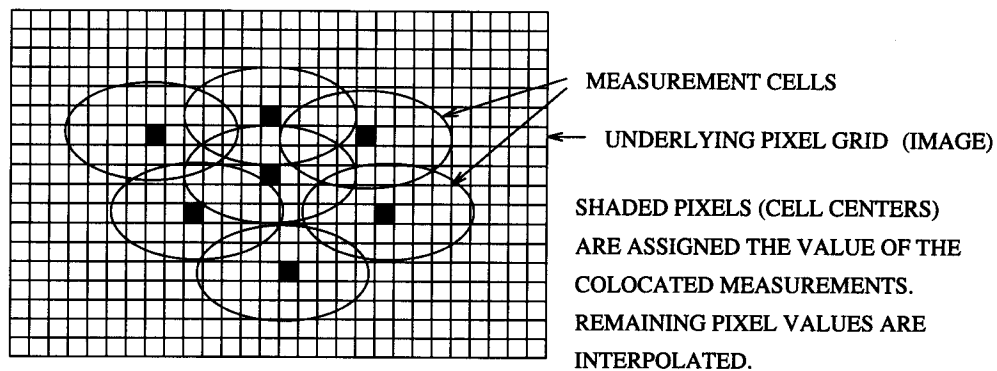


Figure 3.2: Determining pixel estimates from the measurement locations.

As mentioned in Chapter 2, in order for an imaging method to have reduced sensitivity to noise, it must involve some form of averaging of the measurements. Such is the case for the second method, known as AVE. In AVE, a pixel estimate is obtained by taking the weighted average of all of the measurements whose measurement cells cover the pixel (see Fig. 3.3). The weight for each measurement is the measurement's cell response value at the pixel location, so if more than one pixel are within the same overlapping region, their values will differ due to the different weights for each pixel. If $p(m, n)$ is the estimate for the pixel located at (m, n) , and z_r is the r^{th} measurement in the data set, then AVE is

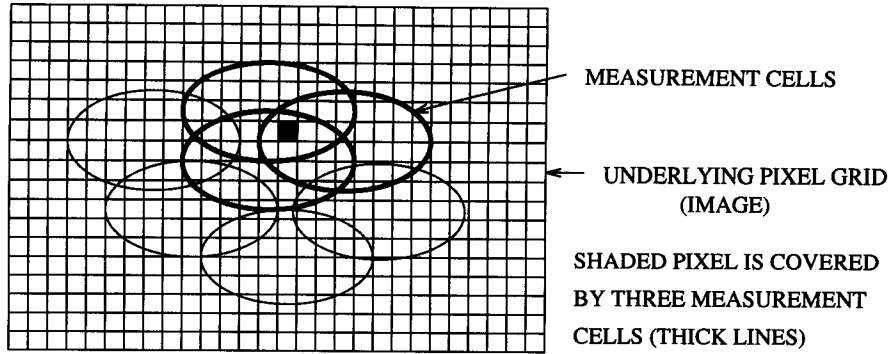


Figure 3.3: Determining pixel estimates from all measurements touching the pixel.

expressed as

$$p(m, n) = \frac{\sum_{r=1}^M z_r h_r(m, n)}{\sum_{r=1}^M h_r(m, n)}, \quad (3.1)$$

where $h_r(m, n)$ is the cell response for the r^{th} measurement at the location (m, n) and the summations are over the M measurements that cover the pixel. While the averaging of this method is helpful for dealing with noisy measurements, it also tends to blur sharp boundaries in the image.

The third method is SIRF, which will be described in detail later. Briefly, SIRF is an iterative approach in which pixel estimates are updated after each iteration by comparing the measurement value to a predicted value based on the current image estimate [3]. Since each pixel obtains an updated estimate for each measurement that covers the pixel, all of the new estimates are averaged together using a non-linear weighting function to obtain the new value. This method generally produces an image with improved resolution over the other two methods and it is also relatively insensitive to noise.

The next sections contain some examples of images generated by the three methods just described. These examples are designed to help gain insights regarding the performance of the methods. Initially, we will consider one-dimensional cases.

3.2 Example 1: Surface Response with Linearly Increasing Wavenumber

The first example uses a surface response function whose wavenumber increases linearly with distance. The function, $s(x)$, shown in Fig. 3.4, is given by

$$s(x) = 10 \times \cos\left(\frac{2\pi x^2}{C}\right), \quad (3.2)$$

so that the wavenumber, $k(x)$ at any point x is

$$k(x) = \frac{4\pi x}{C} \text{ radians/unit distance}, \quad (3.3)$$

where C is used to scale the rate of increase in wavenumber. C is chosen such that the test surface contains features whose sizes range from below to above the limit of resolvability. By using a function that has a one-to-one correspondence between distance and wavenumber, the wavenumber response of the imaging process can be determined directly in the image without transforming to the wavenumber domain.

The measurement cell used to obtain the measurements has a width of 43 units and uses a squared cosine for the cell response. The cell response is shown as the wide cell in the bottom graph of Fig. 3.4. The narrow cell in the figure will be used in a later simulation. The measurement locations were obtained by randomly selecting points with the approximate density of one point for every two pixels. Each measurement was computed by shifting the cell response to the specified location and integrating the product of the surface response and cell response then normalizing by the area under the cell response. The three methods described above were then used to generate one-dimensional images from the measurements. The error was determined using Eq. 2.9 with the appropriate wavenumber spectra computed with a Fast Fourier Transform (FFT).

The first case, shown in Fig. 3.5, is for noise-free measurements. The top graph shows the images generated from the measurements. The middle graph shows the magnitude of the FFT of the cell response. The wavenumber axis on the middle graph corresponds to the pixel (distance) axis on the top graph. Note the null in the FFT of the cell response. Beyond the null point, the measurements are very low and exhibit a 180° phase shift from the true surface. The AVE and SIRF methods were not able to extract any information from the measurements

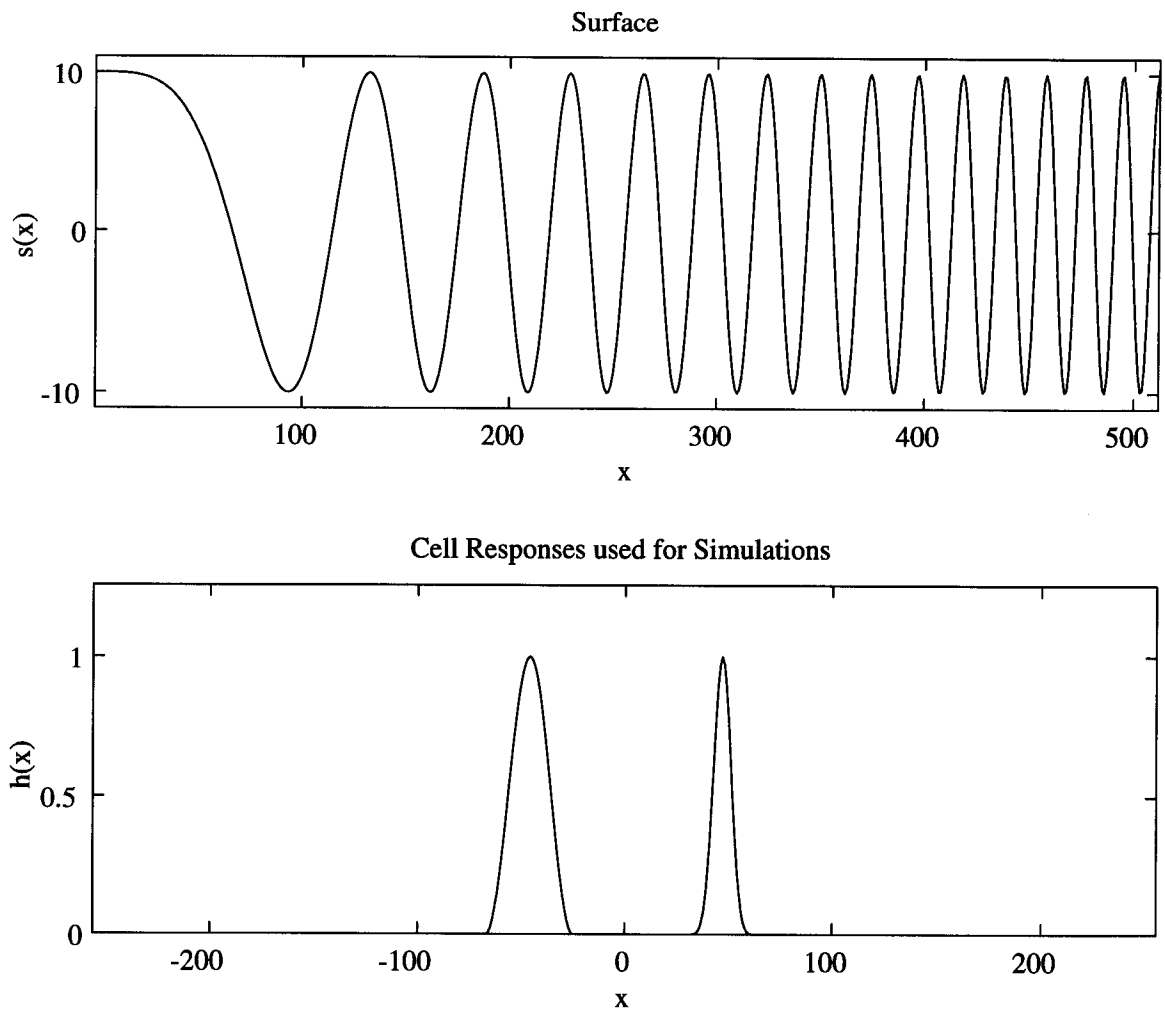


Figure 3.4: Surface response and cell response used for simulations.

at or beyond the null point. This implies that the limit to resolution enhancement achievable through the SIRF method is the wavenumber at which the null occurs.

The resolution of the three estimates can be found from the error curves shown at the bottom of Fig. 3.5. If we determine the resolution of the images from an error threshold of $E = 0.9$, then the wavenumber resolution of the AVE image is about $\Omega = 0.19$ and the wavenumber resolution of the measurements and of the SIRF image are roughly equal at $\Omega = 0.25$. A wavenumber resolution of 0.25 corresponds to a spatial resolution of about 25 units which is slightly larger than the 3-dB width of the cell response. This is close to the traditional definition of resolution of the measurement cell response. The differences in resolution of the three methods is more apparent if a lower error threshold is chosen. For example, for $E = 0.6$, then the wavenumber resolution of the AVE image is about $\Omega = 0.12$, the interpolated image has resolution of about $\Omega = 0.17$, and the resolution of the SIRF image is about $\Omega = 0.2$. Since the differences in performance of the imaging methods is emphasized by a lower error threshold, $E = 0.6$ will be assumed throughout the rest of this thesis.

Next consider the case, shown in Fig. 3.6, where the measurements are noisy. To simulate noise, a Gaussian random sequence with variance $\sigma^2 = 1$ was added to the measurement sequence. Comparing Fig. 3.6 with Fig. 3.5 we can see that the noise has degraded the images, though the degradation is least apparent in the SIRF image.

Comparing the error curves of Fig. 3.6 with those of Fig. 3.5 we see that for all three imaging methods, the error curves follow the same general trends. The curves for the noisy case are more variable than the noise-free case, with a decrease in resolution to $\Omega = 0.16$ for the interpolated image and $\Omega = 0.11$ for the AVE image. The resolution of the SIRF image is essentially the same as for the noise-free case.

Finally, look at the case when two different cell responses are used to obtain measurements. For this simulation, both the wide and narrow cell responses shown in Fig. 3.4 were used. The approximate ratio of measurements made with the narrow cell response to measurements made with the wide cell response was 2/3. The spatial density of the measurements was still about one measurement for every two pixels. Fig. 3.7 shows the images created from these measurements, the

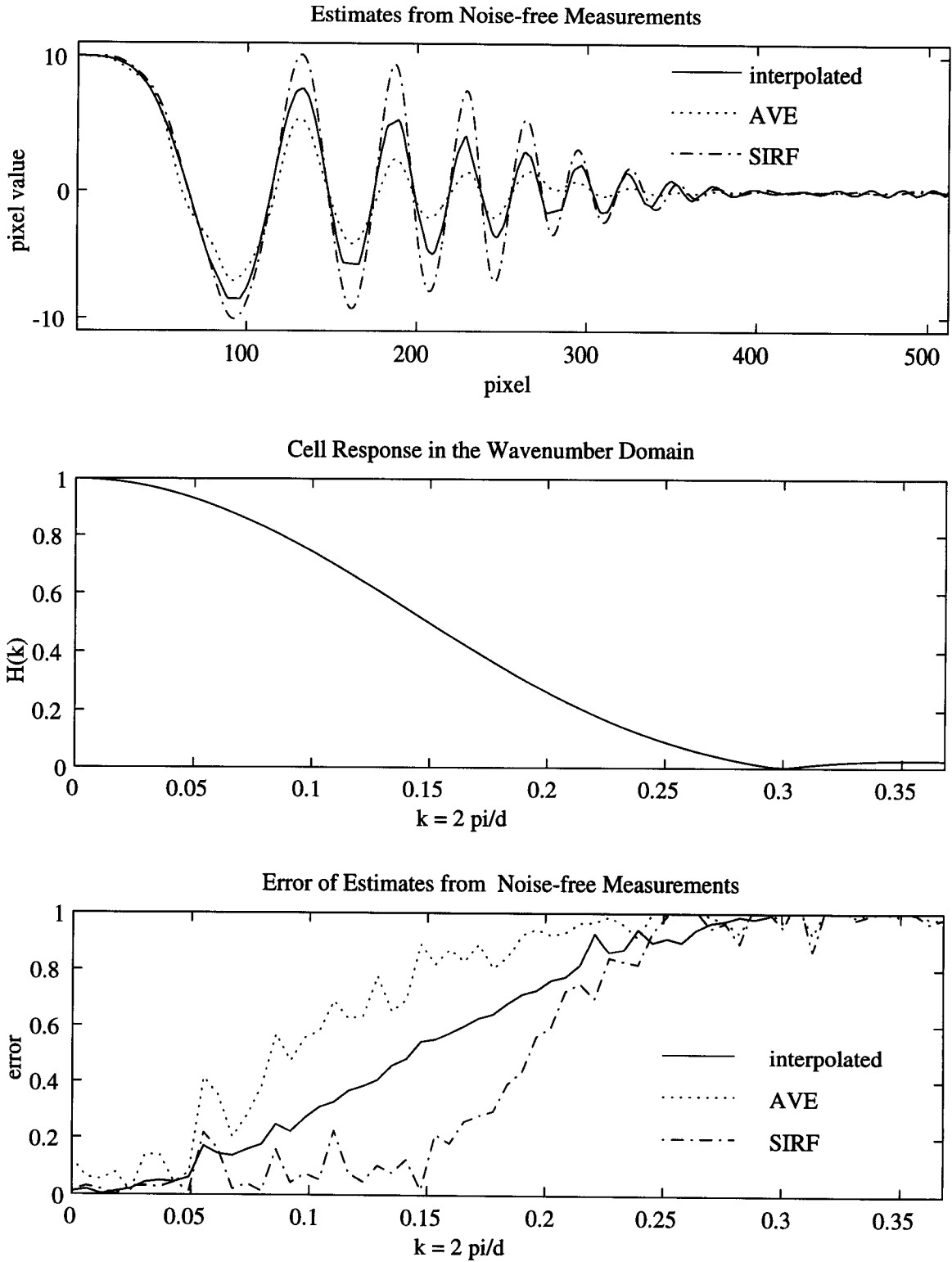


Figure 3.5: Surface response estimates and associated error for noise-free measurements.

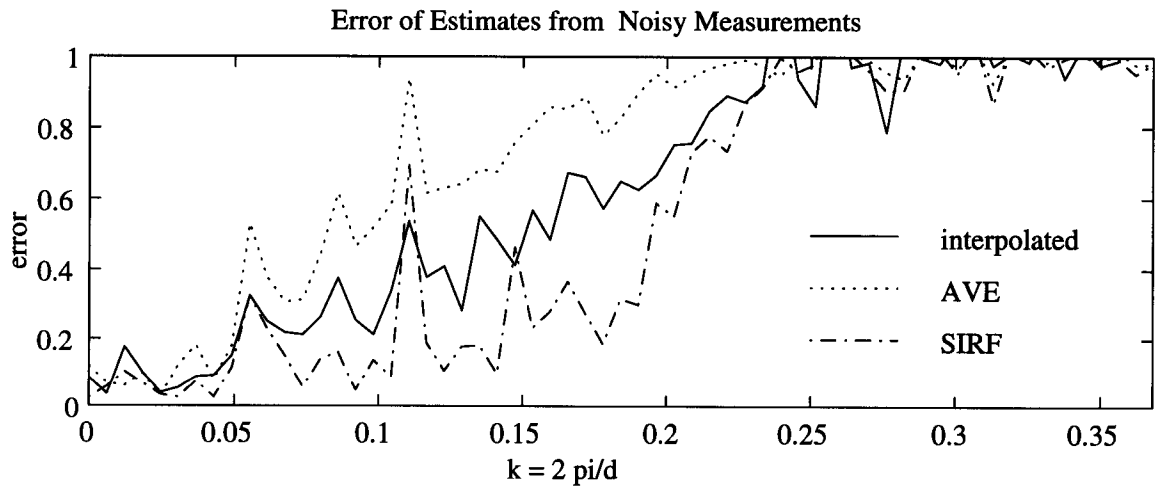
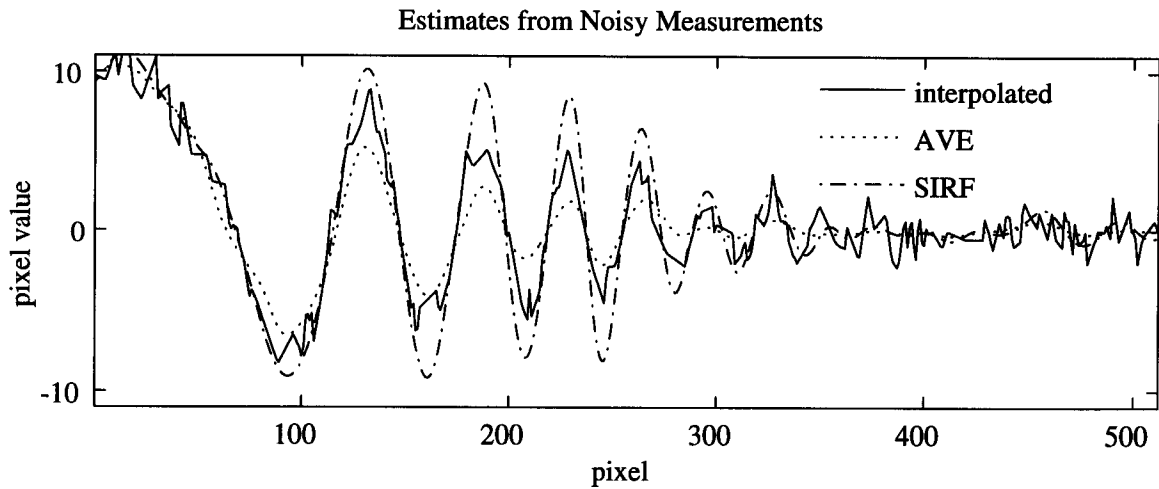


Figure 3.6: Surface response estimates and associated error for noisy measurements.

magnitude of the effective cell response in the wavenumber domain, and the errors of the images. The effective cell response graph was obtained by adding the FFTs of the wide and narrow cell responses, normalizing the sum so that the maximum magnitude is unity, then plotting the magnitude.

While the interpolated image has a jagged appearance due to the mixing of high and low resolution measurements, the roll-off of the peaks in the image closely follows the roll-off of the effective cell response spectrum, which is less steep than when only the wide cell response was used. The SIRF image has been improved in the middle and high wavenumber regions.

Fig. 3.8 shows the error curves for the previous examples grouped according to the imaging method used. Note that while the curves for the noise-free and noisy cases track each other, the error for the mixed cell images is generally lower. For the SIRF method, the error of the mixed cell image is significantly lower in the high wavenumber region.

3.3 Example 2: Resolving Closely Spaced Surface Features

In this example, we look at a simulation that illustrates the differences in resolution of the three imaging methods based on the resolvability of closely spaced features on the observed surface. The procedure for this simulation is the same as in the previous example. The only difference is that the surface response consists only of two closely spaced features of different magnitudes. The surface response and the resulting images and errors are shown in Fig. 3.9. Although the separate features are not distinguishable in any of the estimated images, the amplitude of the tall feature is closer to the true value in the SIRF image than in the other images. Of the three images, the SIRF image is the best estimate of the surface. One undesirable effect of the SIRF method is that some artifacts have been introduced in the image.

3.4 Resolution Enhancement through Filter Compensation

In Example 1, we saw that when an image is created from a set of measurements, the resolution is limited by an effective low pass filter. The wavenumber response of this filter depends on the effective cell response of the measurements

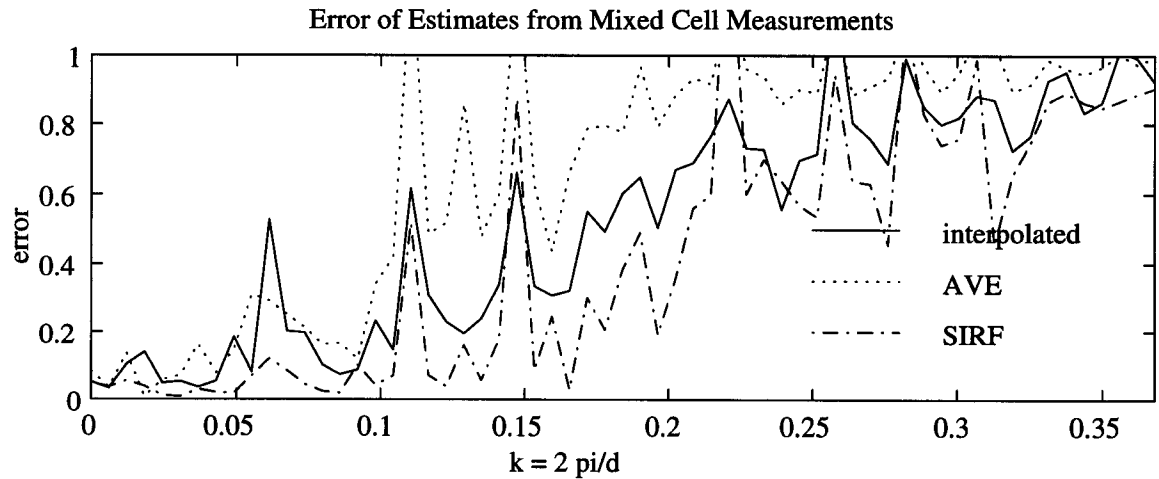
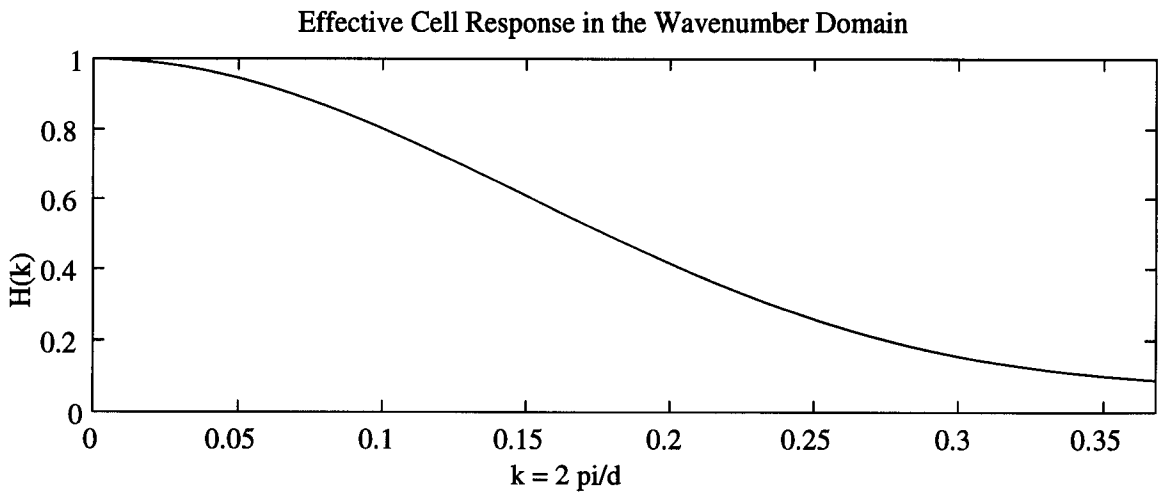
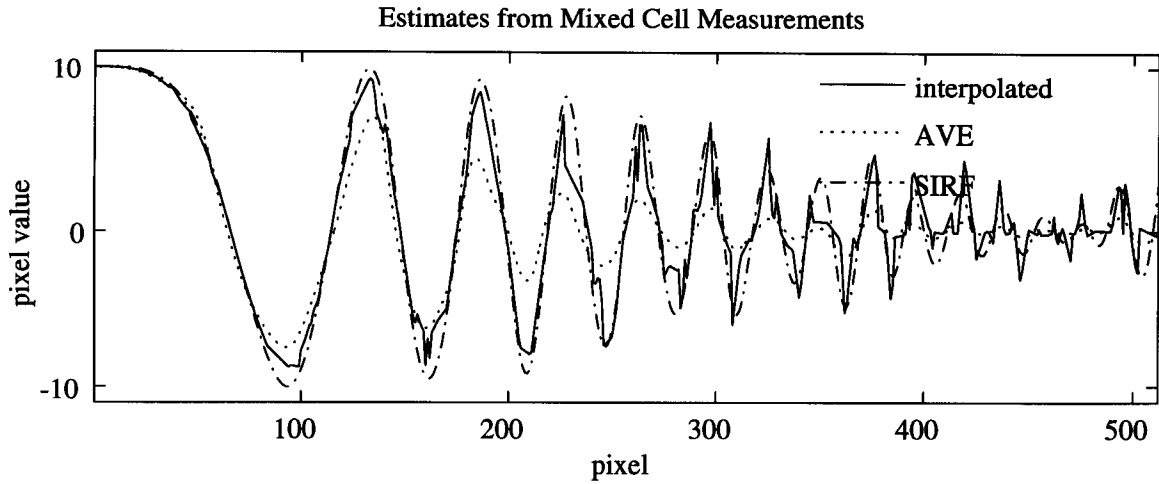


Figure 3.7: Surface response estimates and associated error for mixed measurement cells.

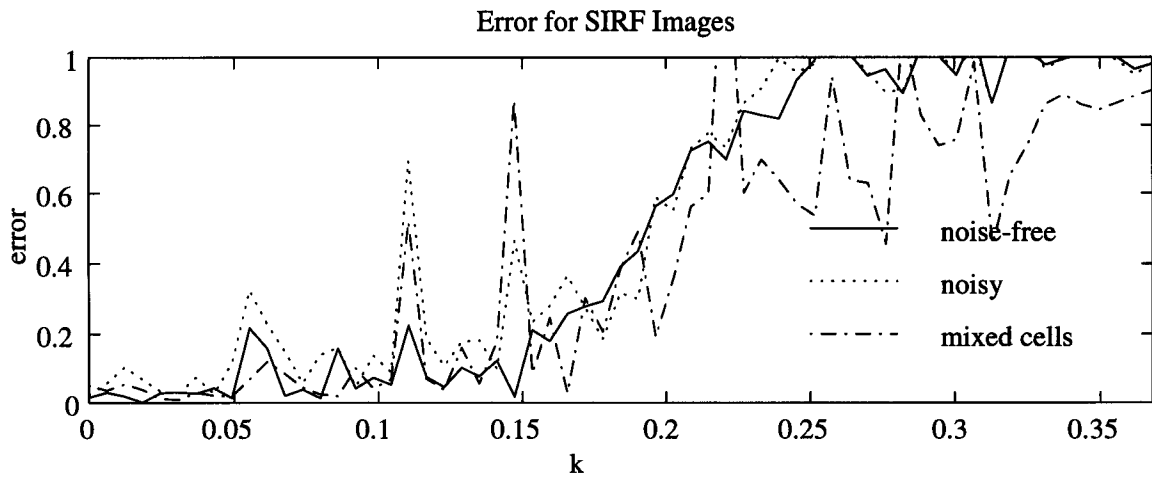
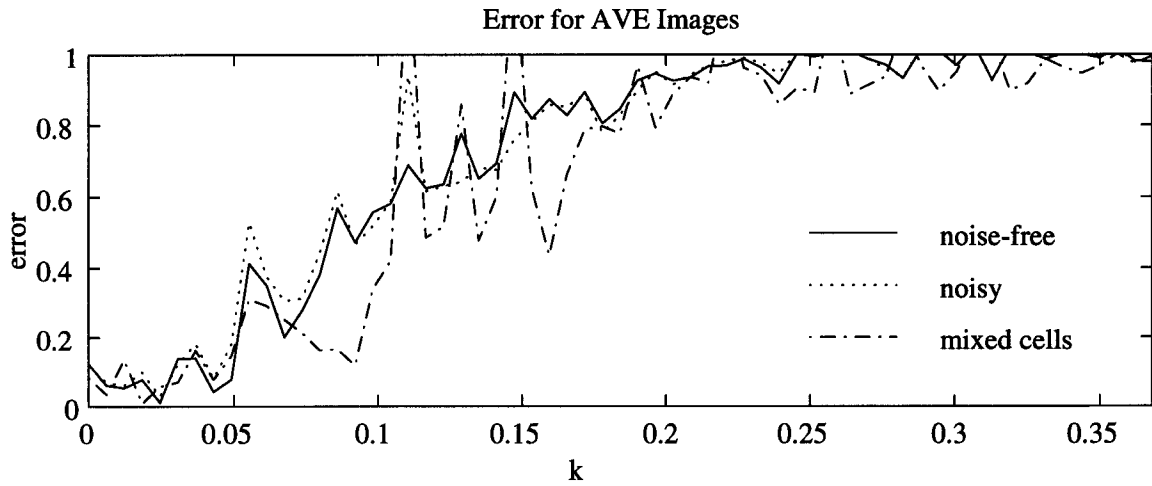
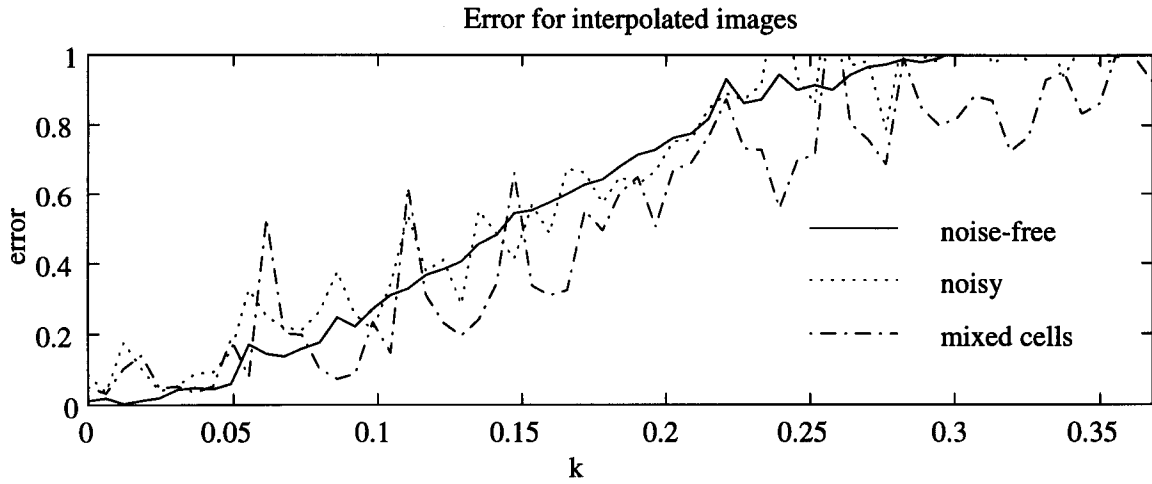


Figure 3.8: Error curves for noise-free, noisy, and mixed cell images.

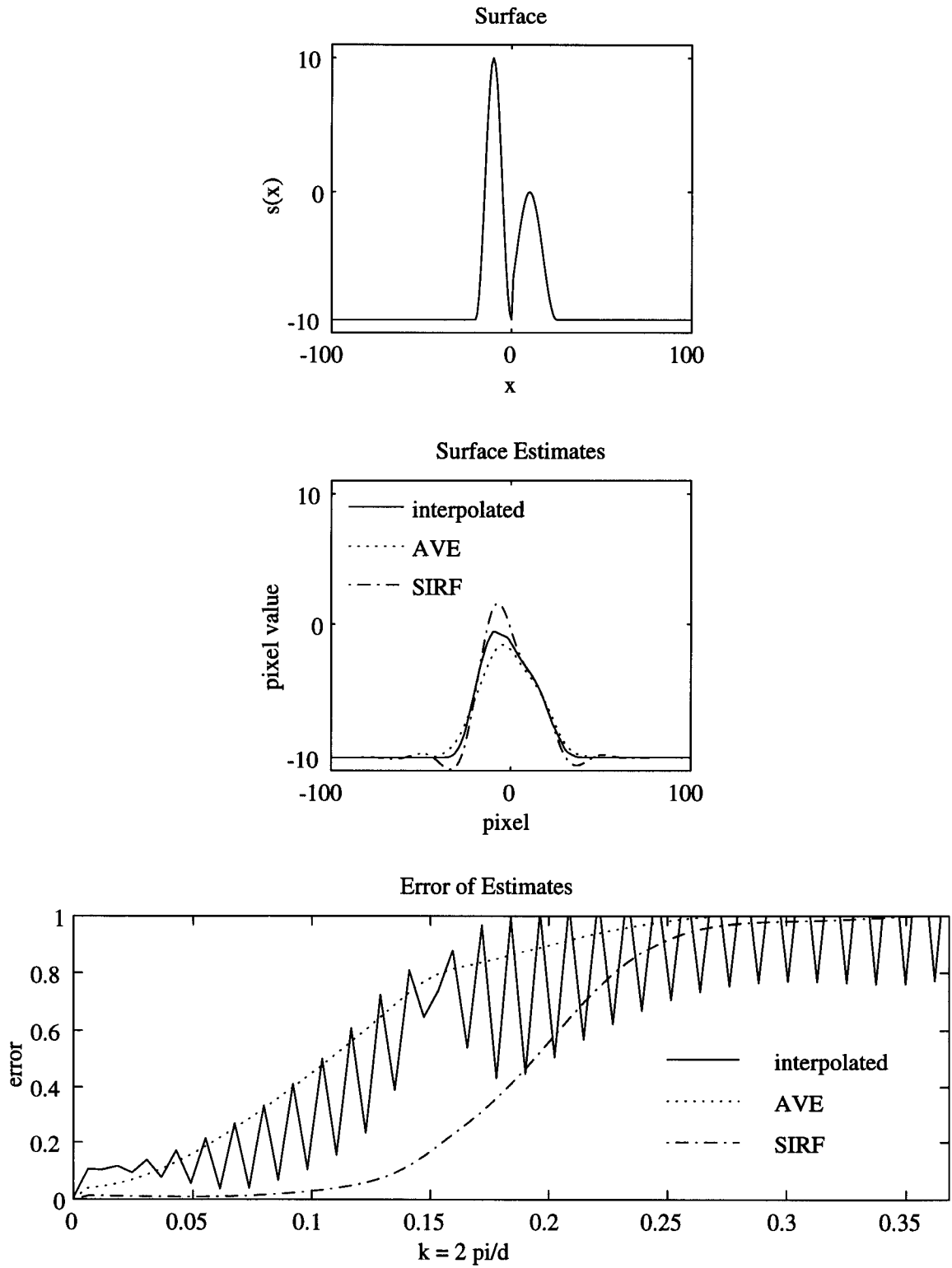


Figure 3.9: Noise-free simulation of resolving closely spaced features.

and on the imaging method used. If this low pass filter response can be determined, then an inverse filter can be applied to the image to enhance the resolution. A method for doing this will be presented in this section.

A simulation image can be generated from a set of real measurements by superimposing the measurement cells onto a simulated surface and calculating what the measurements would have been for that surface. By using a simulation surface whose wavenumber increases linearly with distance, such as that used in Example 1, the wavenumber response of the effective low pass filter can be approximately determined directly from the image. For example, in order to find the effective low pass filter of the SIRF image of Fig. 3.5, one need only plot the normalized magnitude of the envelope of the sequence as shown at the top of Fig. 3.10. Using Eq. 3.3 to convert distance to wavenumber results in the wavenumber domain representation of the filter (see Fig. 3.10 middle). The compensating filter is simply the inverse of the effective low pass filter obtained in this way. As was mentioned in Chapter 2, a straight-forward compensating filter amplifies the noise where the SNR of the image is low, so a low pass filter with cutoff frequency slightly higher than the desired resolution must be used in combination with the compensating filter. The choice of cutoff frequency for the low pass filter is subjective. In this example, the cutoff was chosen at $k = 0.25$, because that is close to the edge of the stop band of the effective low pass filter. The resulting compensation filter is shown at the bottom of Fig. 3.10.

Fig. 3.11 shows the results of applying the compensating filter to the SIRF image of Fig. 3.5. Notice that the levels of the peaks have been brought closer to the true value in the middle region. The error curves also show that for the middle wavenumber range, the error has been decreased by compensation filtering. For $E = 0.6$, the resolution has been increased from about $\Omega = 0.2$ to $\Omega = 0.22$. At $k = 0.25$, the error has been increased slightly by the compensating filter due to the cutoff of the low pass filter. This technique has the drawback of introducing some artifacts into the image as a result of the sidelobes of the compensating filter. This is evident in the left side of the image between pixels 0 and 100 where the image is somewhat misshapen.

Fig. 3.12 shows the effect of compensation filtering on the resolvability of image features. Applying the compensating filter to the SIRF image from Fig. 3.9

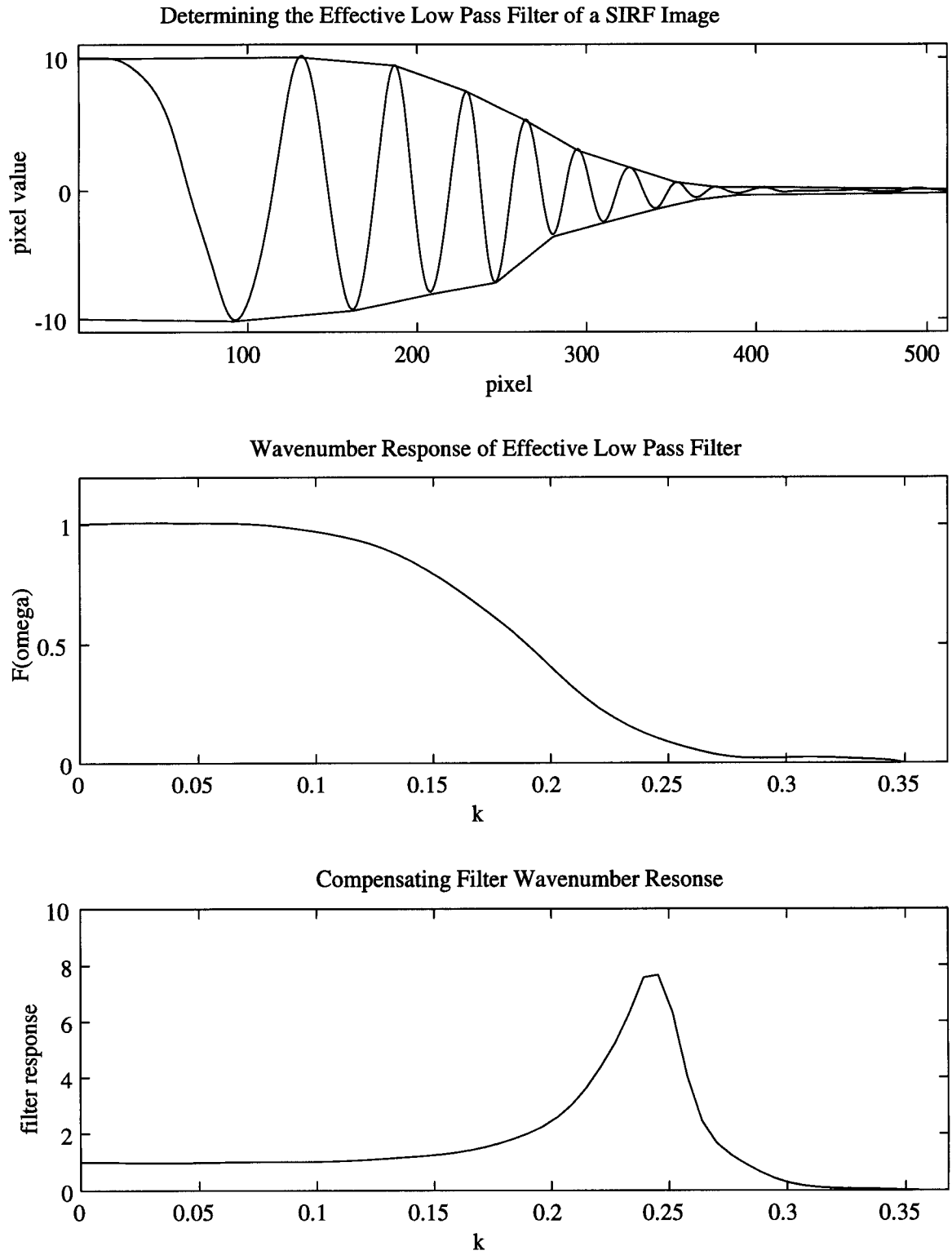


Figure 3.10: Determining the effective low pass filter and inverse filter.

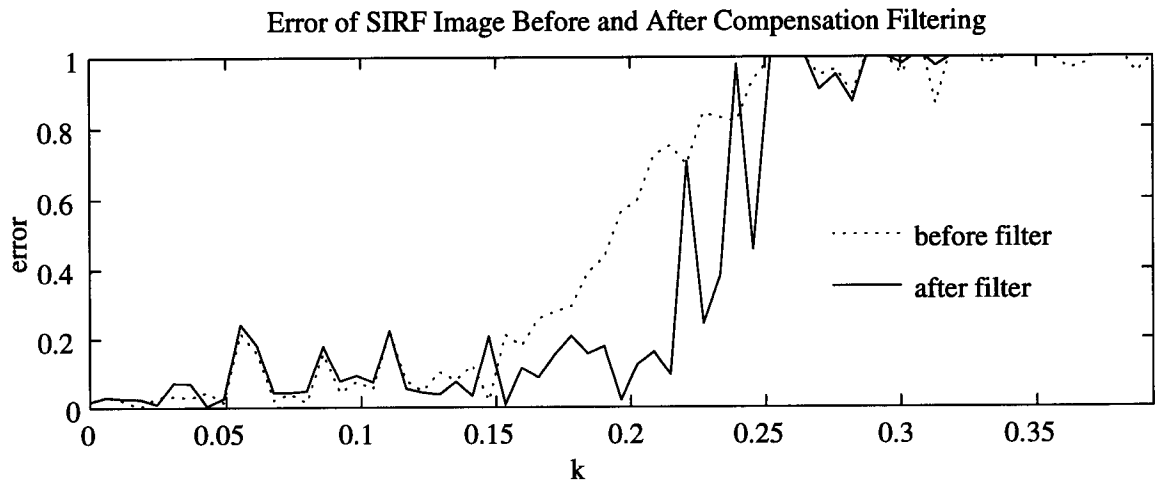
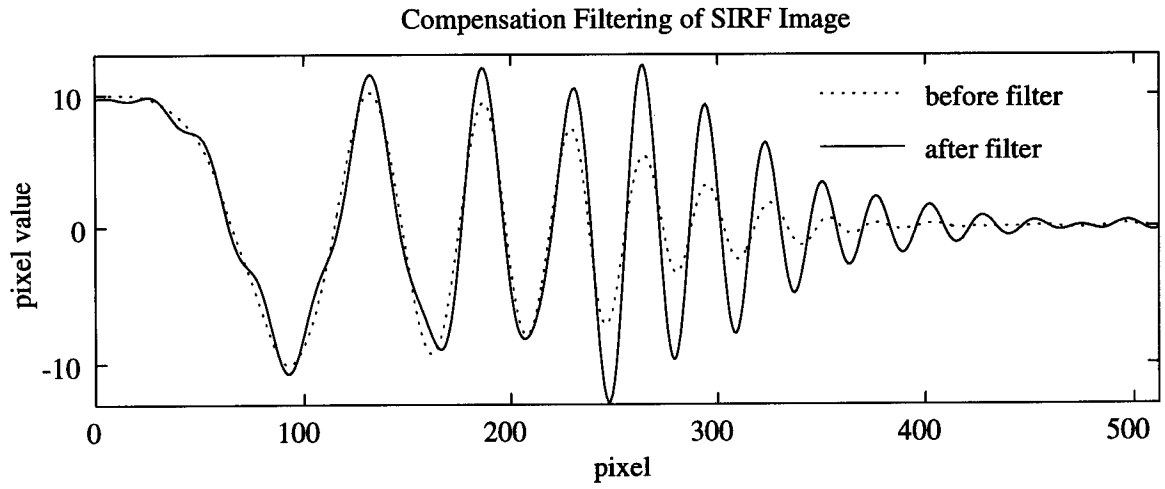


Figure 3.11: Enhancing image resolution through compensation filtering.

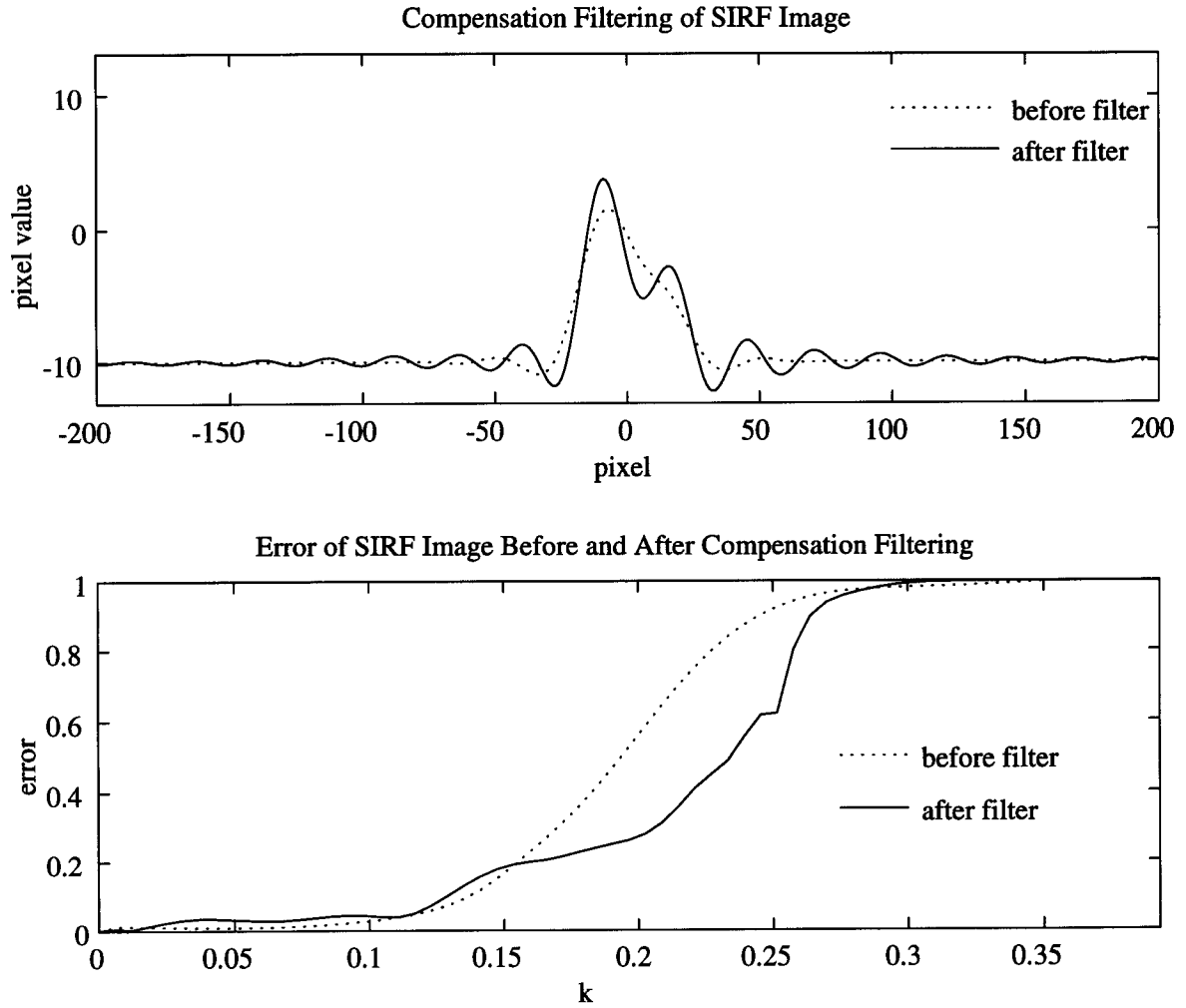


Figure 3.12: Increasing feature resolvability through compensation filtering.

helps to localize the two features in the image and bring their values closer to the true levels. The two features were not clearly distinguishable in any of the previous examples as they are in this filtered image. Again, the artifacts introduced by the filter sidelobes are clearly evident. These artifacts could be lessened by carefully choosing a low pass filter that has low sidelobes in the spatial domain.

3.5 Summary

In this chapter we looked at the effective resolution of three imaging techniques: interpolation, AVE and SIRF. The effective resolution of these methods was compared by determining the error of the wavenumber spectra of one-dimensional simulation images from noise-free measurements, noisy measurements, and measurements from mixed cell responses. In all cases, the SIRF image had the highest resolution. The resolution was limited, however, by an effective low pass filter inherent in the measurement process. By applying an inverse filter to compensate for this inherent low pass filter, the resolution of the images was improved. In the following chapters, the resolution of SIRF images generated from measurements from real instruments will be examined.

CHAPTER 4

IMAGE RECONSTRUCTION FROM MICROWAVE DATA

This chapter covers both the motivation for creating images from radiometer and scatterometer data and the processing methods used for the SMMR data set. Because this research has focused primarily on radiometric data, in particular from the SMMR instrument, we will begin with a rather detailed summary of radiometric quantities and a description of the SMMR instrument. A review of scatterometry is also included with brief instrument descriptions of SASS and the ERS-1 scatterometer. These sections will be followed by a discussion of some considerations regarding the SMMR data set that have an impact on the imaging process and then by a description of the SIRF algorithm that was modified to be applicable to SMMR data. Since the SIRF algorithm as it was developed for SASS is described in detail in [6], it will not be presented here.

4.1 Basics of Microwave Measurements

4.1.1 Radiometry

This section is a summary of radiometric quantities. A more detailed discussion can be found in [7]. A radiometer is an instrument that measures the incoherent electromagnetic energy emitted by some source. All materials contain internal thermal energy which is transformed to electromagnetic energy and is emitted. The term *brightness* B is used to describe the amount of emitted energy (power) that is transmitted and is given by

$$B = \frac{F_s}{A_s}, \quad (4.1)$$

where

$$\begin{aligned} F_s &= \text{radiation intensity of the source, W sr}^{-1} \\ A_s &= \text{area of the source region, m}^2. \end{aligned}$$

The brightness over a region typically is not spatially constant, hence the indices (θ, ϕ) , which are the azimuth and elevation angles relative to an observation point, are introduced to show the spatial variation. Furthermore, the emission from a surface is spectral in nature and may vary with frequency. Incorporating these two properties, *spectral brightness* $B_f(\theta, \phi)$ is defined as the brightness per unit bandwidth.

A *blackbody*, which is an ideal material that emits all absorbed energy, provides a reference for the brightness of real materials. In most of the microwave region, the spectral brightness of a blackbody is given approximately by

$$B_f(\theta, \phi) = \frac{2kT(\theta, \phi)}{\lambda^2}, \quad (4.2)$$

where

$$\begin{aligned} k &= \text{Boltzmann's constant} = 1.38 \times 10^{-23} \text{joule K}^{-1} \\ T &= \text{absolute temperature, K} \\ \lambda &= \text{electromagnetic wavelength, m.} \end{aligned}$$

Therefore, for a narrow bandwidth Δf , the brightness $B_{bb}(\theta, \phi)$ for a blackbody is

$$B_{bb}(\theta, \phi) = \frac{2kT(\theta, \phi)}{\lambda^2} \Delta f. \quad (4.3)$$

Real materials do not emit as much energy at a given temperature as a blackbody. The brightness for a real material can be expressed in the same form as Eq. 4.3 with the introduction of a radiometric temperature, called the *brightness temperature* $T_B(\theta, \phi)$. So for real materials,

$$B(\theta, \phi) = \frac{2kT_B(\theta, \phi)}{\lambda^2} \Delta f. \quad (4.4)$$

Dividing Eq. 4.3 into Eq. 4.4 gives a property of the real material known as *emissivity* $e(\theta, \phi)$:

$$e(\theta, \phi) = \frac{B(\theta, \phi)}{B_{bb}(\theta, \phi)} = \frac{T_B(\theta, \phi)}{T(\theta, \phi)}. \quad (4.5)$$

This relationship between brightness temperature, absolute temperature, and emissivity points to two possibilities for surface imaging from radiometer measurements. In a region of only slightly varying emissivity, surface temperature would be apparent in the image. In a region of greatly varying emissivity, differences in the

surface parameters would be evident, allowing for discrimination between surface types.

Ideally, a spaceborne radiometer would be able to measure the brightness temperature of the earth's surface due only to the self-emitted radiation from the terrain. The truth is that the power detected by the radiometer contains additional components from upwelling atmospheric emission as well as radiation that is scattered by the terrain rather than emitted by it. Also, those components that propagate through the atmosphere are attenuated before they reach the radiometer. The term *apparent temperature* $T_{AP}(\theta, \phi)$ refers to the brightness $B_i(\theta, \phi)$ observed at the radiometer antenna and is defined similar to Eq. 4.4 as

$$B_i(\theta, \phi) = \frac{2kT_{AP}(\theta, \phi)}{\lambda^2} \Delta f. \quad (4.6)$$

The *antenna temperature* T_A , which is the actual measurement made by the radiometer, is calculated as the weighted average of the apparent brightness with the antenna pattern $F_n(\theta, \phi)$ as the weighting function.

$$T_A = \frac{1}{Q} \int_0^\pi \int_0^{2\pi} T_{AP}(\theta, \phi) F_n(\theta, \phi) d\theta d\phi, \quad (4.7)$$

$$Q = \int_0^\pi \int_0^{2\pi} F_n(\theta, \phi) d\theta d\phi.$$

4.1.2 Scatterometry

A scatterometer is an active microwave instrument that transmits electromagnetic energy toward a surface and measures the amount of backscattered energy. The surface characteristic that determines the amount of backscattered energy is known as the normalized radar cross section (σ°) and is defined by the basic radar equation [8]

$$\sigma^\circ = \frac{P_R(4\pi)^3 R^4}{P_T G^2 \lambda^2 A} \quad (4.8)$$

where P_R is the received power, R is the range of the instrument to the surface, P_T is the transmitted power, G is the antenna gain, λ is the wavelength of the transmitted energy, and A is the effective area of illumination at the surface.

Scatterometer measurements of σ° have proven to be useful for mapping surface characteristics such as vegetation types [3, 9]. Over land and for incidence

angles in the range of 20° to 60° , σ° exhibits an approximately linear dependence on the measurement incidence angle [9]. A commonly used model for relating σ° to incidence angle is [3, 6, 9]

$$10 \log_{10} \sigma^\circ(\theta) = \mathcal{A} + \mathcal{B}(\theta - 40^\circ), \quad (4.9)$$

where θ is the measurement incidence angle and \mathcal{A} and \mathcal{B} are constants that depend on the characteristics of the observed surface. Scatterometer measurements can therefore be used to create images representing \mathcal{A} and \mathcal{B} , from which information about the observed surface can be inferred.

4.2 Instrument Descriptions

4.2.1 SMMR

SMMR, which was part of the 1978 Seasat mission, was a 5-frequency microwave radiometer that measured dual-polarized radiation at frequencies of 6.6, 10.69, 18.0, 21.0, and 37.0 GHz. It had a scanning antenna system consisting of an offset parabolic reflector that was mounted over a multifrequency feed horn. The reflector was mechanically scanned over a 50° swath angle that extended from 3° on the port side to 47° on the starboard side of the subsatellite track (Fig. 4.1). The scan velocity varied sinusoidally with a scan period of 4.096 seconds [10].

The SMMR instantaneous footprint was an ellipse-like area. The dimensions depended on the frequency of the received radiation. The scan was continuous, however, and during sampling periods, the footprints became smeared into integrated footprints. Due to the sinusoidally varying velocity of the scanning reflector, the integrated footprints were larger near the center of the swath than at the swath edges. The sample period also depended on frequency. The sample periods were 30 ms for 37.0 GHz, 126 ms for 6.6 GHz, and 62 ms for all other frequencies. There was a 2 ms data dump period between sample periods for digitization and transmission of the sampled radiation data. Figure 4.2 shows the relative sizes of the instantaneous footprints and the integrated footprints.

SMMR alternated taking measurements of horizontal and vertical polarization for the four lowest frequencies. The vertical polarization measurements were taken in the first half of the scan and the horizontal polarization measurements were taken in the second half of the scan.

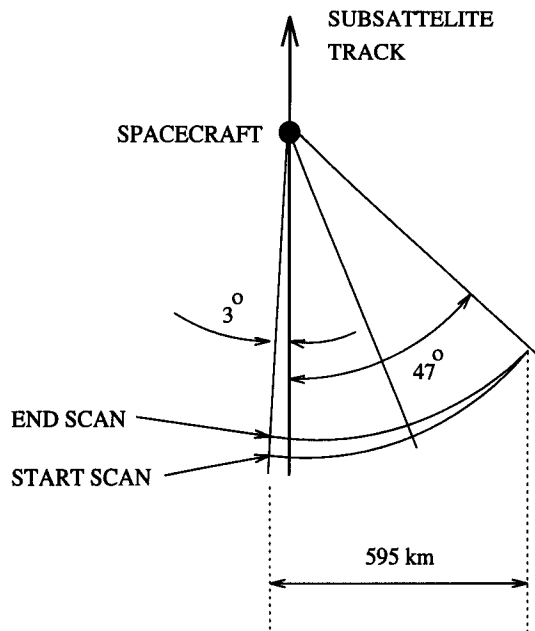
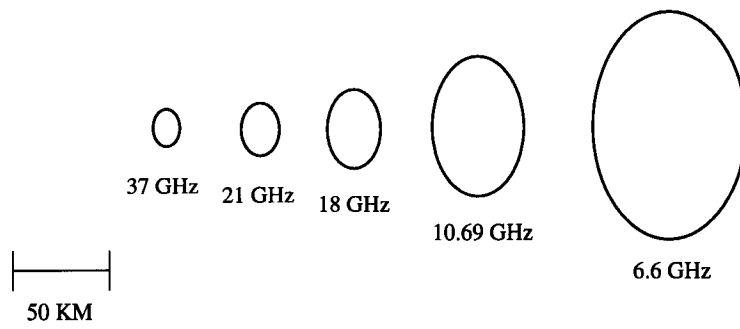


Figure 4.1: SMMR swath relative to the direction of travel of the spacecraft.

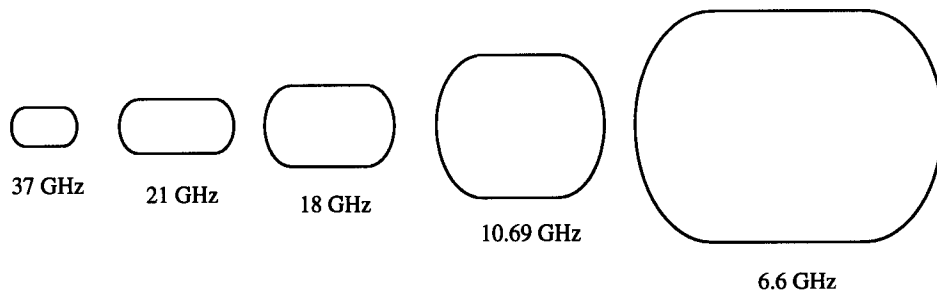
4.2.2 SASS and ERS-1 Scatterometers

SASS, which was also part of the 1978 Seasat mission, used four dual-polarized fan-beam antennas that were arranged at azimuth angles of 45° and 135° from the satellite ground track (Fig. 4.3). Doppler filters were used to divide the footprint into resolution cells. The integration time for each measurement was 1.89 s, during which the instantaneous resolution cells were smeared into integrated measurement cells (Fig. 4.4). The measurement cells were therefore long and narrow. The sizes of the measurement cells varied depending on their location within the antenna footprint. The cells in the near swath were smaller than the far swath cells. For simplicity in generating images, the cell response was assumed to be unity inside the cell and zero outside the cell. The four antennas were rotated through a 7.56-s measurement period in which only one antenna was active at any given time. The time between measurements was such that the cells were spaced 50 km apart in the along-track direction [11].

The ERS-1 scatterometer, which is currently operational, uses three side-looking antennas with the beams pointed at angles of 45° , 90° , and 135° from



SMMR Instantaneous 3-dB Footprint - Relative Sizes



SMMR Integrated 3-dB Footprint - Relative Sizes

(Note: These sizes vary with scan position.)

Figure 4.2: SMMR footprints

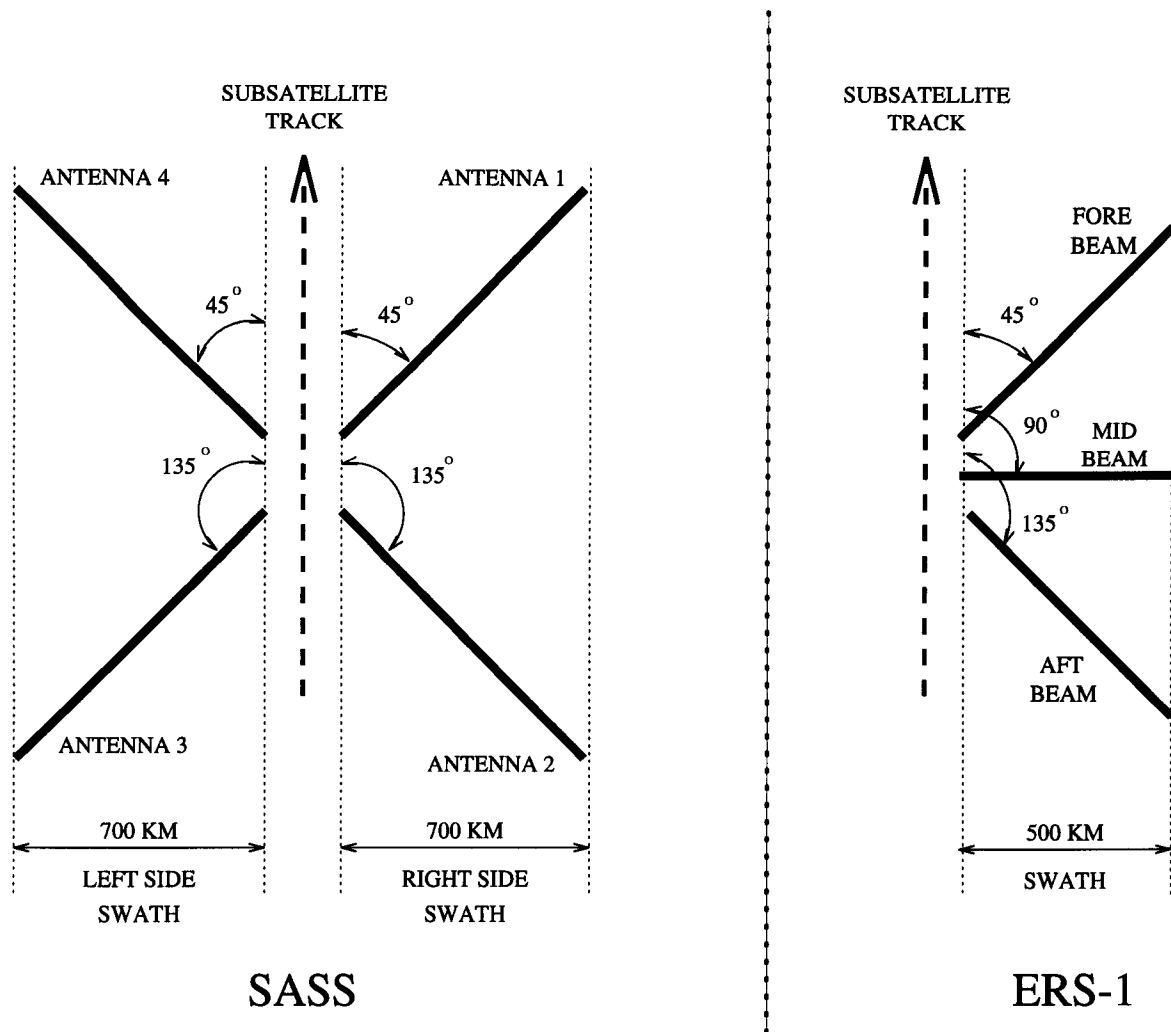


Figure 4.3: SASS and ERS-1 antenna illumination patterns

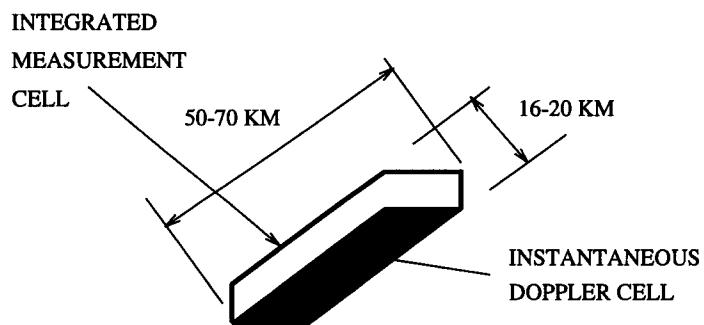


Figure 4.4: SASS integrated measurement cell.

the satellite ground track on the starboard side (see Fig. 4.3). Pulse compression is used to segment each footprint into resolution cells, and for each cell, six pulses are averaged together to obtain a single measurement. Specific information regarding the dimensions of the measurement cells and cell responses has not been released by the European Space Agency (ESA), but a general description has been obtained [12]. The cells are 100-km diameter circles. The cell response is a squared cosine with a half-power diameter of 50 km (see Fig. 4.5). Our ability to construct high resolution images from ERS-1 data is hampered by our lack of an accurate cell response description.

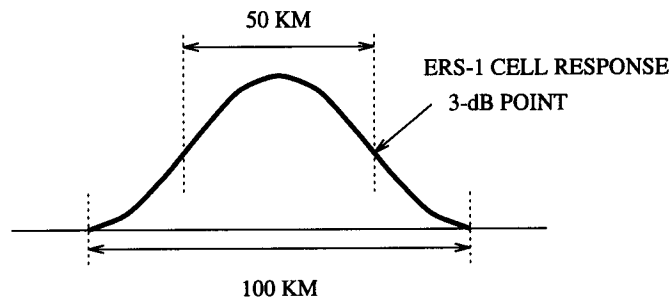


Figure 4.5: ERS-1 cell response.

4.3 Application of SIRF to SMMR

4.3.1 Considerations for Imaging

The SMMR data are available as antenna temperatures and as brightness temperatures. A radiometric calibration algorithm was used to generate the antenna temperatures which corrected for losses and reradiation in the microwave components and for non-linearities of the radiometer [13]. The antenna temperatures were then processed further using an antenna pattern correction algorithm that provided more accurate brightness temperature measurements by accounting for antenna sidelobe contributions and cross-polarization coupling [14]. It would have been desirable to use the brightness temperature measurements to generate the SMMR images; however, the antenna pattern correction algorithm made them

unsuitable for imaging. The correction algorithm averaged the antenna temperature measurements into a grid of evenly spaced square cells. This spatial averaging reduced the resolution of the data set, so the uncorrected antenna temperatures were selected for processing. The SMMR antenna temperatures differed from the true brightness temperatures of the observed scene for three main reasons: interference from the atmosphere, antenna sidelobe contributions, and cross-polarization coupling. These three problems will now be addressed.

Electromagnetic radiation propagating through the atmosphere is attenuated to some degree depending on the frequency of the radiation and the water content of the atmosphere. In order to avoid having cloud cover interfere with the measurements, frequencies for which attenuation through the atmosphere is minimal should be used. Fig. 4.6 shows that for frequencies greater than about 10 GHz, clouds can greatly affect the measurements [7]. For this reason, only the 6.6 GHz and 10.69 GHz data were used.

Energy entering the sidelobes of the antenna causes the measurements to not only depend on the region inside the footprint, but to a lesser degree on the region outside of the footprint. In order to deal with this problem, the measurement cells and cell responses should be calculated in a way that accounts for more than just the 3-dB footprint of the antenna. For SMMR data it was decided to extend the measurement cells to include the area within the 15-dB beamwidth of the antenna. This cutoff was chosen for simplicity because the antenna pattern within this beamwidth was almost symmetric, which simplified calculation of the measurement cells. Images created using the extended cell response estimate showed higher quality than images created using the 3-dB cell response estimates. The calculation of the cells will be described in a later section.

The third problem of using antenna temperatures, that of cross-polarization coupling, is due to the scanning of the reflector over the fixed feedhorn. As the reflector rotates above the feedhorn, the orientation of the feedhorn relative to the reflector changes by up to 25° from the plane of symmetry. The polarization of the measurements is most pure near the center of the swath, while at the swath edges, there is some mixing of polarized energy. Over the ocean, where the emitted energy is strongly polarized, this effect can change the antenna temperature by up to 10 K. In the land images, however, the effect is not clearly evident and has not

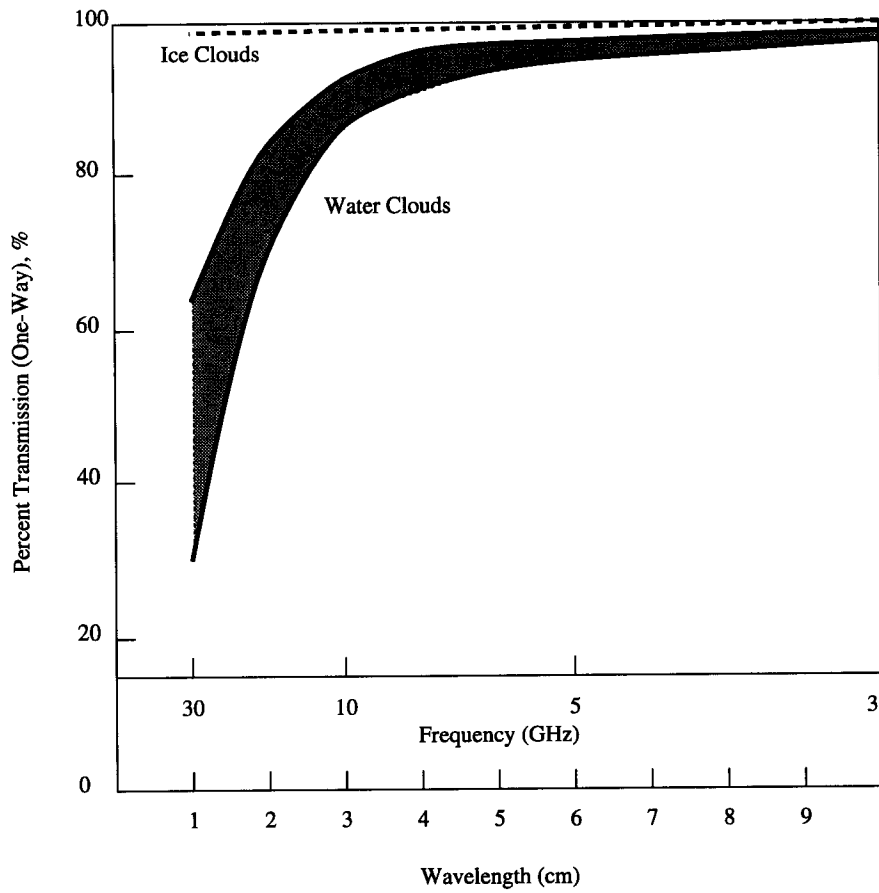


Figure 4.6: Effect of clouds on transmission from the earth surface into space.

been considered.

With the above considerations, the SIRF technique was successfully applied to SMMR data. This technique will now be presented.

4.3.2 The Modified SIRF Algorithm

The scatterometer image reconstruction with filtering (SIRF) algorithm was developed specifically for imaging from SASS data [3, 6]. SIRF is a multivariate algorithm in the sense that the two variable, \mathcal{A} and \mathcal{B} from Eq. 4.9, are estimated simultaneously. The multivariate estimation capability of SIRF is not necessary for image reconstruction of SMMR data, because the measurement incidence angle remains roughly constant at 48° . The SIRF algorithm had to be modified in order to be applied to the SMMR data. This modified version will be described here. A description of the multivariate SIRF can be found in [3, 6].

Suppose the brightness temperature distribution at the earth's surface is averaged into resolution elements on a rectilinear grid with a resolution element size $S_x \times S_y$. In the absence of noise the T_A measurement will be a weighted average of the T_B s of the resolution elements that lie within the region covered by the measurement cell. Eq. 4.7 can then be written as

$$T_{Ar} = \frac{1}{Q} \sum_{m=L_r}^{R_r} \sum_{n=B_r}^{T_r} T_B(m, n) h_r(m, n), \quad (4.10)$$

$$Q = \sum_{m=L_r}^{R_r} \sum_{n=B_r}^{T_r} h_r(m, n),$$

L_r , R_r , B_r , and T_r define a bounding rectangle for the r^{th} measurement cell, $h_r(m, n)$ is the weighting function for the $(m, n)^{th}$ resolution element and is simply the measurement cell response sampled on the same grid as the T_B distribution, and $T_B(m, n)$ is the T_B value for the $(m, n)^{th}$ resolution element. The resolution enhancement problem is then to determine the T_B value for each individual resolution element based on the T_A measurements.

This problem is handled for the noise free case by a class of iterative methods called algebraic reconstruction techniques (ART) [15]. SIRF is a variation of multiplicative ART (MART). In MART, a predicted value (forward projection)

of each measurement is calculated from a current estimate of the image and is compared to the measurement. A scale factor is then computed as the ratio of the measurement to the forward projection. An update term is then computed for each pixel in the measurement cell by multiplying by the scale factor. Between iterations, each pixel in the image is updated by averaging the update terms for the pixel. As the process progresses, the scale factors approach unity and all of the forward projections match the measurements. When noise is present in the measurements, however, the scale factors tend not to converge to unity and the process may even become unstable. SIRF is a form of MART that has been made less sensitive to noise in two ways. First, the scale factors calculated for each forward projection are damped by taking the square root. This brings all of the scale factors closer to unity, the damping effect being greater for values farther from unity. Second, the update terms are computed in a manner that limits the amount of change for a single update (see Equation 4.13). This tends to reduce the sensitivity of the update terms to noise. The univariate SIRF algorithm is outlined below.

Each pixel of the image estimate, p_j where j is the pixel number, is first set to some initial nonzero value (usually the average expected value of the image). Then for the k^{th} iteration, and for the i^{th} measurement in the data set, z_i , and its corresponding weighting function, h_{ij} , the forward projection, f_i^k , is calculated as

$$f_i^k = \frac{1}{q_i} \sum_{n=1}^N h_{in} p_n^k, \quad (4.11)$$

$$q_i = \sum_{n=1}^N h_{in},$$

where N is the number of pixels in the image. The scale factor, d_i^k , is then computed as

$$d_i^k = \left(\frac{z_i}{f_i^k} \right)^{\frac{1}{2}}. \quad (4.12)$$

The non-linear update term, u_{ij}^k is then computed according to

$$u_{ij}^k = \begin{cases} \left[\frac{1}{2q_i} \left(1 - \frac{1}{d_i^k} \right) + \frac{1}{p_j^k d_i^k} \right]^{-1} & d_i^k \geq 1 \\ \left[\frac{1}{2} q_i \left(1 - d_i^k \right) + p_j^k d_i^k \right] & d_i^k < 1 \end{cases} \quad (4.13)$$

After the entire data set has been processed, each pixel estimate, p_j^k , is updated by computing a weighted average of the update terms, i.e.,

$$p_j^{k+1} = \frac{1}{g_j} \sum_{i=1}^M h_{ij} u_{ij}^k, \quad (4.14)$$

$$g_j = \sum_{i=1}^M h_{ij},$$

where M is the number of measurement cells covering the pixel.

This set of equations is iterated over k until the scale factors approach unity and the image does not change between iterations. In addition, an edge-preserving 3×3 median filter is applied to the image between iterations which tends to improve the subjective quality of the image. For lower noise levels, this filter may be omitted, in which case the algorithm is referred to as SIR.

This technique relies on the cell response in calculating both the forward projections and the update terms. Because of this, the cell response estimate should be very accurate. The next section describes how the SMMR cell response estimates are calculated.

4.3.3 Improved SMMR Cell Response Estimate

Preliminary images were created with a cell response based on the 3 dB cutoff of the antenna pattern. The instantaneous footprint was assumed to be an ellipse with the dimensions given in [16] and response of 1 inside the footprint and 0 outside. Each measurement cell was then estimated by stepping this footprint along the path of the scan and adding the number of footprints within the cell that covered each pixel in the cell. The cell response was then normalized by dividing by the number of instantaneous footprints used in the estimate. The quality of the images generated in this way was unsatisfactory. In an effort to improve the image quality, a better measurement cell response estimate was developed.

The basic idea of the improved cell response is the same as that described in the previous paragraph. The improvement is that the antenna pattern was used to estimate the instantaneous footprint response to the 15 dB cutoff for each step along the scan. Calculating the footprint response is done as follows. Suppose

the antenna boresight intersects the surface at (x_0, y_0) . The footprint response, $f_0(x, y)$ is given (approximately) by

$$f_0(x, y) = 10^{-0.06\theta^2(x, y)}, \quad (4.15)$$

where $\theta(x, y)$ is the angle in degrees between the boresight line and a line from the antenna to the point (x, y) . This angle is determined by

$$\theta(x, y) = \arccos \left(\frac{2d_1^2 - 2d_1d_2(x, y) \cos[\psi(x, y)]}{2d_1[d_1^2 + d_2^2(x, y) - 2d_1d_2(x, y) \cos(\psi(x, y))]\frac{1}{2}} \right), \quad (4.16)$$

where d_1 is the length of a line segment D_1 from the spacecraft to the point (x_0, y_0) , $d_2(x, y)$ is the length of a line segment D_2 from the point (x, y) to the point (x_0, y_0) , and $\psi(x, y)$ is the angle between D_1 and D_2 . All of these quantities must be determined from information contained in the SMMR data records. Figure 4.7 shows how a typical cell response pattern would look using both methods for estimating the instantaneous footprints. The units on the spatial axes are arbitrary spatial units.

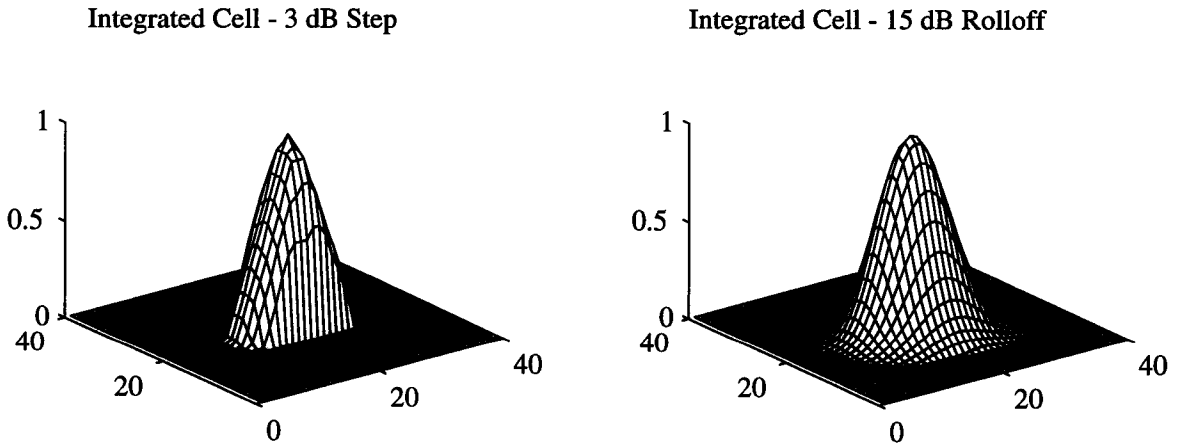


Figure 4.7: Integrated cell response using the 3 dB cutoff (left) and 15 dB roll-off (right).

While the improved cell response estimate resulted in smoother, apparently less noisy images, the computational time and storage requirements for creating an image increased dramatically. This problem is addressed in the next section.

4.3.4 Computational Considerations

The computer requirements for storage space needed to generate a single SMMR image with the improved cell response estimate are very large. For the Greenland images in Chapter 6, data from four days was combined for an image that covered an 1850-km \times 1850-km area at a scale of 6.25 km per pixel. This is approximately 19,000 individual measurements per image for the 6.6 GHz case. A cell response pattern typically covered about 1000 pixels. Since SIRF is an iterative method that requires access to each cell response once per iteration, it is most efficient to calculate the cell responses only once and store them in a file. Each pixel in a cell response requires a location and a weight. Using 4-byte integers for the location and 4-byte reals for the weights means that each measurement requires about 8,000 bytes of storage space. For 19,000 measurements, this adds up to about 152 megabytes per image. For a series of images, this storage requirement is overwhelming.

Two steps were taken to reduce the necessary storage. First, the weights were integer quantized to 2-byte integers. In doing this, accuracy is maintained to about -45 dB, which is sufficient since the cell response was only estimated above the 15-dB cutoff as described in section 4.3.3. The second step achieved a great reduction by recognizing that all of the pixels are located next to each other in rows that are also next to each other. Rather than store a location for each pixel, a reference location was stored, which was the location of the first pixel in the first row of pixels. Each row of pixels was then defined by its first pixel, which is determined by an offset number of columns from the first pixel of the previous row, and by the total number of pixels in the row. Thus each row required the storage of only 4 bytes. There are typically about 43 rows in a single cell, so the storage requirements for pixel location information was reduced from about 4,000 bytes to about 176 bytes per cell. These steps reduced the storage requirement by about 49 percent.

The time required to calculate the cell responses was also large due to the enormous number of mathematical operations. Calculating the weight for each pixel in a measurement cell required on the order of 1500 mathematical operations. The total number of operations required for an image was cut in half by calculating

the weight for every other pixel in a checkerboard fashion and estimating the weights for the other pixels by averaging the surrounding weights. A comparison of an image generated in this manner to an image for which all pixel weight values were calculated showed that the brightness temperature estimates for the two images differed by less than 0.01 K for almost all pixels. The time required to calculate all of the cell responses was reduced from about 34 to 17 CPU hours on a VAX series 4000 model 60 workstation. With about 7 CPU hours required for the SIRF program, about one four-day image of Greenland could be generated per day per computer workstation.

CHAPTER 5

RESULTS

This chapter is divided into two sections: simulation results and real measurement results. The simulation section allows for a direct comparison of two-dimensional images from the three instruments, SMMR, SASS, and ERS-1, and enables a performance review of each instrument via a comparison of the image reconstructed from a set of synthetic measurements with the “true” image used to calculate the measurements. The simulations are for both noise-free and noisy measurements. For the noise-free case, the differences in resolution for the three instruments depend only on the size, shape, and distribution of the measurement cells and cell responses. The noisy case is presented to aid in interpreting the images from real data. By simulating noisy measurements, we can get a feel for how much degradation of the real data images is due to noise. The added noise level is approximately the same as the real data.

5.1 Simulation Results

It is difficult to determine the resolution of images from real data since the underlying surface response from which the real measurements were made is not known. Thus, Eq. 2.8 cannot be used directly to determine resolution. For this reason, a test image is used to generate a set of simulated measurements, and the resolution is determined by comparing the test image with the image created from the measurements.

As was shown in the examples of Chapter 3, if the test image has a wavenumber that increases linearly with distance, then the wavenumber spectrum of the image can be determined directly from the image. With this in mind, a test image was created with a surface response given by

$$s(x, y) = a + b \times \cos\left(\frac{2\pi d^2}{c}\right), \quad (5.1)$$

where a and b are chosen to make the average value and dynamic range of the simulated surface response appropriate for the different instruments, c is used

to scale the rate of increase in wavenumber and was chosen so that the sizes of the image features ranged from below to above the limit of resolvability for each instrument, and $d = \sqrt{x^2 + y^2}$ is the distance from the origin. The image scale is 6.25 km per pixel, and the image region corresponds to an 1850 km \times 1850 km square.

To obtain the simulation measurements, actual measurements covering an 1850-km square region of the Earth's surface were used. The measurement cell locations, dimensions, and cell responses were taken from the data set and the simulation measurement values computed from the test image. The images were created by applying the SIRF technique to the synthetic measurements. For the noisy measurements, a random noise term was added to each measurement based on the noise estimates contained in the data set.

5.1.1 SMMR

Two separate test images were used for the SMMR simulation. One was for 6.6 GHz measurements, and the other was for 10.69 GHz measurements. Since the footprint size is different at the two frequencies, the rates of increase in wavenumber for the test images were chosen so that the extent of the measurement response at each frequency would show up in the simulation. The 6.6 GHz test image was generated from Eq. 5.1 using $a = 200$, $b = 10$ and $c = 3600$. The data set used to generate the synthetic measurements was taken from an 1850-km square region centered at 52° West longitude and 68° North latitude. The data was collected over a four-day time span, which amounted to approximately 21,000 measurements.

The actual layout of the cells (3-dB contour) for a single scan are shown in Fig. 5.1 (left) and for several scans in Fig. 5.1 (right).

Note that the amount of overlap between consecutive measurements varies across the swath due to the sinusoidal velocity of the scanning reflector. Note also that the cells are ellipses with low eccentricity, and are oriented in many different directions. As a result the measurement response due to the combining of many different measurement cells is essentially circularly symmetric about the

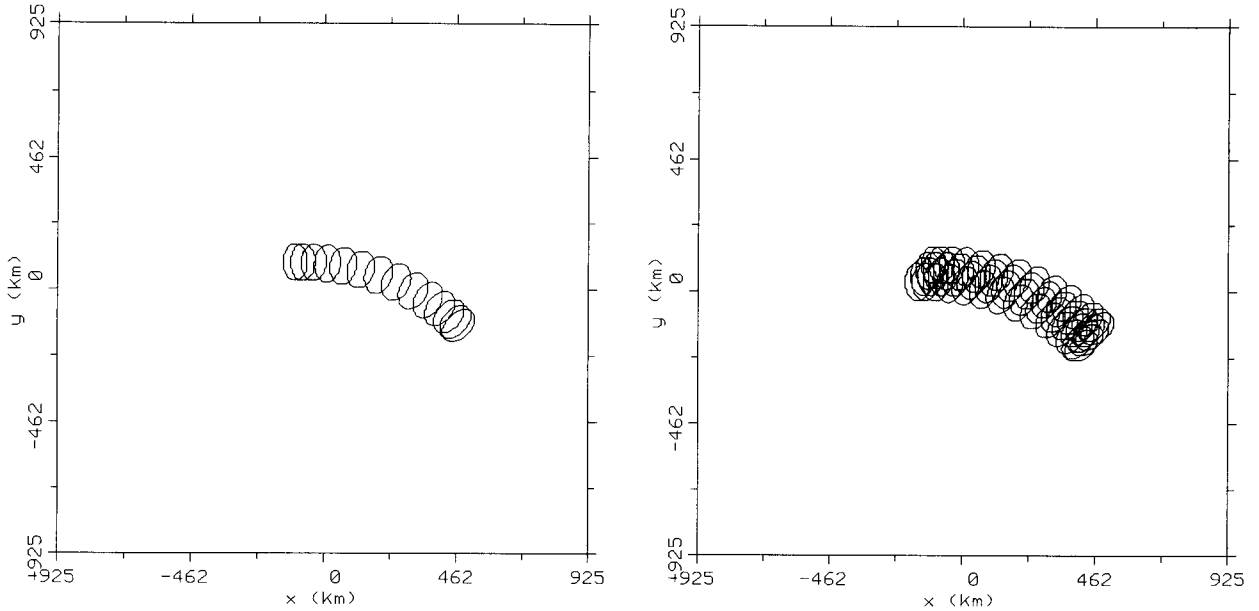


Figure 5.1: Typical cell layout (3 dB contour) for SMMR 6.6 GHz measurements for a single scan (left) and for several scans (right).

origin of the wavenumber plane. This symmetry is evident in the simulation image. The test image and resulting SIRF image are shown in Fig. 5.2. The lower frequency variations are resolved, but the high frequency variations are filtered out. Note that the roll-off of the SIRF image appears to be circularly symmetric about the center point of the image.

To determine the error in the image, we examine a vertical cross section through the center of the image (Fig. 5.3 top). The wavenumber spectrum is estimated from the roll-off of the envelope of the SIRF image, except near the edges where the SIRF image drops down below 200. This is due to edge effects and is ignored. The spectrum is estimated directly from the image by determining the envelope of the image, removing the mean value, and normalizing by the value of b used in Eq. 5.1. This normalized envelope is simply the effective low pass measurement response inherent in the measurement and imaging process. To find the error, this low pass filter is subtracted from 1 and plotted against wavenumber (Fig. 5.3 bottom). The simulation shows that for $E = 0.6$, the resolution of the SIRF image from 6.6 GHz SMMR data is about $\Omega = 0.27$. This corresponds to

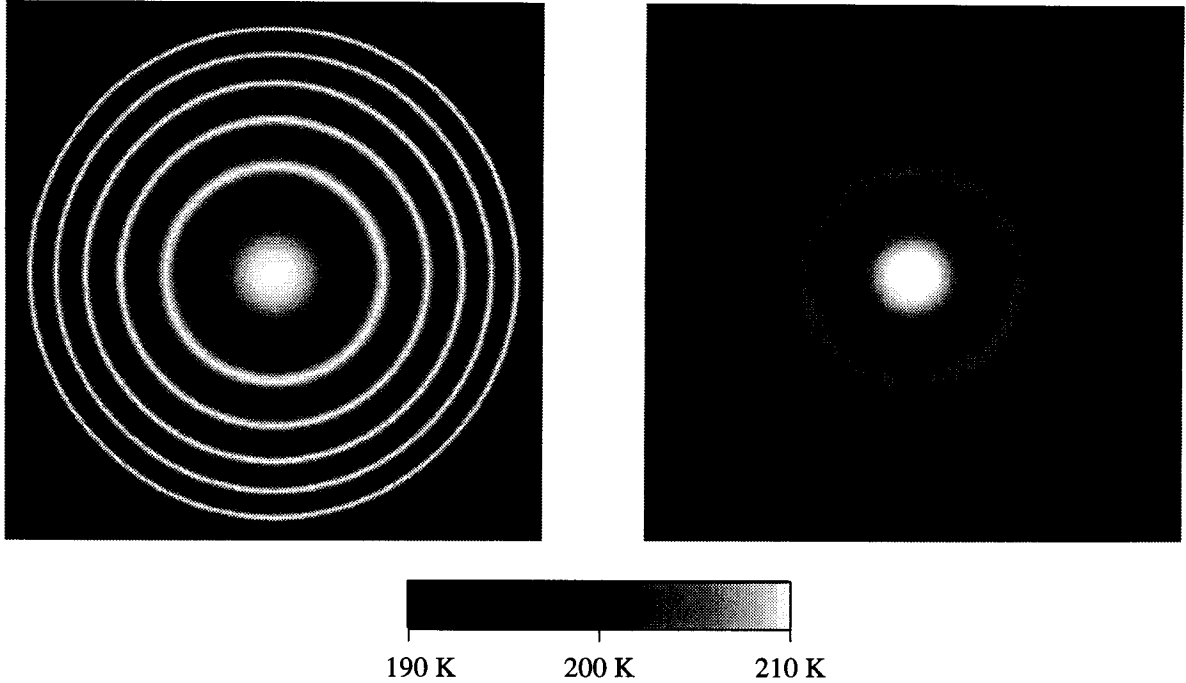


Figure 5.2: Test image (l) and SIRF image (r) for simulated 6.6 GHz noise-free SMMR data

a spatial resolution of about 145.4 km, which is about 20% larger than the 3-dB diameter of the measurement cells.

Next we examine the results of applying a compensating filter to the SIRF image. The compensating filter is the inverse of the effective low pass measurement response discussed in the previous paragraph. Since the SIRF image appears to be almost circularly symmetric about the center point, the effective low pass filter is assumed also to be circularly symmetric. Thus, the two-dimensional filter is designed by rotating the one-dimensional filter estimate about the origin of the wavenumber plane. As was discussed in Chapter 3, when an inverse filter is applied, a low pass filter must also be used to avoid excessive amplification of noise in the image. Two compensation filters are presented here that use different low pass filters. The first uses an 11th order Chebyshev filter with cutoff at $k = \pi/10$ and will be called Filter 1. The second uses a 7th order Butterworth filter with cutoff at $k = \pi/11.11$ and will be called Filter 2. The design specifications of these

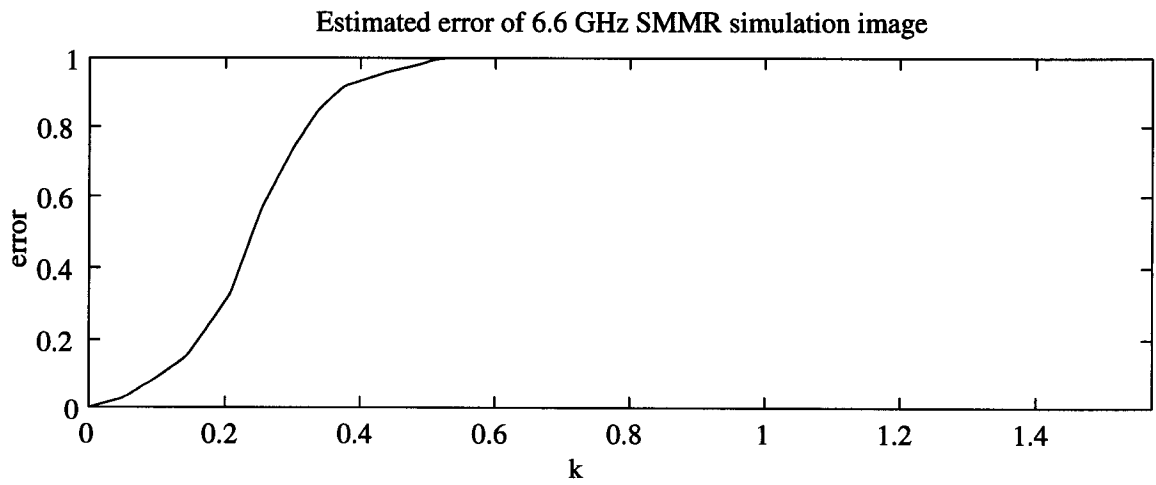
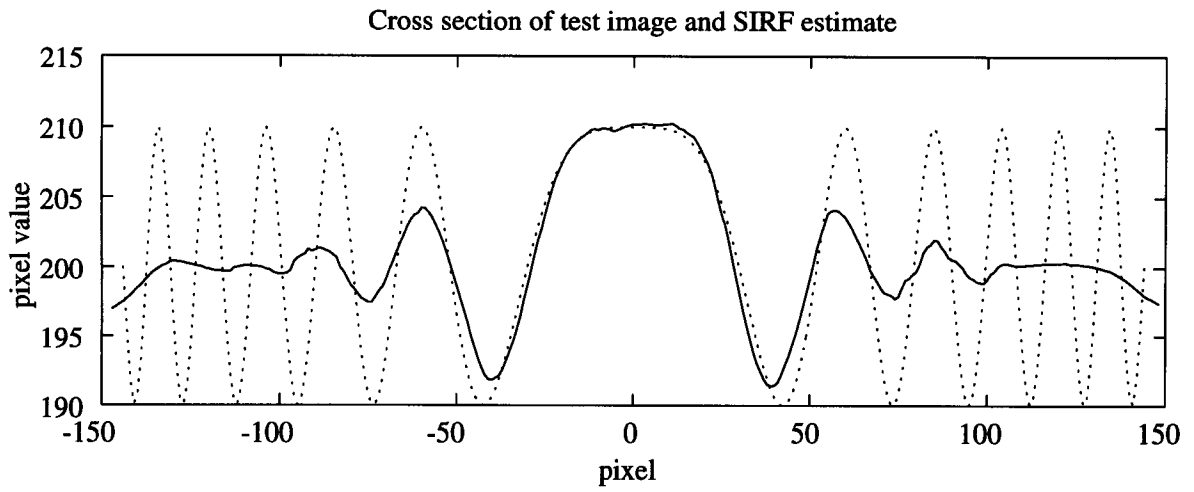


Figure 5.3: Cross section and estimated error of SIRF image from 6.6 GHz SMMR data

filters were chosen subjectively by looking at the estimated roll-off of the SIRF image and then observing the results of compensation filtering using filters of various orders and cutoff frequencies. While the increase in resolution will not be as great for Filter 2 as for Filter 1 because of the lower cutoff, the introduction of artifacts will be less since the filter sidelobes are smaller. The composite filter response of these two compensating filters are shown in Fig. 5.4. The filtered images are shown in Fig. 5.5.

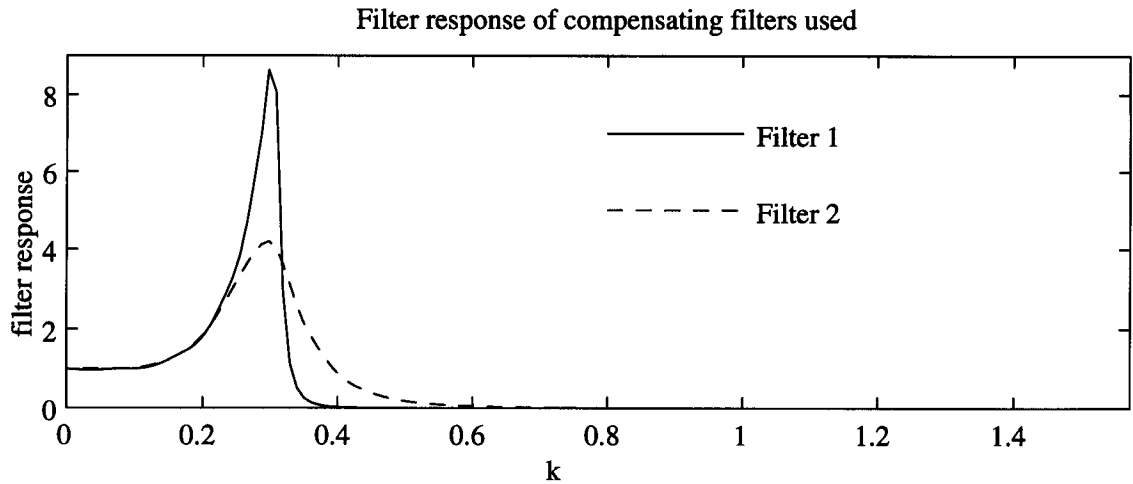


Figure 5.4: Filter response of compensating filters.

From the cross sections of the filtered images compared to the SIRF and test images (Fig. 5.6 top) we see that some of the features in the image have been enhanced significantly. However, as we saw in Chapter 3, the compensation filtering has also introduced some artifacts into the images. The Filter 1 image has a dip at the center and shows features near the edges that do not correspond to the true image. The Filter 2 image does not appear to be as corrupted by the artifacts as the Filter 1 image. From the estimated error (Fig. 5.6 bottom), the resolution of the filtered images are $\Omega = 0.32$ for the Filter 1 image and $\Omega = 0.3$ for the Filter 2 image. These resolutions correspond to spatial resolutions of 122.7 km and 130.9 km, respectively. This is about the same distance as the 3-dB diameter

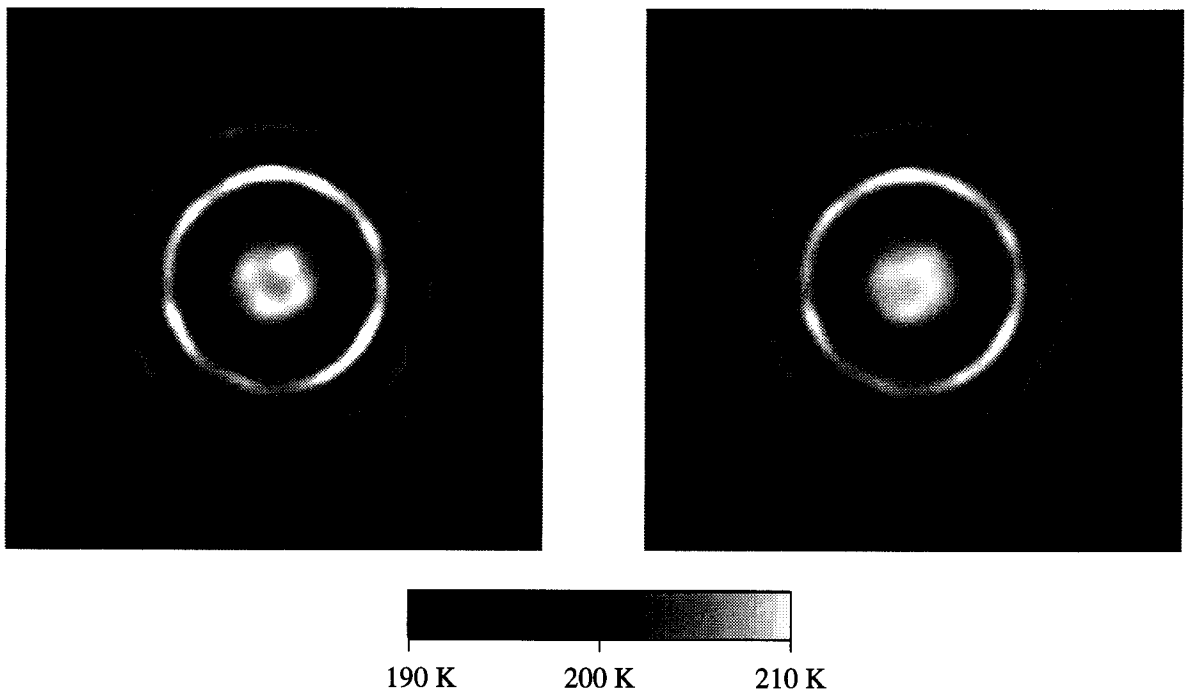


Figure 5.5: SIRF images after compensation filtering by Filter 1 (l) and Filter 2 (r).

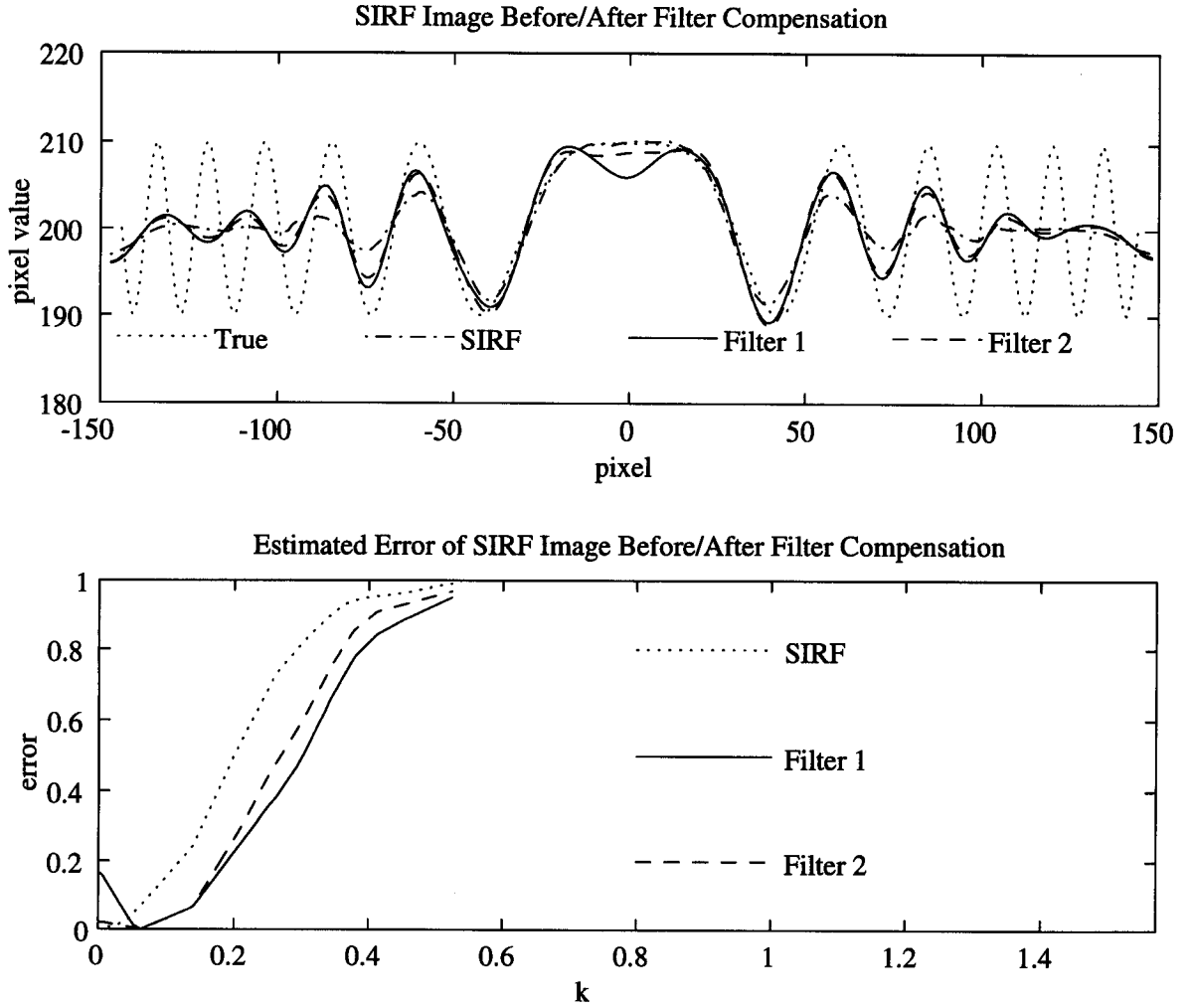


Figure 5.6: Cross section and estimated error of compensation filtered images.

of the measurement cells.

Next we consider the effects of noise in the measurements. The simulated noisy measurement set was obtained by adding noise to the simulated measurement set according to the equation

$$z_r = T_r + \Delta T \mathbf{x}_r, \quad (5.2)$$

where z_r is the r^{th} noisy measurement, T_r is the simulated noise-free value of the r^{th} measurement, ΔT is the estimated standard deviation of the noise as given in the data set ($\Delta T \approx 0.65K$), and \mathbf{x} is a normal Gaussian random variable. The SIRF image from the noisy measurements is shown in Fig. 5.7. A cross section of

the image and the estimated error are shown in Fig. 5.8. Comparing Fig. 5.7 with Fig. 5.2 and Fig. 5.8 with Fig. 5.3, it is evident that there is only slight degradation of the image and virtually no reduction in resolution.

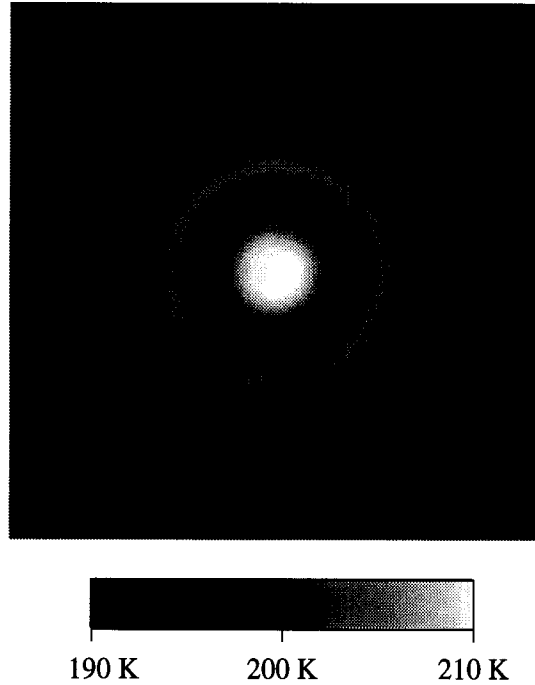


Figure 5.7: SIRF image from simulated noisy 6.6 GHz SMMR measurements.

When a compensating filter is applied to the SIRF image from noisy measurements, the resolution is improved, but more image artifacts are evident (see Fig. 5.9). Since Filter 1 caused more degradation of the image than Filter 2 in the noise-free case, only Filter 2 was used. A vertical cross section and the estimated error of the enhanced image are shown in Fig. 5.10. The resolution of the enhanced image is about $\Omega = 0.3$, which is the same as for the noise-free case.

Next we look at the simulation for 10.69 GHz SMMR measurements. For the 10.69 GHz SMMR measurements, a test image with a steeper increase in wavenumber was needed to best estimate the response of the SIRF image. The test image was created from Eq. 5.1 using $a = 200$ and $b = 10$ as before, and with $c = 2160$. The actual layout of the measurements is shown in Fig. 5.11. These measurements were collected over the same region as the 6.6 GHz measurements. The total number of measurements is about 40,000. The density of the 10.69 GHz

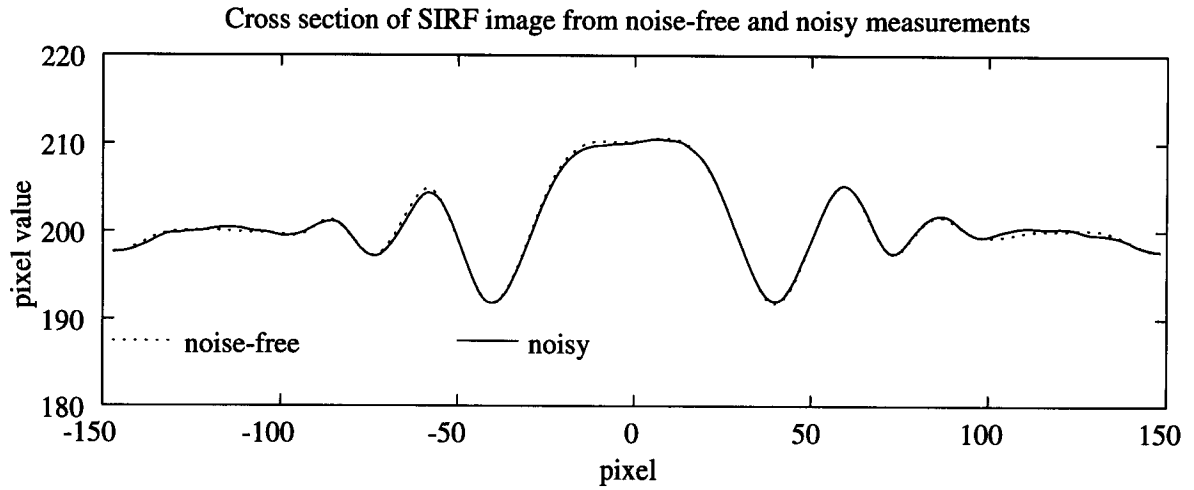


Figure 5.8: Cross section of SIRF image from simulated noisy 6.6 GHz SMMR data

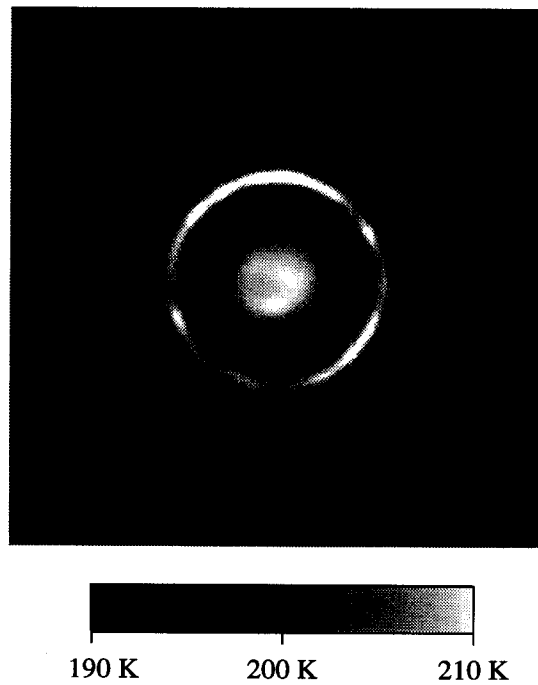


Figure 5.9: Compensation filtered SIRF image from simulated noisy 6.6 GHz SMMR measurements.

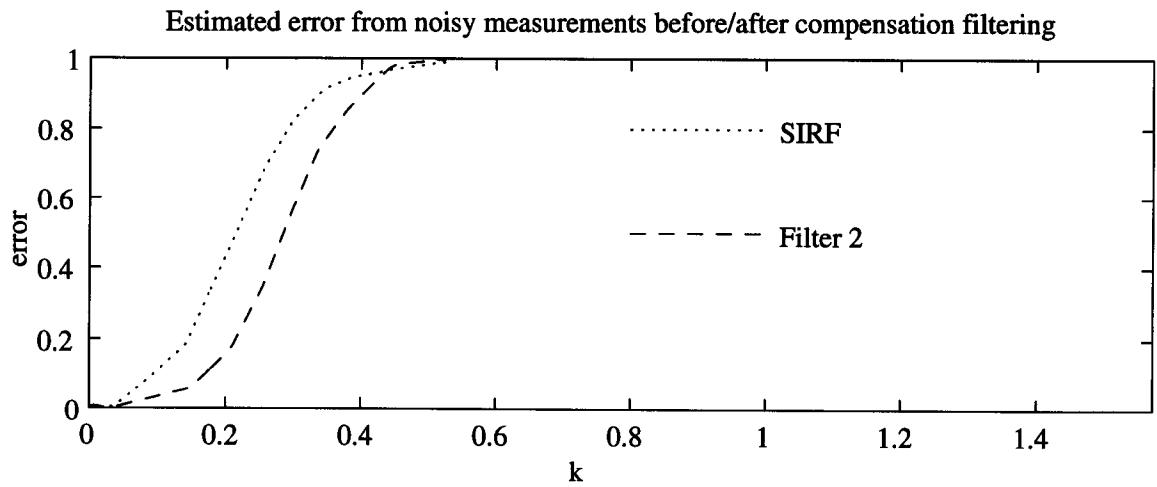
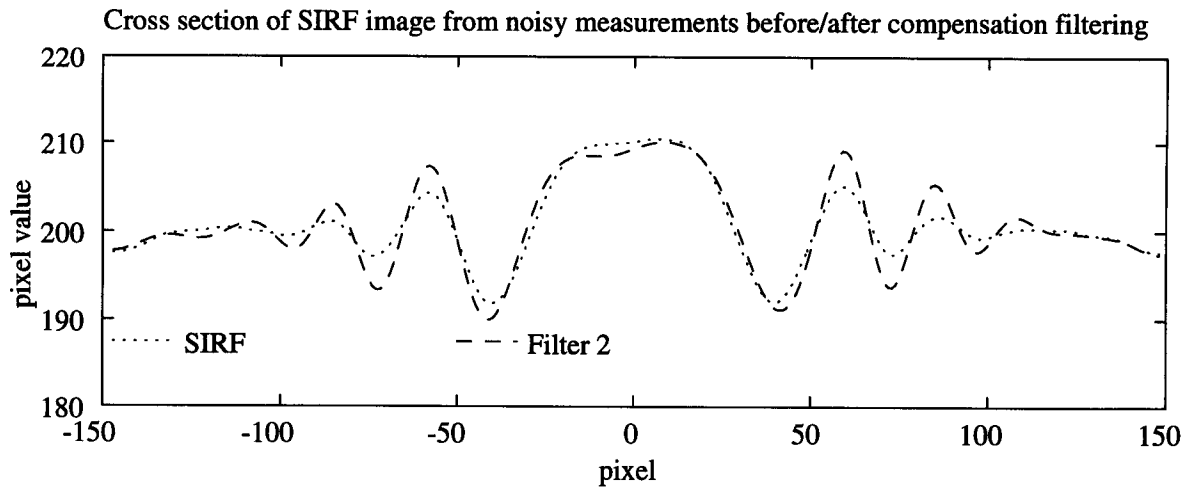


Figure 5.10: Cross section and estimated error of SIRF image from simulated noisy 6.6 GHz SMMR data after compensation filtering.

measurements is higher than the 6.6 GHz measurements because the measurement cell size is smaller, hence twice as many measurements were taken.

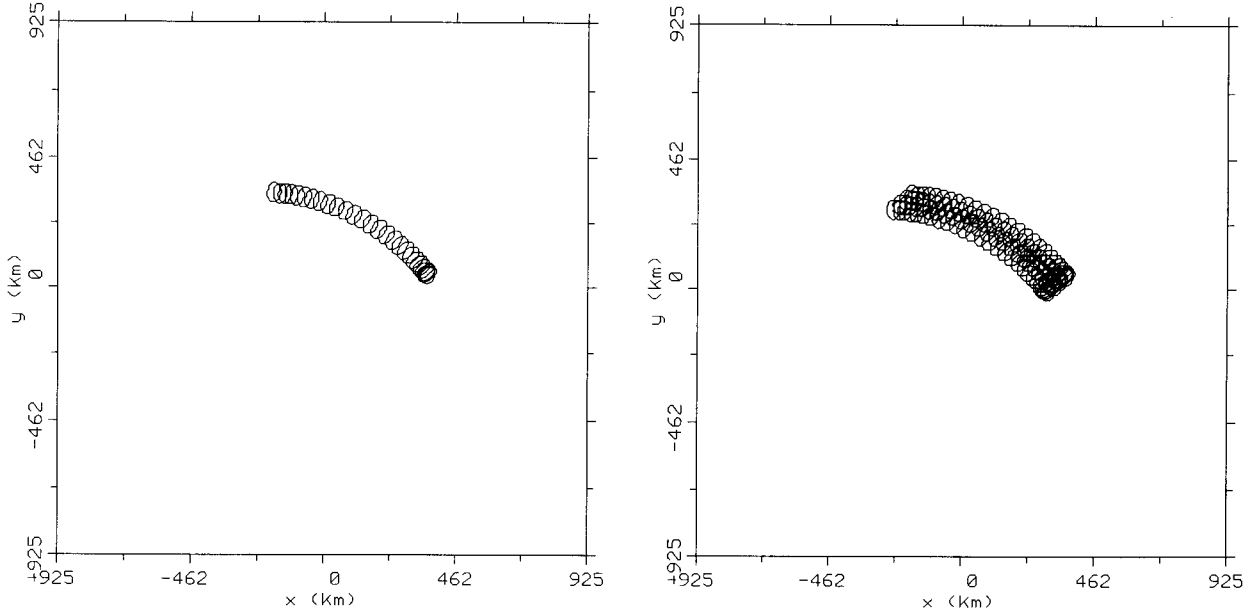


Figure 5.11: Typical cell layout (3 dB contour) for SMMR 10.69 GHz measurements for a single scan (left) and for several scans (right).

The test image and the SIRF estimate are shown in Fig. 5.12. The cross section of the images and an estimate of the error are shown in Fig. 5.13. The resolution of the SIRF image in this case is about $\Omega = 0.4$ for $E = 0.6$. This corresponds to a spatial resolution of 93.5 km, which is about 20% larger than the 3-dB diameter of the measurement cells. The results for the 10.69 GHz measurements are all very similar to the results for the 6.6 GHz measurements, so the noise-free SIRF result will simply be presented without considering compensation filtering and noisy measurements.

5.1.2 SASS

Recall that the SIRF algorithm for scatterometers estimates two parameters that characterize the linear model for the dependence of σ° (dB) on incidence angle: the normalized intercept, A , and the slope, B . Hence, simulated A and B images are needed. The A test image was generated from Eq. 5.1 with $a = -10$,

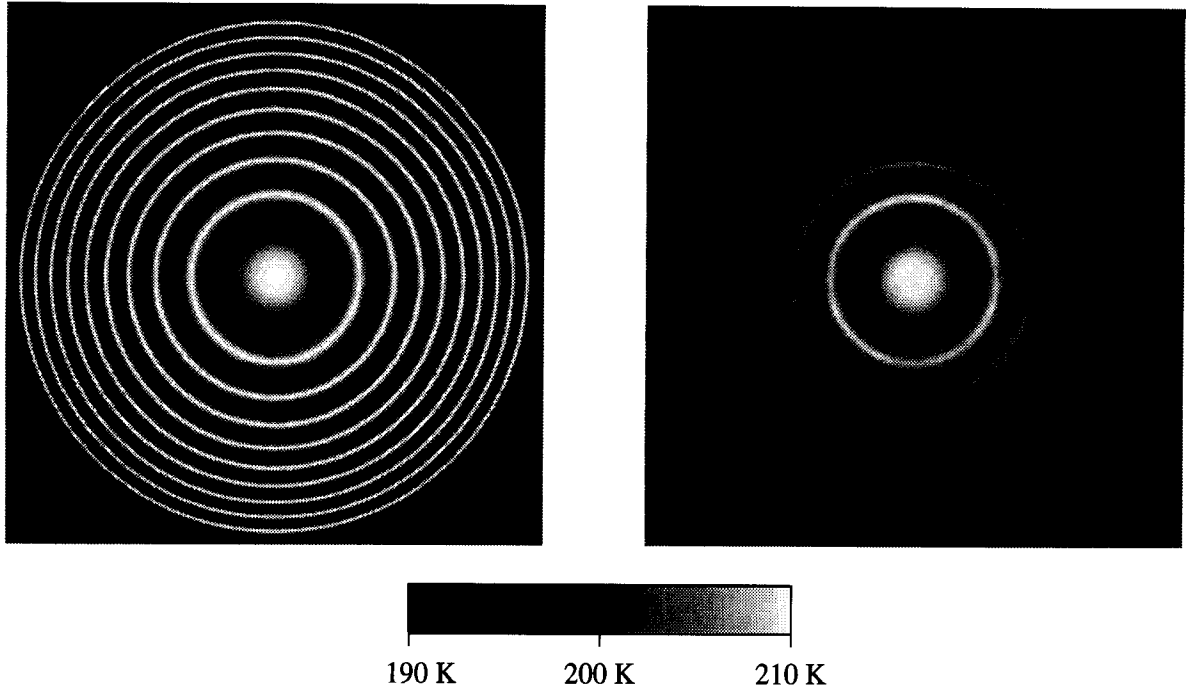


Figure 5.12: Test image (l) and SIRF image (r) for 10.69 GHz SMMR data

$b = 5$ and $c = 1080$. This image has a very rapid increase in wavenumber to test the high resolution of the SASS data. For this simulation, the B image was set to zero. The data set used to generate the synthetic measurements was collected over a three month period and contains measurements that fall within an 1850-km square region centered at 61.25° West longitude and 6.55° South latitude, covering a portion of the Amazon rain forest. The image is made from about 225,000 measurements.

The actual layout of the measurement cells for one measurement cycle of a single beam is shown in Fig. 5.14 (left) and the layout for several measurement cycles of two beams is shown in Fig. 5.14 (right). Note that the cells increase in size across the swath. The increase is due to the increase in slant range at the far swath. Note also that the measurement cells are oriented with the long dimension aligned along the look direction of the antenna. From Fig. 4.3 on page 39, the cells will be oriented with the long dimension along one of two lines 45° or 135° from the subsatellite track. The orbit inclination angle is about 110° for ascending passes and 70° for descending passes (see Fig. 5.15), so when measurements from

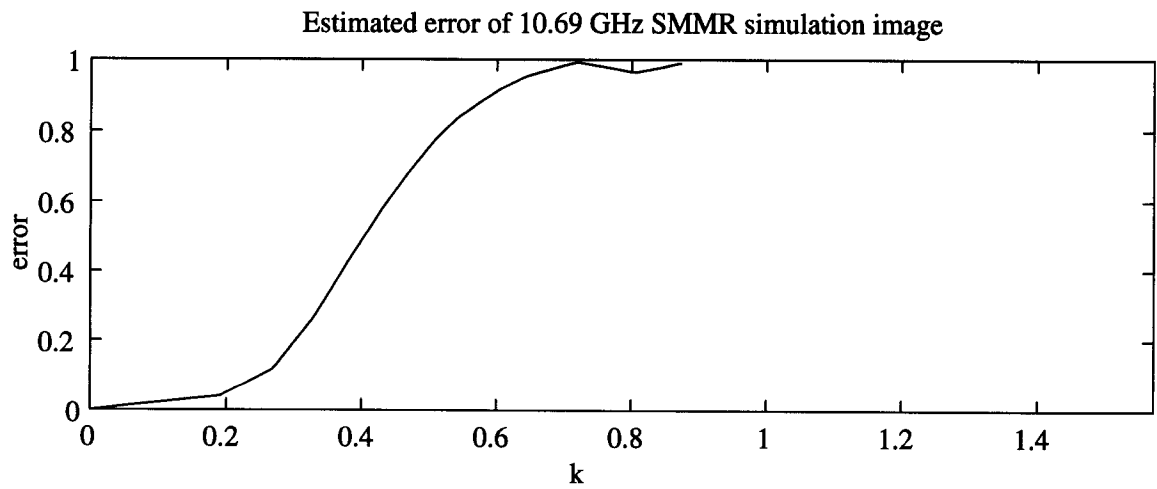
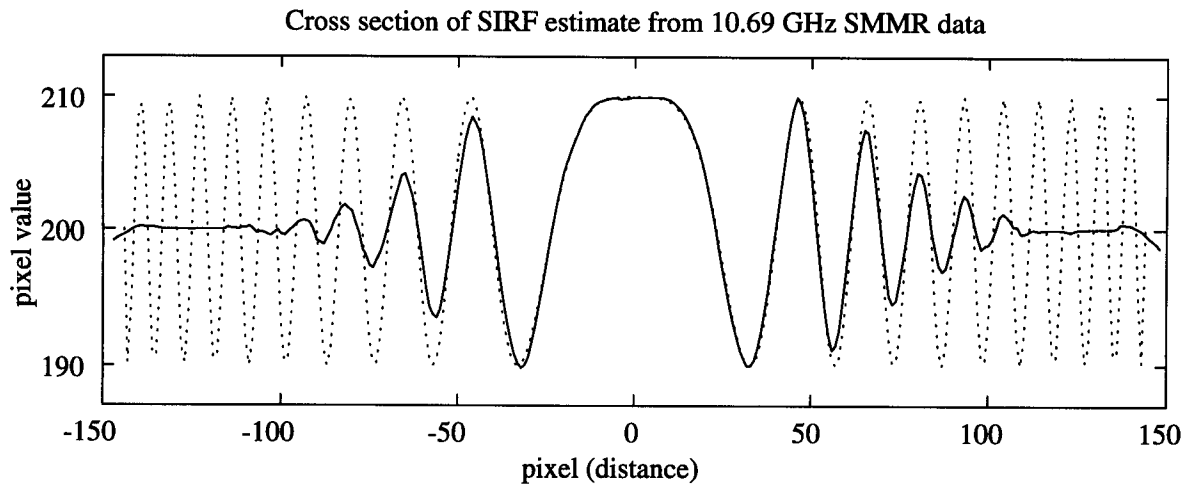


Figure 5.13: Cross section and estimated error of SIRF image from 10.69 GHz SMMR data

ascending and descending passes are combined into one data set, the measurement cells are oriented with the long dimension aligned in one of four directions.

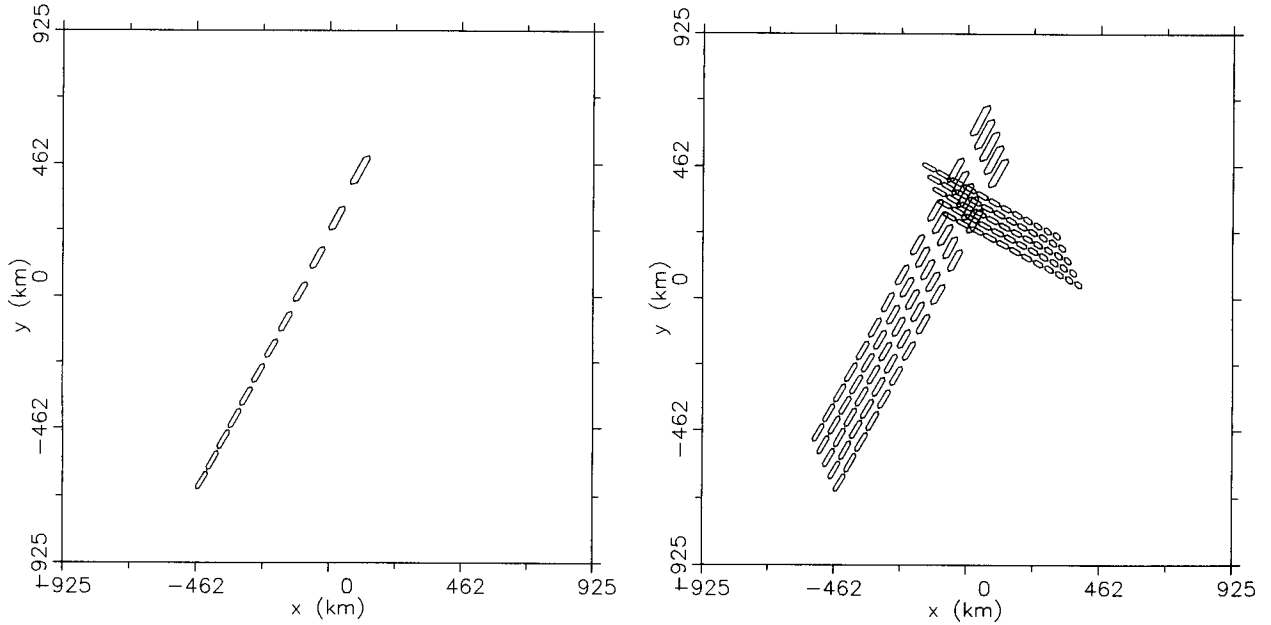


Figure 5.14: Typical cell layout (3 dB contour) for SASS measurements for a single beam (left) and for several beams (right).

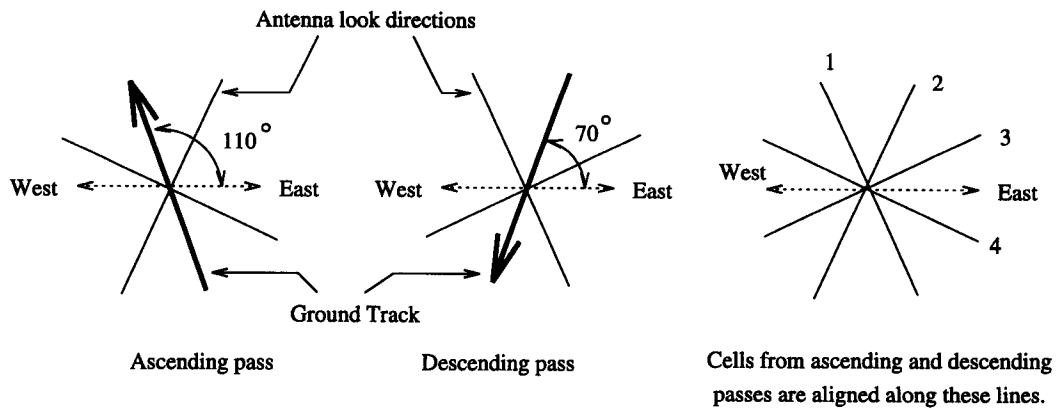


Figure 5.15: Orientation of SASS cells used in simulation.

Because the cells are aligned in this manner, the effective low pass filter inherent in the measurements and imaging process is not circularly symmetric, hence the resolution of the SIRF image is also not circularly symmetric. To illustrate, consider only the measurement cells that are aligned in one direction. For these measurements, the effective filter response is long and narrow (see Fig. 5.16). For a set of measurements whose cells are aligned in several different directions, the effective filter response is a combination of many long and narrow shapes (see Fig. 5.17).

The simulated A image and resulting SIRF image are shown in Fig. 5.18. Note that the criss-cross shaped filter response discussed above shows up in the SIRF image (see Fig. 5.19). Thus, the resolution of the SIRF image from SASS data is not circularly symmetric.

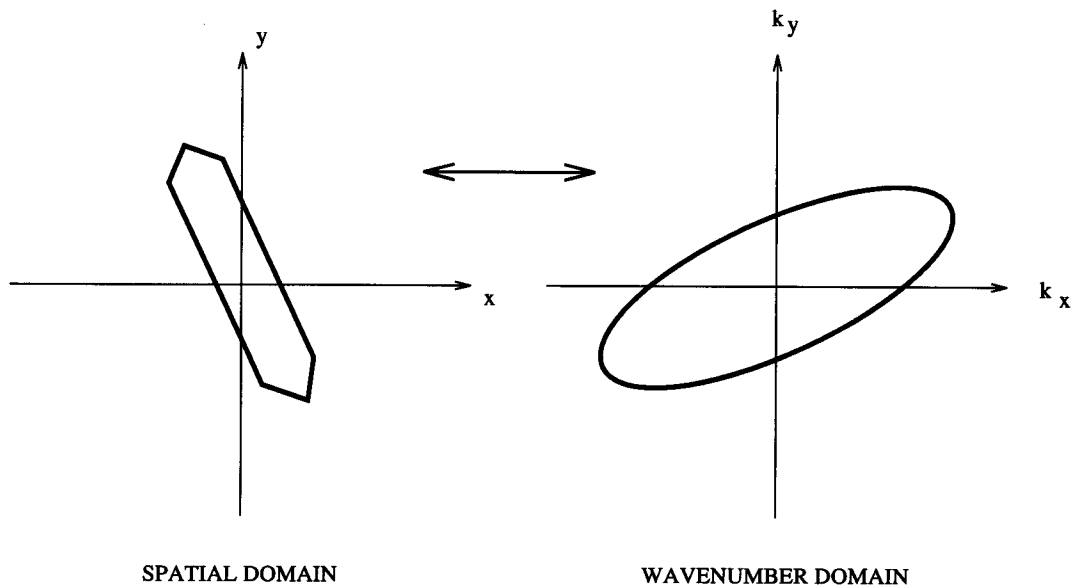


Figure 5.16: Effective cell response and FT for cells aligned in one direction.

Fig. 5.20 shows a cross section and estimated error for the SIRF image. The cross section runs through the center of the image along a line from the midpoint of the top side of the image to the midpoint at the bottom side. Using this cross section for the error gives a lower bound on the resolution since the error along this line is the greatest. The resolution in this case is about $\Omega = 1$

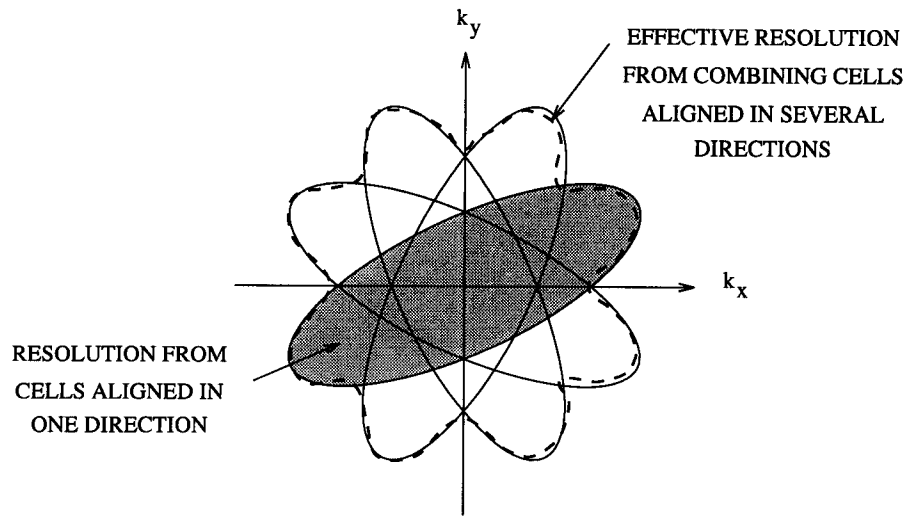


Figure 5.17: Effective resolution of the SASS image

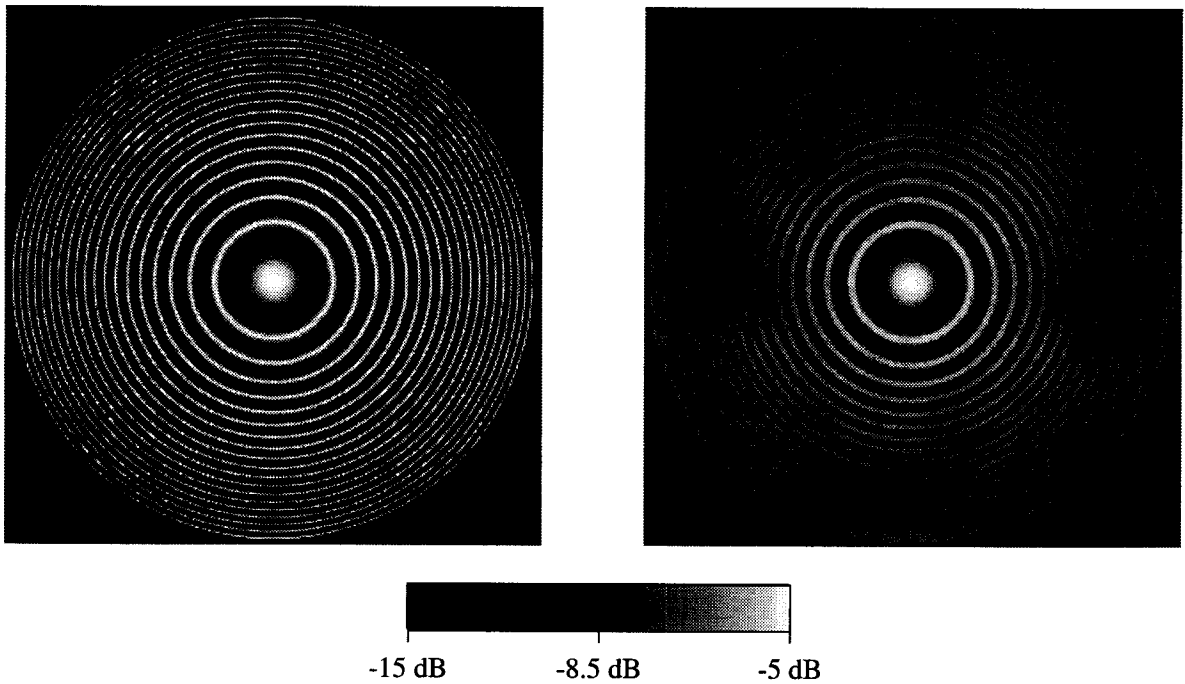


Figure 5.18: Test image (l) and SIRF image (r) for SASS data

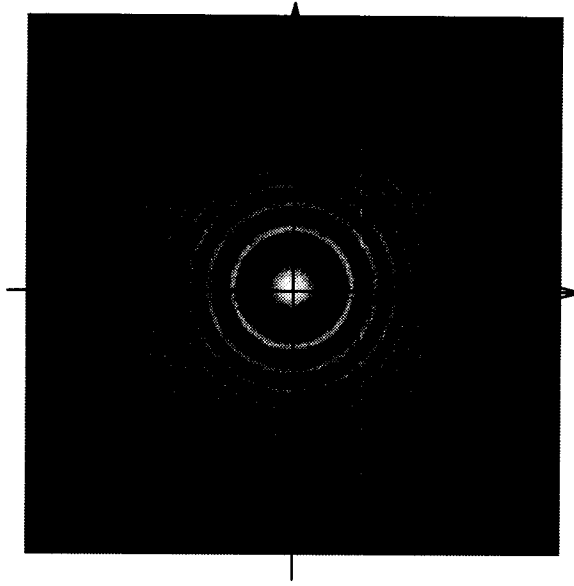


Figure 5.19: Resolution of the SIRF image from simulated SASS data

for $E = 0.6$. This is a spatial resolution of 39.3 km. Consider that this is from measurement cells that range in size from 16×50 km to 20×70 km.

Since the effective resolution of the SIRF image depends on the angle of cross section, finding an appropriate compensating filter for the SASS image is rather difficult. Furthermore, the SASS image has the highest resolution of all the instruments considered here. As a result no compensating filter was applied.

Noise had virtually no effect on the SASS images, so the results are presented without accompanying figures. Noise was added to the measurement set according to (see [3])

$$z_r = (1 + K_p \mathbf{x}_r) \sigma_r^\circ, \quad (5.3)$$

where z_r is a noisy measurement, K_p is an estimate of the noise standard deviation for the r^{th} measurement and is taken from the data set, \mathbf{x}_r is a zero mean Gaussian random variable of variance 1, and σ_r° is the simulated value of the r^{th} measurement. The simulation showed that the SIRF algorithm with SASS is very insensitive to noise. A cross section of the SIRF image for noise-free and noisy measurements showed that the noise level was so low that the noise-free and noise added images

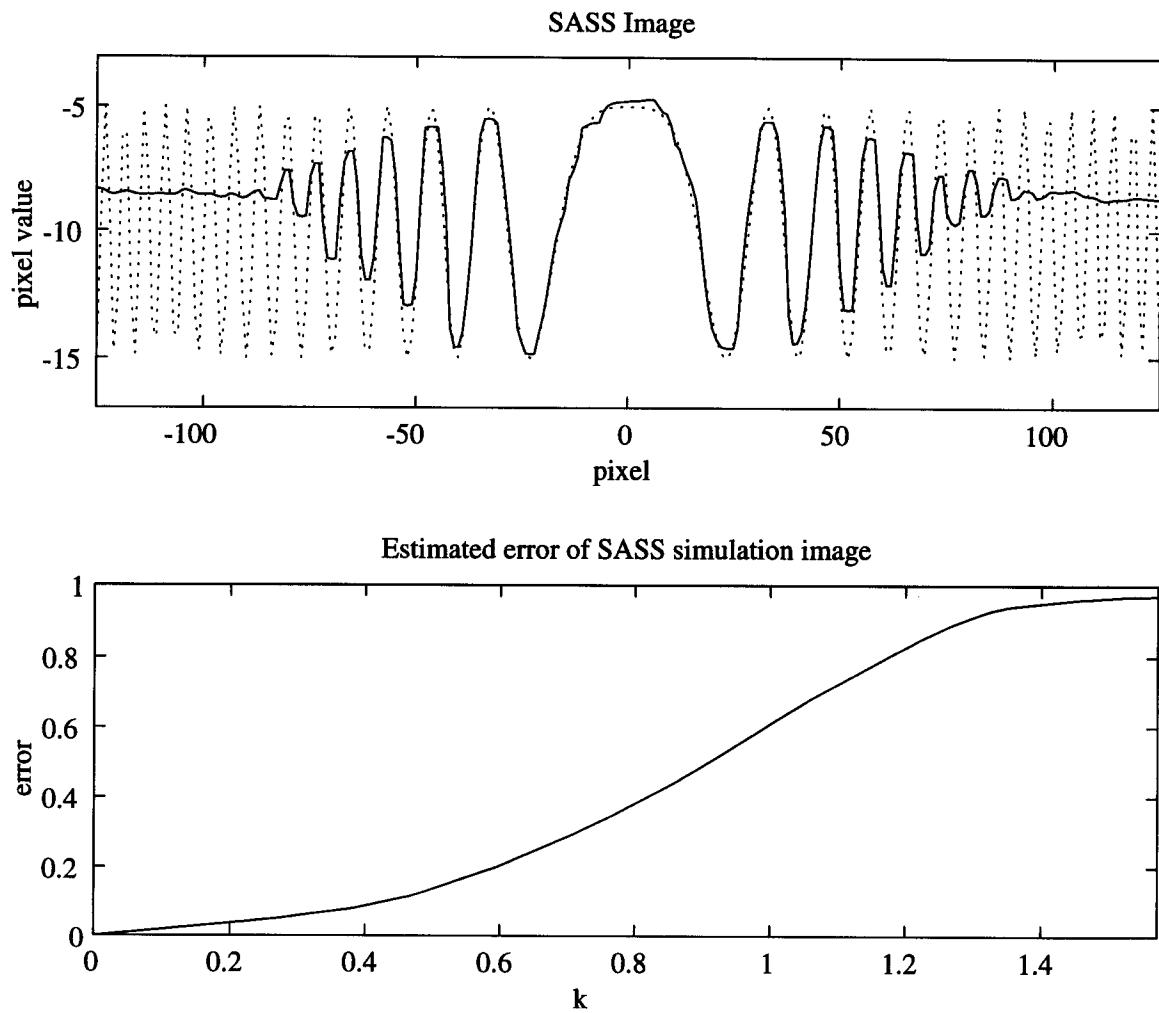


Figure 5.20: Cross section and estimated error of SIRF image from SASS data

were virtually indistinguishable. For this reason, the cross section is not shown and the noise will not be considered further.

5.1.3 ERS-1 Scatterometer

The simulated A image for the ERS-1 scatterometer measurements was generated from Eq. 5.1 with $a = -10$, $b = 5$ and $c = 2160$. Note that the rate of increase in wavenumber is lower for the ERS-1 test image than for the SASS test image since ERS-1 is a lower resolution instrument. As was done for the SASS simulation, the B image was set to zero. The layout of the ERS-1 measurement cells (3 dB contour) for one cell and for a single measurement cycle are shown in Fig. 5.21 (left) and for several measurement cycles in Fig. 5.21 (right). There are 19 measurement cells per antenna and corresponding cells from the different antennas are assumed to have co-located cell centers.

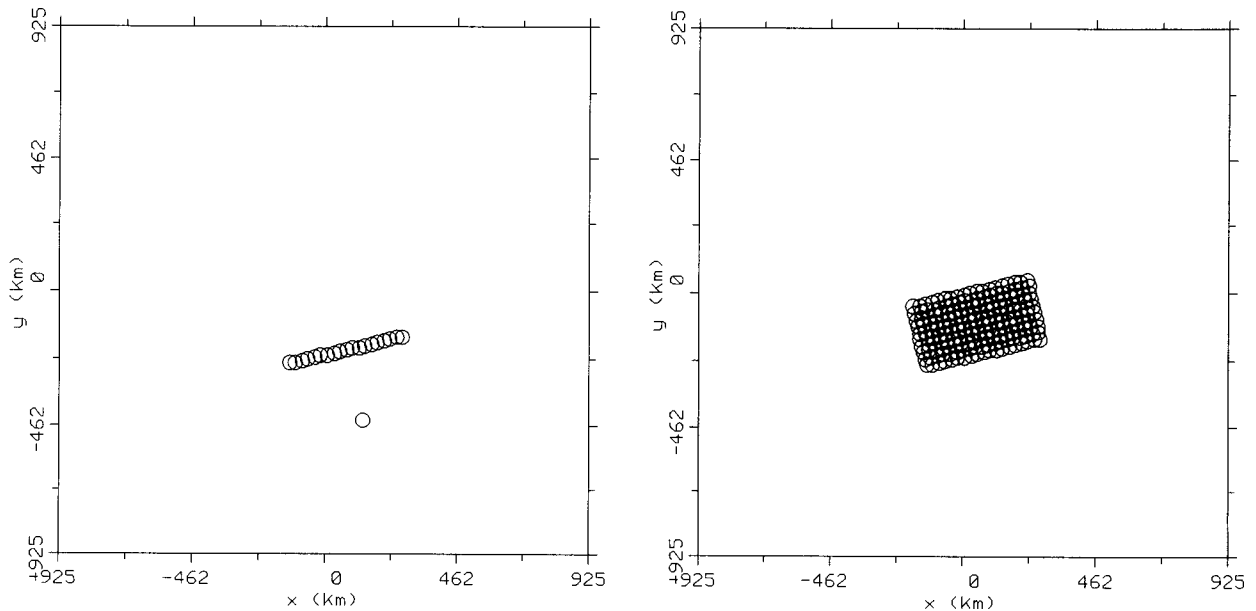


Figure 5.21: Typical cell layout (3 dB contour) for ERS-1 measurements for a single cell and the cells from a single measurement cycle (left) and for several measurement cycles (right).

The simulated A image and SIRF estimate are shown in Fig. 5.22. Since the measurement cells used for this simulation are circular, the resolution of the

SIRF image is circularly symmetric like the SMMR images. From the cross section and estimated error of Fig 5.23, the resolution of the SIRF image is about $\Omega = 0.52$ for $E = 0.6$, which corresponds to a spatial resolution of 12.08 pixels, or 75.5 km. This is about 51 percent larger than the 50-km 3-dB diameter of the measurement cell.

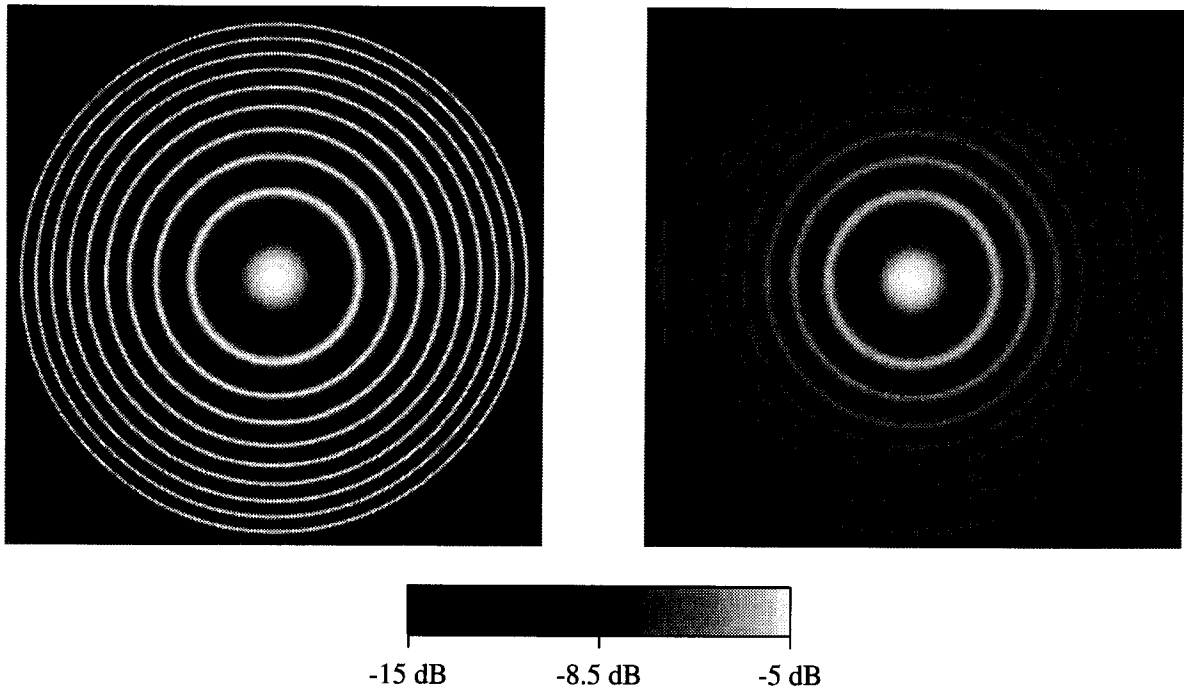


Figure 5.22: Test image (l) and SIRF image (r) for ERS-1 data

The compensating filter was found using the same procedure as for the SMMR images. Again, two different compensating filters were used. Filter 1 incorporated a low pass Chebyshev filter with cutoff at $k = 0.57$ and Filter 2 used a low pass Butterworth filter with cutoff at $k = 0.5$. The results were similar to the SMMR simulation in that Filter 1 enhanced the resolution more than Filter 2, but also introduced more artifacts. The filtered images are shown in Fig. 5.24 with the image from Filter 1 on the left and the image from Filter 2 on the right. The cross sections and estimated errors of Fig. 5.25 show the amount of resolution enhancement achieved. The resolution of the Filter 1 image is $\Omega = 0.58$ and the resolution of the Filter 2 image is $\Omega = 0.56$, which correspond to spatial resolutions of 67.7 km and 70.1 km, respectively.

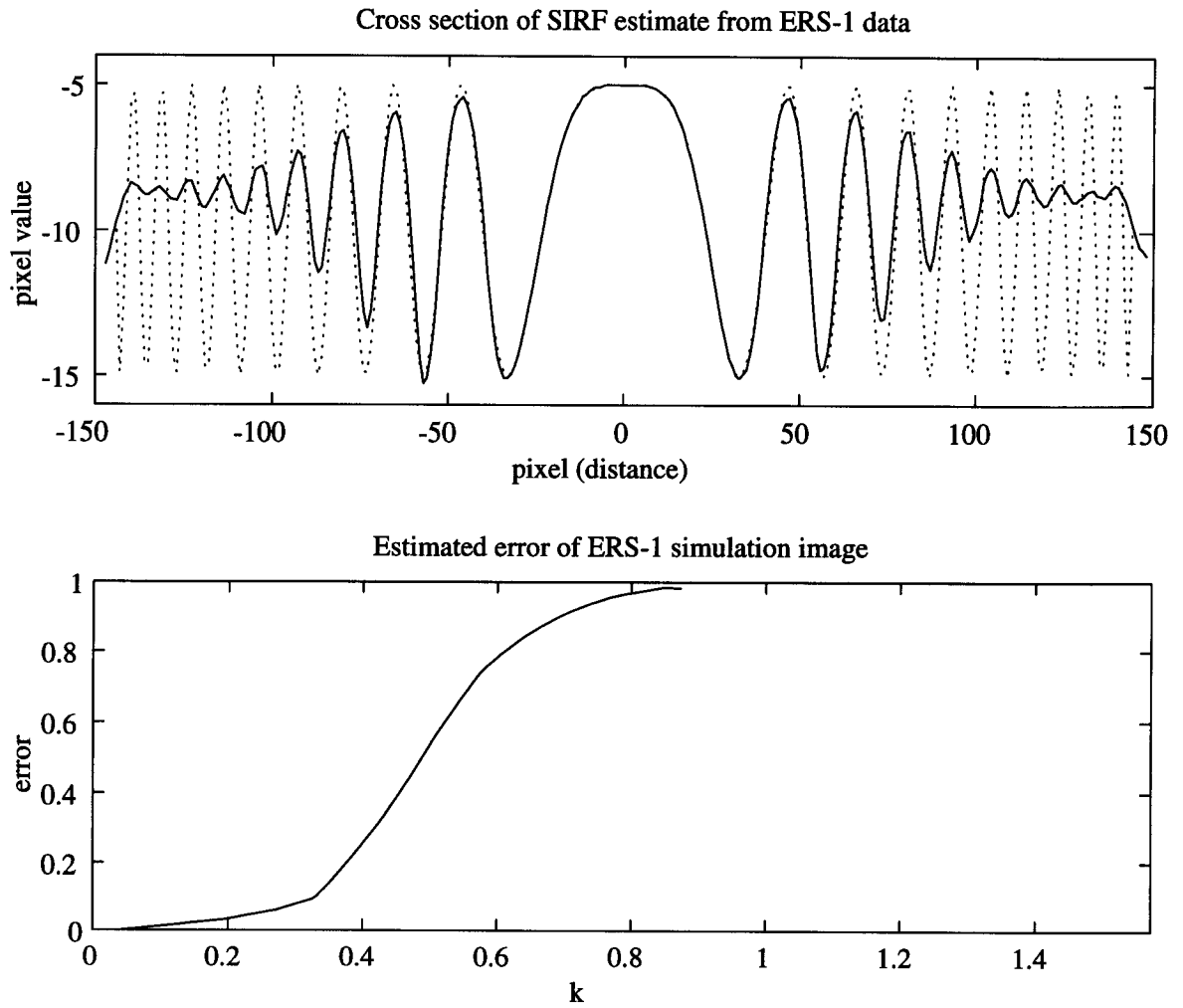


Figure 5.23: Cross section and estimated error of SIRF image from ERS-1 data

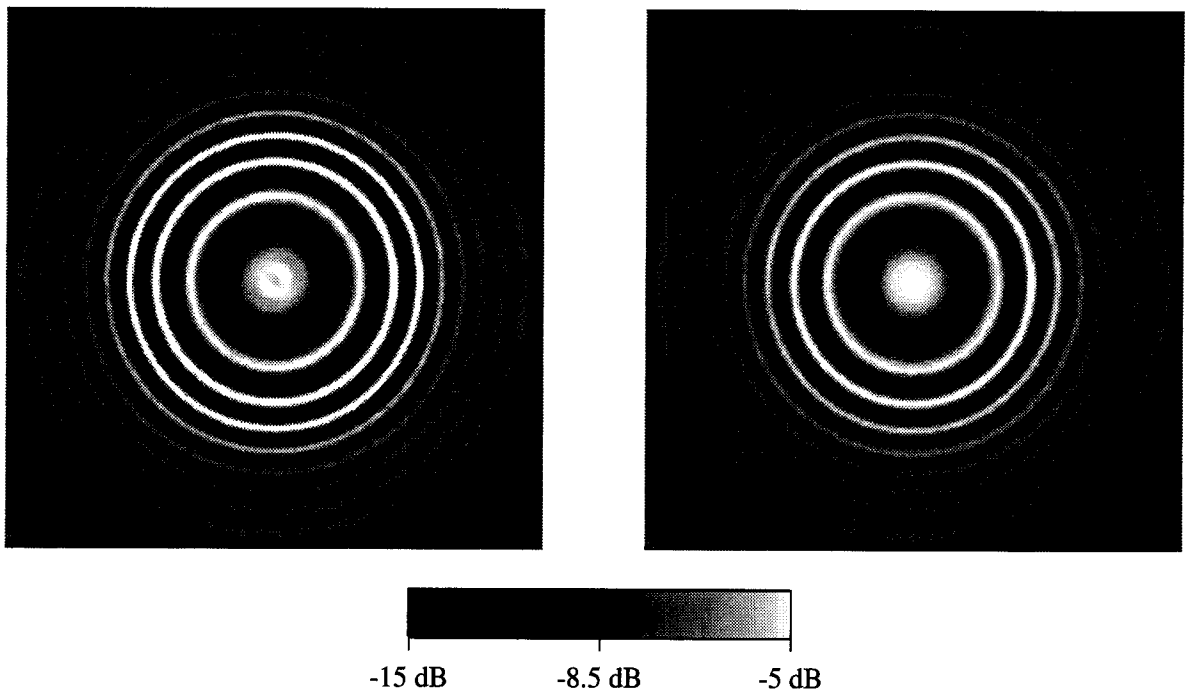


Figure 5.24: ERS-1 SIRF image after compensation filtering from Filter 1 (left) and Filter 2 (right).

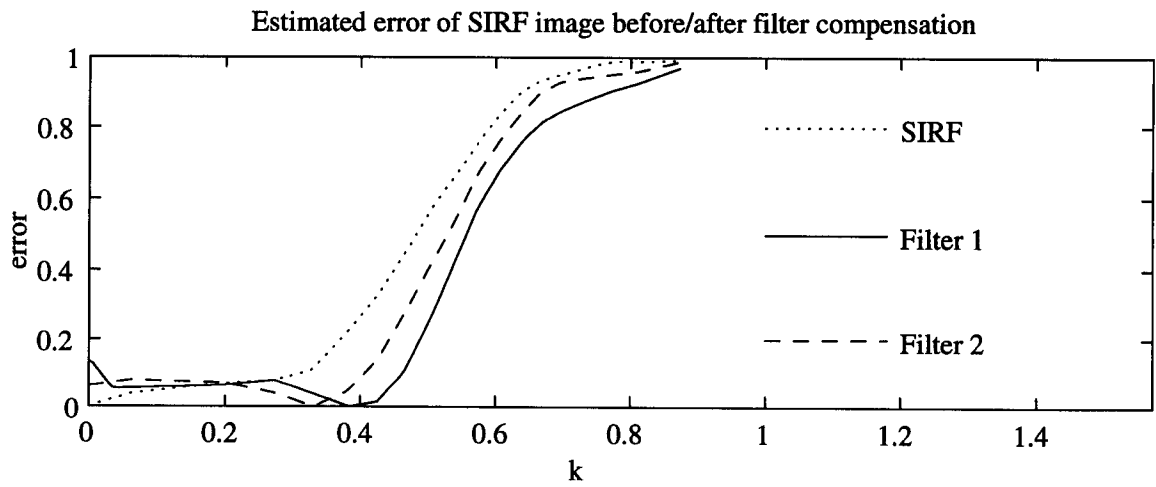
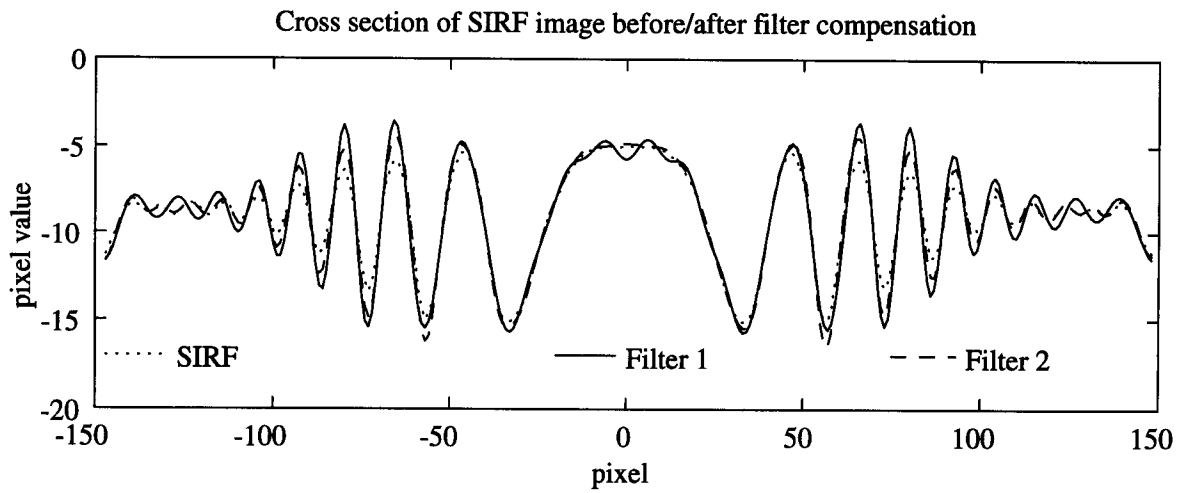


Figure 5.25: Cross section and estimated error of SIRF image after compensation filtering.

To test the effects of noise in the measurements, an image was created from a set of noisy measurements generated from Eq. 5.3. The SIRF image is shown in Fig. 5.26 and the cross section and estimated error are shown in Fig. 5.27. We see from the image and the cross section that the outer rings in the image are lost in the noise level. The estimated error shows that the resolution of the image is about $\Omega = 0.5$, which corresponds to a spatial resolution of 78.5 km.

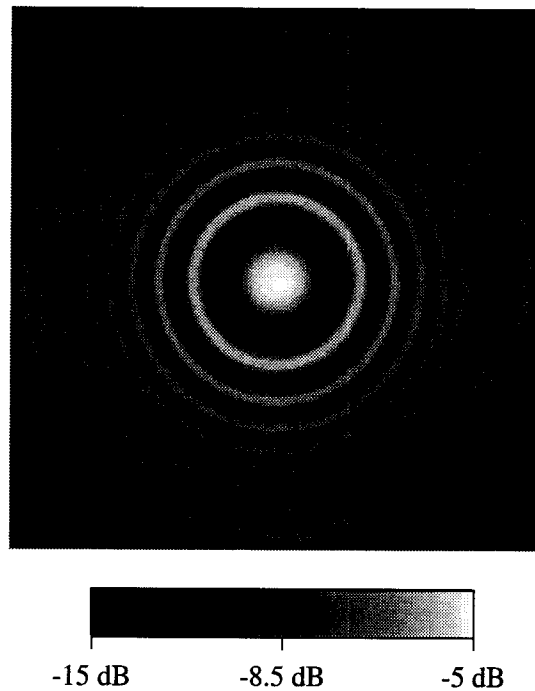


Figure 5.26: SIRF image from simulated noisy ERS-1 measurements.

Finally, we look at the effect of applying a compensating filter to the SIRF image from noisy measurements. Only Filter 2 was used. The filtered image is shown in Fig. 5.28. The cross section and estimated error of the filtered image are shown in Fig. 5.29. From the estimated error, the resolution of the compensation filtered image is $\Omega = 0.55$, which is a spatial resolution of 71.4 km.

5.1.4 Simulation Summary

From the simulation results, the performance of the SIRF imaging technique depends on the shape and orientation of the measurement cells and not on the instrument. Even though the SMMR images required the one-dimensional

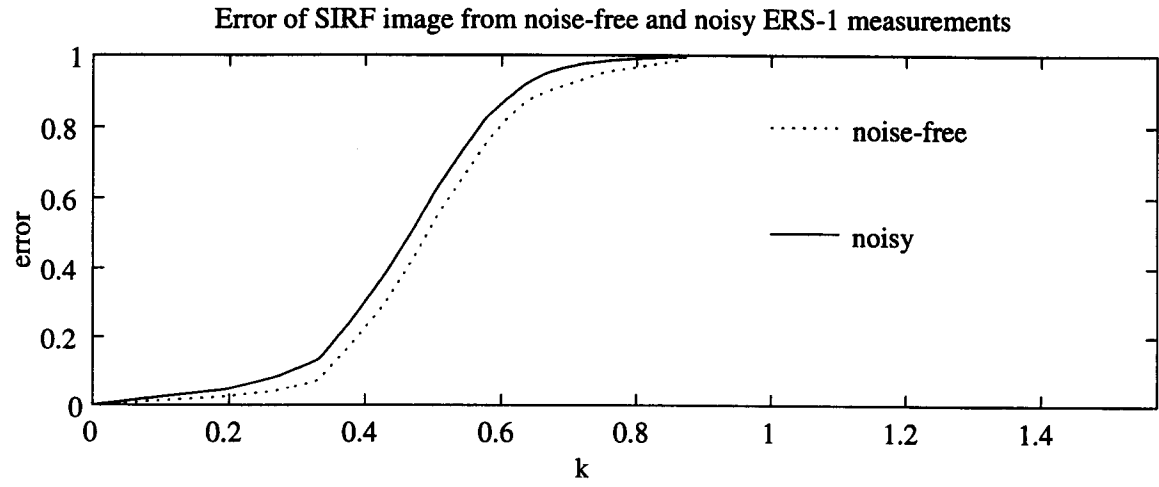
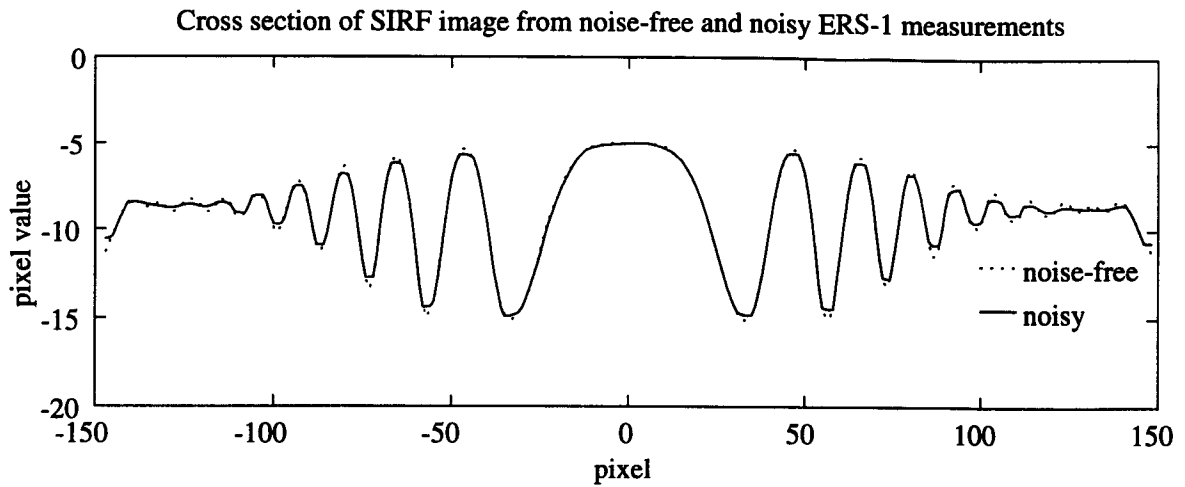


Figure 5.27: Cross section and estimated error of SIRF image from simulated noisy ERS-1 measurements.

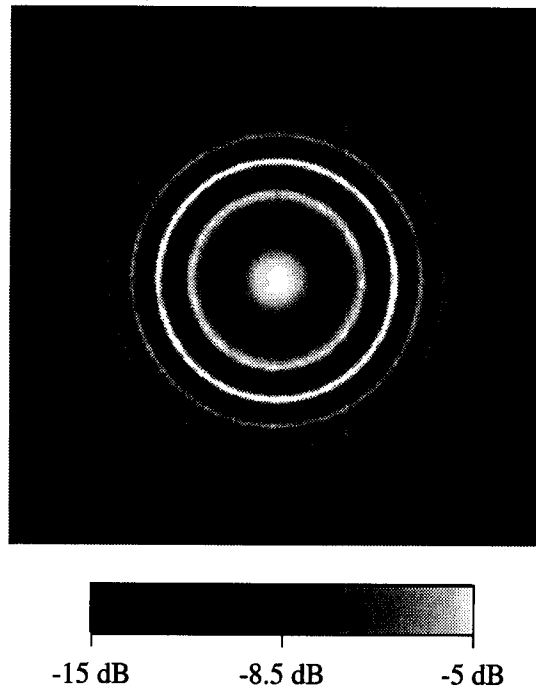


Figure 5.28: SIRF image after compensation filtering from Filter 2.

version of SIRF while the ERS-1 images required the two-dimensional version, the results were similar because both instruments used measurement cells that were essentially circularly symmetric. The reason that SIRF worked so well for the SASS instrument was that the mixing of different sized cells, which were long and narrow and oriented in several different directions, allowed the effective low pass filter inherent in the measurements to be dominated by the short dimension of the measurement cells.

The wavenumber resolutions of the simulation images are given in Table 5.1 and spatial resolutions are given in Table 5.2.

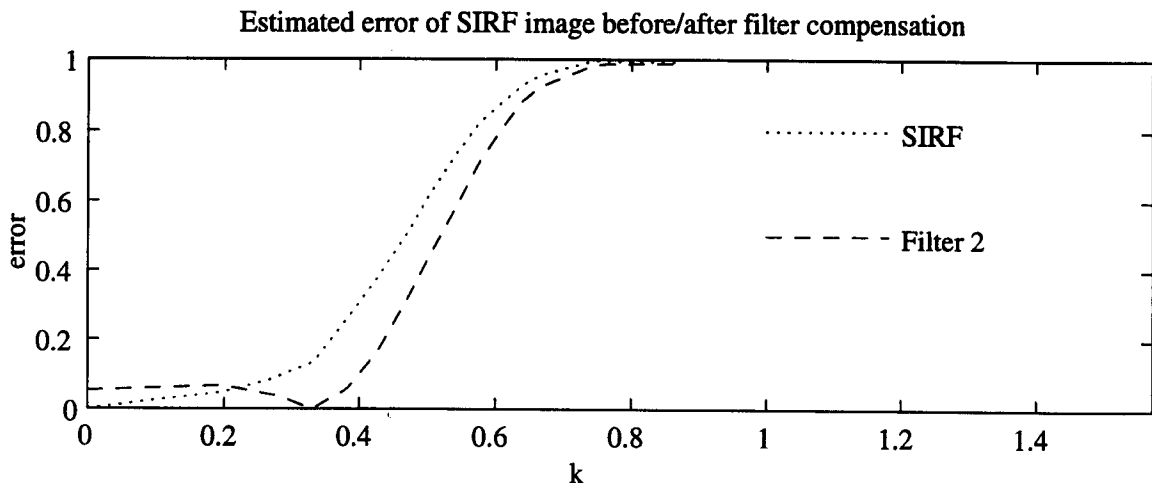
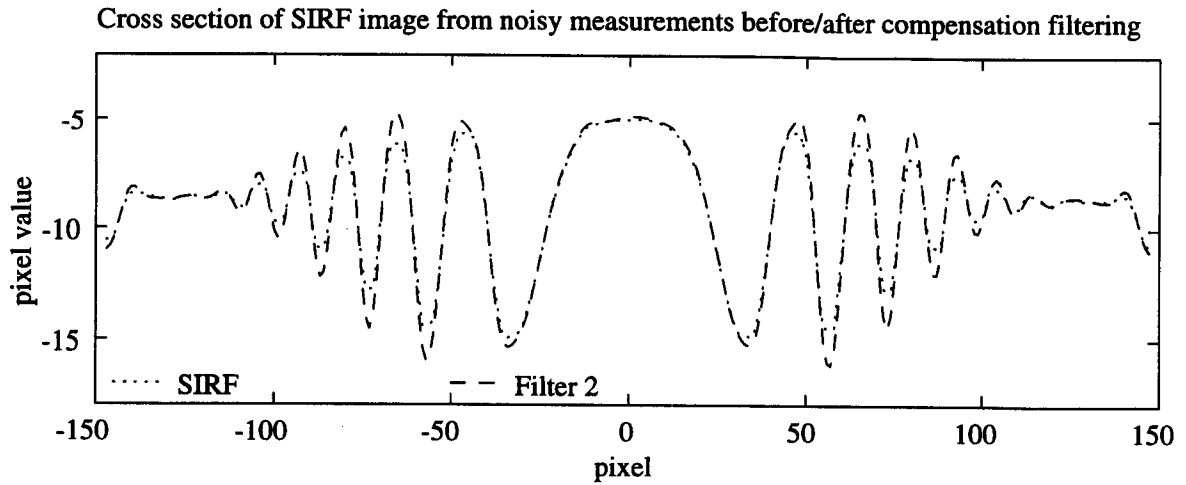


Figure 5.29: Cross section and estimated error of SIRF image from noisy measurements after compensation filtering.

INSTRUMENT	RESOLUTION (WAVENUMBER)			
	NOISE-FREE		NOISY	
	SIRF	COMPENS. FILTERED	SIRF	COMPENS. FILTERED
SMMR 6.6 GHz	0.27	0.30	0.27	0.30
SMMR 10.69 GHz	0.42	0.46	0.42	0.46
SASS	1.0	N/A	1.0	N/A
ERS-1	0.52	0.56	0.50	0.55

Table 5.1: Wavenumber resolution of images from SMMR, SASS, and ERS-1, for $E = 0.6$.

INSTRUMENT	SPATIAL RESOLUTION (KM)			
	NOISE-FREE		NOISY	
	SIRF	COMPENS. FILTERED	SIRF	COMPENS. FILTERED
SMMR 6.6 GHz	145.4	130.9	145.4	130.9
SMMR 10.69 GHz	93.5	85.4	93.5	85.4
SASS	39.3	N/A	39.3	N/A
ERS-1	75.5	70.1	78.5	71.4

Table 5.2: Spatial resolution of images from SMMR, SASS, and ERS-1, for $E = 0.6$.

5.2 Real Data

This section contains images from actual data. The two regions in the images are Greenland for SMMR and SASS, and the Amazon for ERS-1 and SASS. Images of both of these regions had been generated for SASS by other researchers, so it was desired to make images of these regions from the other two instruments to enable a comparison between sensors. Over the Amazon, however, the day to day fluctuations in brightness temperature made that region unsuitable for imaging from SMMR data. Over Greenland, the ERS-1 instrument was inactive, so only data from over the Amazon could be used for that instrument. Thus, two different regions were needed.

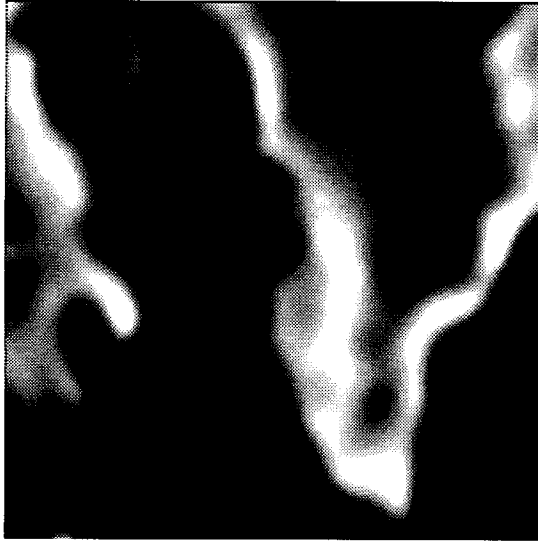
5.2.1 SMMR

Figures 5.30 through 5.33 contain radiometric images of Greenland, Baffin Bay and Baffin Island. Each picture was created from data collected over four consecutive days. The four day time period was chosen because it was the shortest amount of time that gave complete coverage of the entire image region. Using a longer time period did not yield a higher quality image. Each figure shows a four-day period from the middle of four consecutive months. The differences in the images reflect seasonal changes in the structure of the Greenland ice sheet.

Figure 5.34 shows the results of applying the two compensating filters from the SMMR simulations to the 6.6 GHz horizontal polarization image from July 15. Note that the image features, such as the three dark spots in the center of the southern half of Greenland, are enhanced. The introduction of artifacts is also evident, primarily in the central region of the northern half of Greenland. The introduction of artifacts appears to be more pronounced in the image from Filter 1 than in the Filter 2 image. This is consistent with the simulation results since Filter 1 uses a low pass filter with a steeper roll-off than Filter 2.

5.2.2 SASS

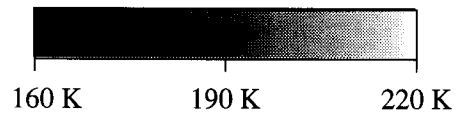
Figure 5.35 shows two SASS *A* images of Greenland from late July and late August. There are gaps in the image because the imaging time is constrained by the rate of change of the ice-sheet structure. The time period for each image



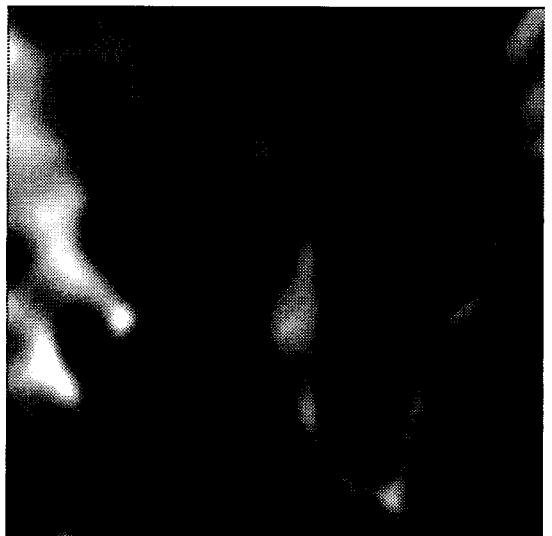
JULY 15 - 18



AUGUST 16 - 19

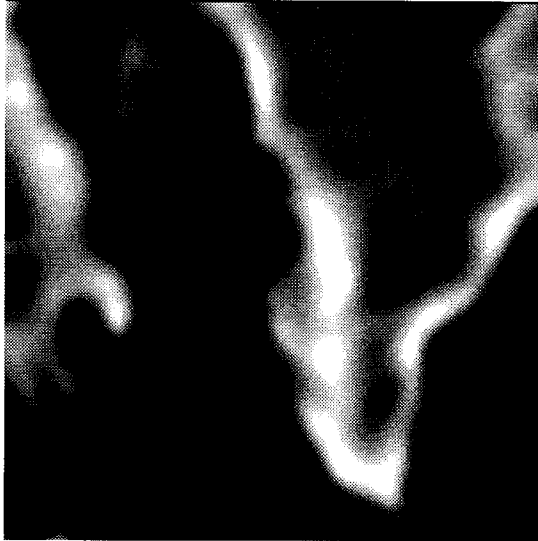


SEPTEMBER 13 - 16

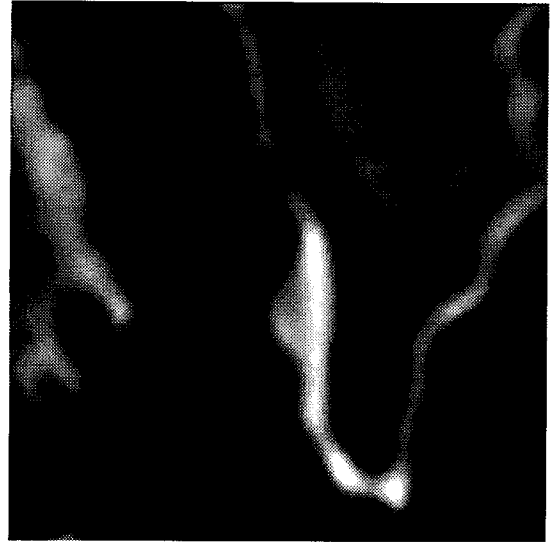


OCTOBER 7 - 10

Figure 5.30: SMMR images from 6.6 GHz vertically polarized measurements.



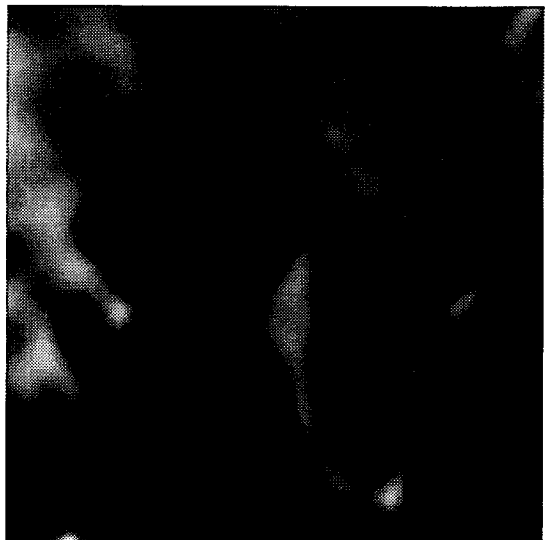
JULY 15 - 18



AUGUST 16 - 19

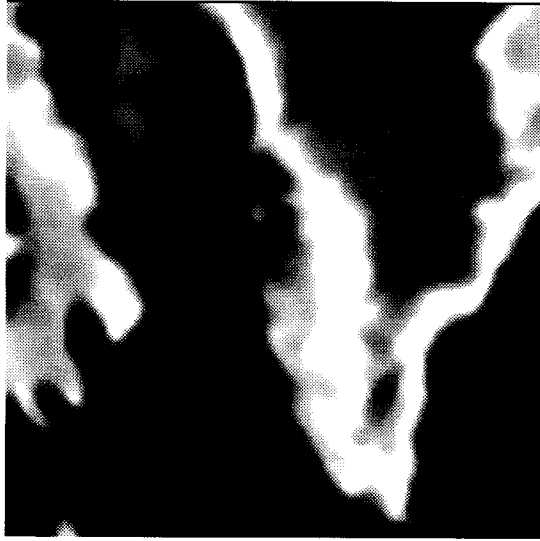


SEPTEMBER 13 - 16



OCTOBER 7 - 10

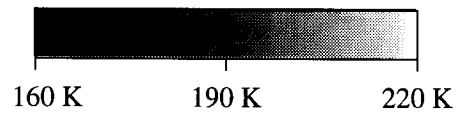
Figure 5.31: SMMR images from 6.6 GHz horizontally polarized measurements.



JULY 15 - 18



AUGUST 16 - 19



SEPTEMBER 13 - 16



OCTOBER 7 - 10

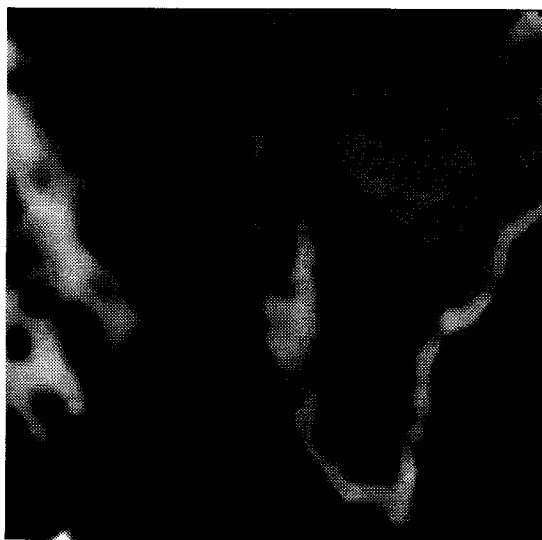
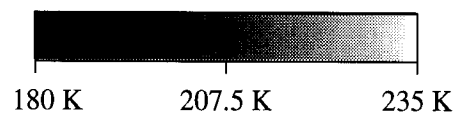
Figure 5.32: SMMR images from 10.69 GHz vertically polarized measurements.



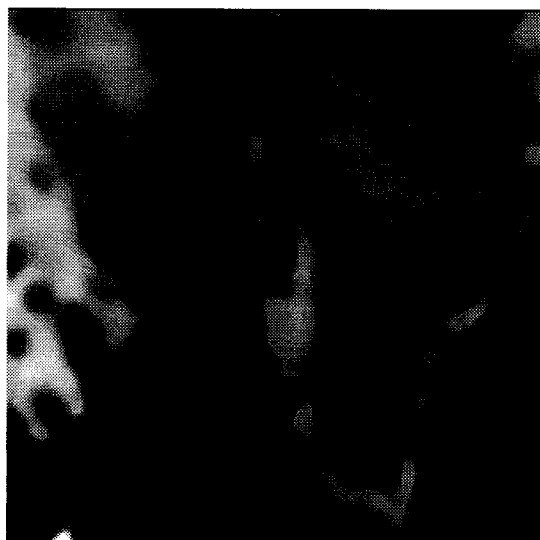
JULY 15 - 18



AUGUST 16 - 19



SEPTEMBER 13 - 16



OCTOBER 7 - 10

Figure 5.33: SMMR images from 10.69 GHz horizontally polarized measurements.

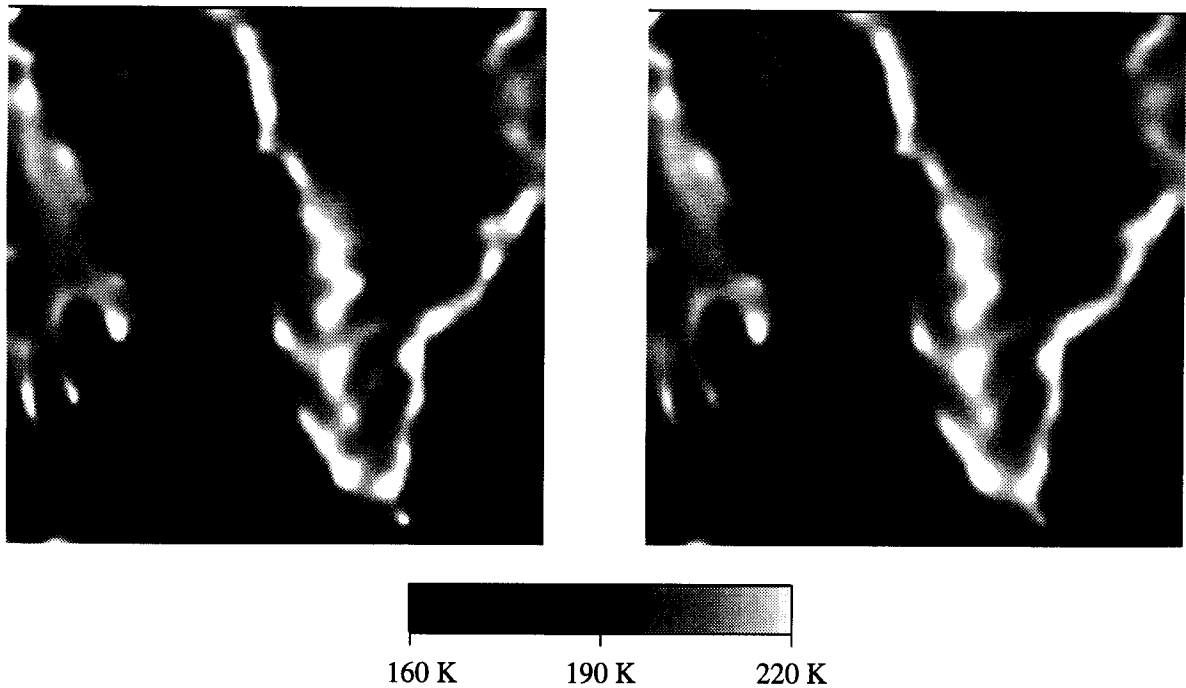


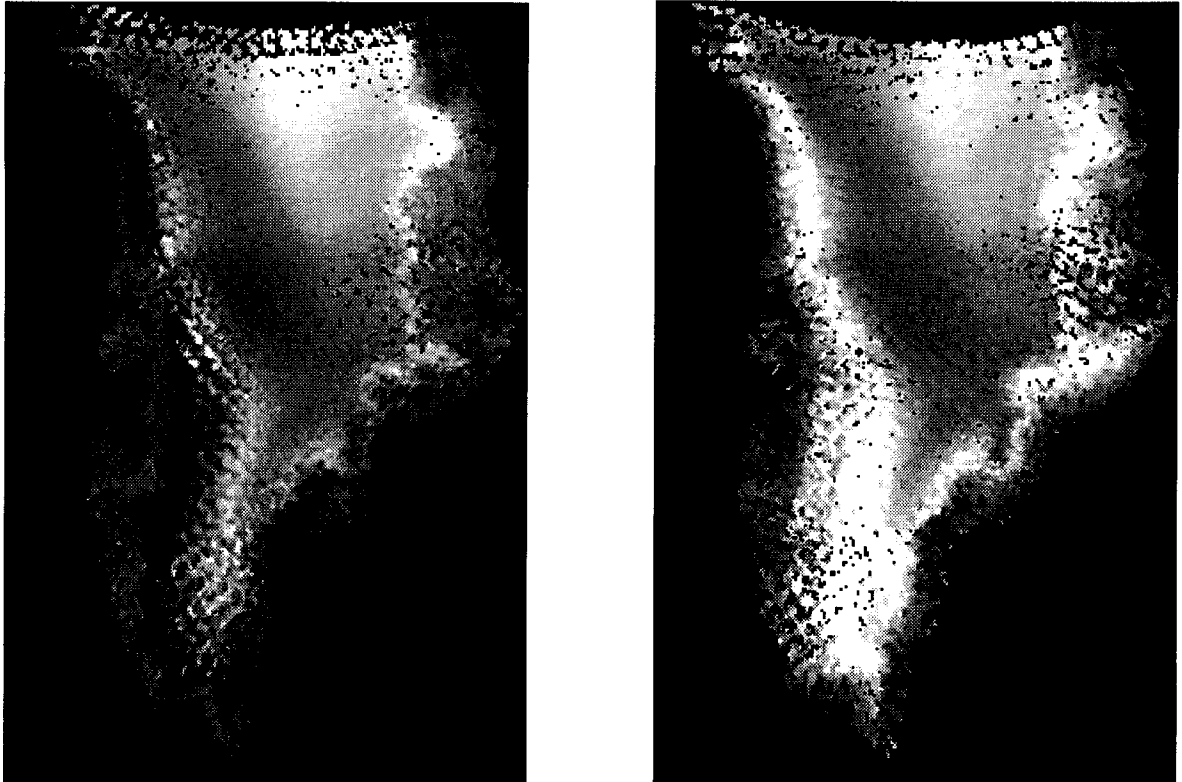
Figure 5.34: Compensation filtered images of 6.6 GHz horizontal polarization data from July 15 - 18, Filter 1 (left) and Filter 2 (right).

was not long enough to get total coverage of the region. Once again, the differences in the images reflect seasonal changes in the Greenland ice sheet. Note the sharper quality of the image than the SMMR images indicating higher resolution.

5.2.3 ERS-1 Scatterometer

Figure 5.36 shows *A* images from ERS-1 and SASS data of a region over the Amazon for a three month period. Many of the same prominent features show up in both images, but the SASS image is much clearer. Even though the SASS measurement cells had one dimension that was longer than the 3-dB diameter of the ERS-1 scatterometer measurement cells, the narrow dimension of the SASS cells allowed for a much higher resolution image. Also, there is some banding in the ERS-1 image due to the inaccuracy of the cell response estimate used.

Figure 5.37 shows the ERS-1 image after applying the compensating filters from the ERS-1 simulation. As was the case in the simulation, Filter 1 produced a sharper image than Filter 2, but also introduced stronger artifacts.



LATE JULY

LATE AUGUST



Figure 5.35: SASS *A* images of Greenland.

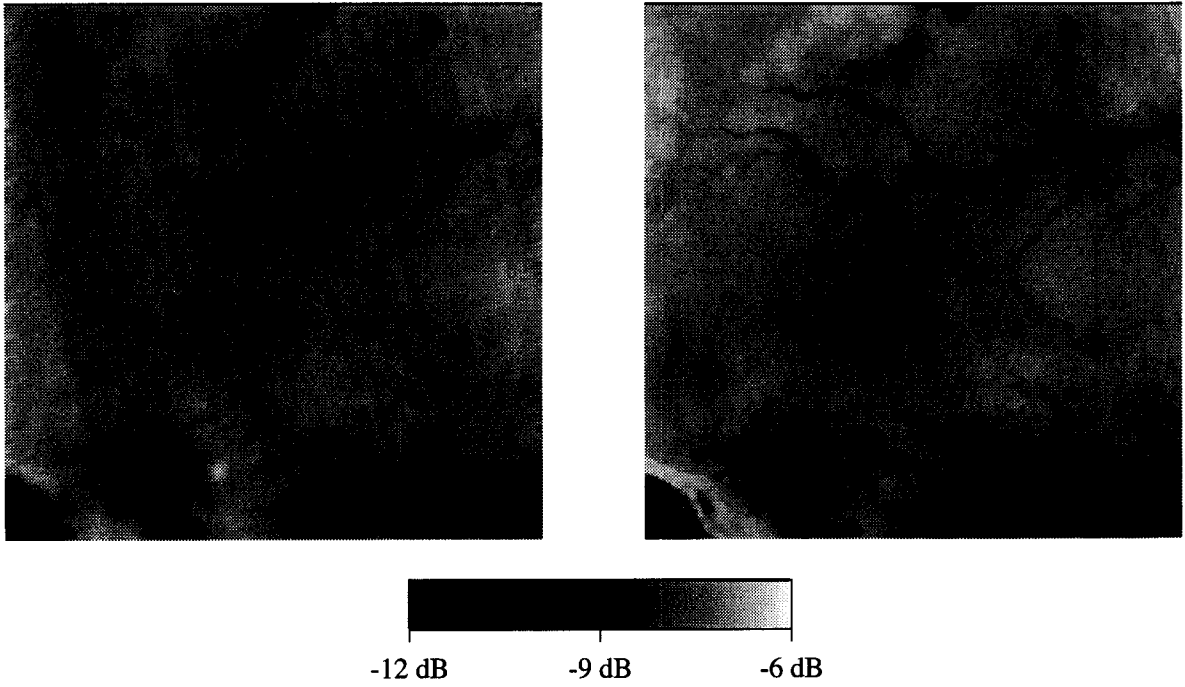


Figure 5.36: ERS-1 (l) and SASS (r) *A* images of the Amazon region.

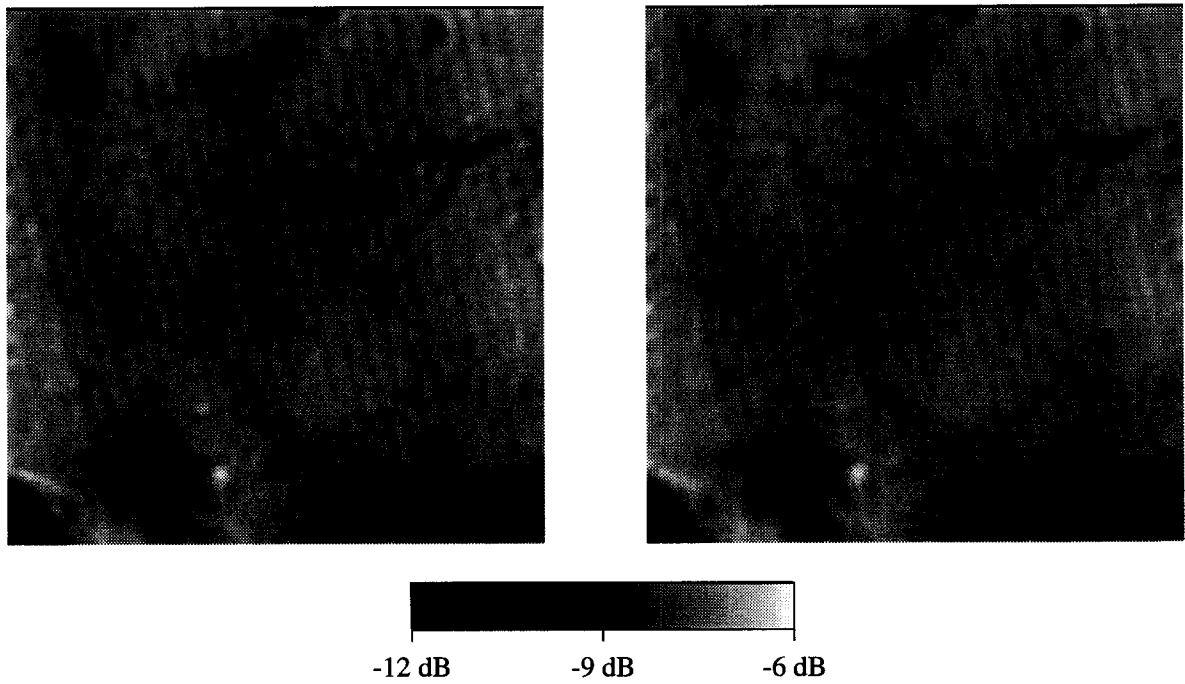


Figure 5.37: ERS-1 *A* image after compensation filtering from Filter 1 (left) and Filter 2 (right).

CHAPTER 6

CONCLUSIONS

6.1 Discussion

In this thesis, the problem of enhancing the resolution of images generated from remotely sensed data was explored. This research was driven by a desire to understand the limitations of a previously published enhanced resolution imaging technique, called SIRF, and to improve the resolution of images generated using this technique. From this research, we draw the following conclusions and results:

1. A spectral-based definition of resolution was developed as an alternative to the traditional definition. The definition for this thesis relates resolution to the bandwidth and the accuracy of the wavenumber spectrum of an image, which implies that in addition to the size of resolvable features in an image, image quality may be used as a measure of resolution.
2. A comparison of the performance of three imaging techniques, referred to as interpolation, AVE, and SIRF, demonstrated that while the SIRF technique exhibited better resolution performance than the other two methods, the image resolution of each method was limited by an effective measurement response. The significance of this rather obvious result is that the SIRF technique improves resolution by reducing the error of the image spectrum rather than by extending its width.
3. From the above result, we conclude that enhancement of resolution implies a correction for the measurement response in the image spectrum. A drawback of resolution enhancement is that a correction of the measurement response over a finite bandwidth introduces artifacts into the image.
4. Further resolution enhancement of SIRF images is possible by determining the effective measurement response of the underlying data and imaging technique and applying a filter with the inverse response to the image. This

method is referred to as compensation filtering. In order to avoid excessive amplification of noise by the inverse filter, a low pass filter should also be used. This method for resolution enhancement should be used with caution because of the introduction of image artifacts.

5. Since the SIRF technique was shown to be limited in resolution by the measurement response (Chapter 3) and because the SASS data combined long and narrow measurement cells whose Fourier transforms cover different regions of the wavenumber plane (Chapter 5), we conclude that the high resolution of the SASS images is due not only to the size, but also to the shape and orientation of the measurement cells. The resolution was dominated by the short dimension of the measurement cells. Since the other instruments used measurement cells that are essentially circular, the resulting images had a more limited increase in resolution.

We saw that the SIRF technique created higher quality images than the other traditional imaging methods, but in order to achieve a dramatic increase in resolution, the underlying data set should have a mixing of measurement cells whose Fourier transforms cover different regions of the wavenumber plane. In this way, the effective measurement response will have a greater extent in the wavenumber domain than the individual measurement cells. The implication for future instruments is that the size of the antenna footprint may actually be larger than the desired resolution in one direction. This could have some mechanical advantages in the design of spaceborne instruments.

6.2 Contributions

The contributions of this research are: (1) an alternative spectral-based definition of resolution for remote sensing applications, (2) a wavenumber analysis technique for comparing the effective resolution of different imaging methods and instruments, (3) a method for further resolution enhancement of images using a compensating filter, (4) an understanding of the impact of measurement cell shape and orientation on resolution, (5) an understanding of the limitations on resolution enhancement imposed by the measurement process, (6) a modified version of SIRF that is applicable to radiometer data, and (7) a set of SMMR images of Greenland

that can be used in conjunction with the SASS images for geophysical studies of that region.

6.3 Future Research

The radiometric images generated from SMMR are made from measurements which are known to contain a mixing of polarized energy due to cross-polarization coupling. In order to obtain more accurate images, a method for determining a “pure” polarization measurement is required. The measurement cell geometry and cell response information should not be degraded by the method, because this information is required by the imaging technique.

While the SIRF method is the only published method for imaging from scatterometer data, a different method for resolution enhanced imaging from radiometric data has been presented [17]. This method, known as the Backus-Gilbert approach, has been successfully applied to a high frequency radiometer, the Special Sensor Microwave/Imager (SSM/I). A comparison of that method with the methods described in this thesis should be performed. This comparison would require that SIRF and the compensation filter be applied to the SSM/I data and that the Backus-Gilbert approach be applied to the SMMR data. Simulations similar to those presented in this thesis would enable a comparison of the two techniques.

Finally, suppose a set of measurements is made from cell responses that have strong sidelobes in the wavenumber domain. It is conceivable that the information in the sidelobes could be extracted to obtain high wavenumber information about the underlying surface. Furthermore, it may be possible to combine measurements made from different sized measurement cells that have strong sidelobes in such a way that the sidelobes and nulls of the different measurement cells cancel each other, resulting in a measurement response that has a very wide spectrum. Such a system could be used to generate images with resolution much higher than the size of the footprints. Towards that end, the ability of the SIRF technique to extract information from the sidelobes should be investigated.

BIBLIOGRAPHY

- [1] R. Massom, *Satellite Remote Sensing of Polar Regions*. Boca Raton, FL: Lewis Publishers, 1991.
- [2] T. J. Jackson and T. J. Schmugge, "Algorithm for the passive microwave remote sensing of soil moisture," in *Microwave Radiometry and Remote Sensing Applications* (P. Pampaloni, ed.), (Zeist), pp. 3–17, VSP, 1989.
- [3] D. G. Long, P. J. Hardin, and P. T. Whiting, "Resolution enhancement of spaceborne scatterometer data," *IEEE Transactions on Geoscience and Remote Sensing*, vol. 31, pp. 700–715, May 1993.
- [4] M. J. McFarland, R. L. Miller, and C. M. U. Neale, "Land surface temperature derived from the SSM/I passive microwave brightness temperatures," *IEEE Transactions on Geoscience and Remote Sensing*, vol. 28, pp. 839–845, September 1990.
- [5] A. V. Oppenheim and A. S. Willsky, *Signals and Systems*. Englewood Cliffs, NJ: Prentice-Hall, 1983.
- [6] P. T. Whiting, "Resolution enhancement of seasat scatterometer data," master's thesis, Brigham Young University, Provo, UT, 1992.
- [7] F. T. Ulaby, R. K. Moore, and A. K. Fung, *Microwave Remote Sensing, Active and Passive*, vol. 1. Norwood, MA: Artech House Inc., 1981.
- [8] N. Levanon, *Radar Principles*. New York, NY: Wiley-Interscience, 1988.
- [9] R. G. Kennett and F. K. Li, "Seasat over-land scatterometer data, part I: Global overview of ku-band backscatter coefficients," *IEEE Transactions on Geoscience and Remote Sensing*, vol. 27, pp. 592–605, September 1989.
- [10] E. G. Njoku, J. M. Stacey, and F. T. Barath, "The seasat scanning multi-channel microwave radiometer (SMMR): Instrument description and performance," *IEEE Journal of Oceanic Engineering*, vol. OE-5, pp. 100–115, April 1980.

- [11] D. H. Boggs, *Algorithm Development Facility Scatterometer Sensor Algorithm Specifications*. California: Jet Propulsion Laboratory, 1981.
- [12] Personal communication between David Long and Evert Attema.
- [13] P. N. Swanson and A. L. Riley, "The seasat scanning multichannel microwave radiometer (SMMR): Radiometric calibration algorithm development and performance," *IEEE Journal of Oceanic Engineering*, vol. OE-5, pp. 116–124, April 1980.
- [14] E. G. Njoku, E. J. Christensen, and R. E. Cofield, "The seasat scanning multichannel microwave radiometer (SMMR): Antenna pattern corrections - development and implementation," *IEEE Journal of Oceanic Engineering*, vol. OE-5, pp. 125–137, April 1980.
- [15] A. K. Jain, *Fundamentals of Digital Image Processing*. Englewood Cliffs, NJ: Prentice-Hall, 1989.
- [16] *Geophysical Data Record (GDR) Users Handbook - Scanning Multichannel Microwave Radiometer (SMMR)*. Pasadena, CA: Jet Propulsion Laboratory, 1982.
- [17] G. A. Poe, "Optimum interpolation of imaging microwave radiometer data," *IEEE Transactions on Geoscience and Remote Sensing*, vol. 28, pp. 800–810, April 1990.